

# **Nonlinear finite element analysis of quasi-brittle materials**



A thesis submitted to the University of Cardiff for the  
degree of Doctor of Philosophy

By

Waled Farj Alnaas

April-2016

To my beloved father and grandfather

## **Declaration**

This work has not previously been accepted in substance for any degree and is not concurrently submitted in candidature for any other higher degree.

Signed:.....(Candidate)      Date:.....

## **Statement 1**

This thesis is being submitted in partial fulfilment of the requirements for the degree of Doctor of Philosophy (PhD).

Signed:.....(Candidate)      Date:.....

## **Statement 2**

This thesis is the result of my own independent work/investigation, except where otherwise stated. Other sources are acknowledged by explicit references.

Signed:.....(Candidate)      Date:.....

## **Statement 3**

I hereby give consent for my thesis, if accepted, to be available for photocopying, inter-library loan and for the title and summary to be made available to outside organisations.

Signed:.....(Candidate)      Date:.....

## Summary

The development of robust solution schemes for the nonlinear finite element analysis of quasi-brittle materials has been a challenging undertaking, due mainly to the stability and convergence difficulties associated with strain-softening materials. The work described in this thesis addresses this issue by proposing a new method for improving the robustness and convergence characteristics of a finite element damage model. In this method, a smooth unloading-reloading function is employed to compute an approximate tangent matrix in an incremental iterative Newton type solution procedure. The new method is named ‘the smooth unloading-reloading’ (SUR) method. A range of examples, based on a set of idealised quasi-brittle specimens, are used to assess the performance of the SUR method. The results from these example analyses show that the proposed approach is numerically robust, effective and results in considerable savings relative to solutions obtained with a reference secant model.

Three acceleration approaches are also proposed in this thesis to further improve the convergence properties of the new SUR method. The first acceleration approach, named ‘the predictive-SUR method’, predicts a converged value of a damage evolution variable using an extrapolation in semi-log space. The second proposed method is designated ‘the fixing approach’, in which a damage evolution parameter is updated from the last converged step in Stage-1 iterations and then fixed in Stage-2 iterations. The third acceleration technique employs ‘a slack tolerance’ at key stages in a computation. The improvement of the convergence properties of the SUR method, when the proposed acceleration approaches are introduced, is illustrated using a series of example computations based on the analysis of a range of plain and reinforced concrete structural elements.

In addition, a new element with an embedded strong discontinuity is proposed for simulating cracks in quasi-brittle structures. The new formulation is applied to quadrilateral elements and exploited to simulate mode-I, mode-II and mixed mode fracture. The interface element approach and the smeared crack approach are used as reference methods. The results from a series of examples show that the new proposed embedded strong discontinuity approach is both effective and accurate.

## **Acknowledgment**

I would like to express my heartfelt gratitude to my supervisor Prof Tony Jefferson. Tony, your endless support, encouragement, enthusiastic guidance, patience and immense knowledge motivated me to keep going when I was down. I consider myself fortunate to work with a kind, easy-going, helpful, disciplined, modest, wise and knowledgeable person like you.

I am also deeply indebted to Dr Iulia Mihai for her help and useful discussions, especially in the first year of my PhD.

My sincere thanks go to my colleagues in offices W1.31 and W1.32: Robert Davies, Martins Pilegis, Chuansan Ma, Oliver Teall, Adrianna Chitez, Tobias Hazelwood, Shukri, Brubeck, Thomas, Stefani and Monica. Being with you makes the study place a cheerful environment and the research an enjoyable experience.

I would like to thank my friends for their support in all time during my PhD journey. There are too many to mention here, but you know who you are.

My especial thanks go to my family. Father and Grandfather, I will do my best in this life to make you proud of me until we meet again in paradise in the hereafter. Mother, thank you so much for everything you have done for me, there are so many to account, so whatever I write or do for you, I would not give you what you deserve, I love you so much. My wonderful brothers and sisters, thank you for your love, support and having faith in me.

Last but not least, I would like to thank God for his blessing, mercy and being with all aforementioned.

# Contents

Summary .....	iii
Acknowledgment.....	iv
Table of Figures.....	vii
List of Tables.....	xii
Notations .....	xiii
<b>Chapter 1: Introduction</b>	
1.1 Introduction .....	1
1.2 Aims and objectives .....	4
1.3 Outline of the thesis.....	5
1.4 List of publications .....	7
<b>Chapter 2: Literature review</b>	
2.1 Finite element method for modelling cracks .....	9
2.1.1 Discrete crack approach .....	9
2.1.2 Smearred crack approach .....	11
2.2 Concrete modelling .....	12
2.2.1 Mechanical behaviour of Concrete .....	12
2.2.2 Constitutive models for concrete .....	13
2.2.3 Continuum damage mechanics .....	16
2.3 Localization of strain.....	19
2.4 Solution techniques for nonlinear finite element analysis.....	21
2.5 Elements with embedded SD approach.....	27
2.5.1 Work of the Delft research group.....	27
2.5.2 Work of the research group at UPC .....	29
2.5.2 Work of other research groups.....	30
<b>Chapter 3: An incremental iterative method for numerical simulation of quasi-brittle materials.</b>	
3.1 Introduction .....	32
3.2 Constitutive model .....	33
3.2 Smooth unloading-reloading and target damage functions.....	37
3.3 Fracture energy for simplified softening curve .....	41

3.4	Element characteristic length calculation .....	44
3.5	Convergence criteria.....	46
3.6	Numerical examples .....	48
3.7	General discussion and conclusions .....	73
<b>Chapter 4: Acceleration techniques for the smooth unloading-reloading method</b>		
4.1	Introduction .....	75
4.2	Acceleration techniques.....	75
4.2.1	Predictive-SUR approach.....	75
4.2.2	Fixing algorithm.....	80
4.2.3	Slack tolerance technique.....	80
4.3	Numerical implementation .....	81
4.4	Discussion and conclusions .....	103
<b>Chapter 5: A new formulation for elements with embedded strong discontinuity</b>		
5.1	Introduction .....	106
5.2	Kinematic of strong discontinuity .....	108
5.3	A new formulation for an element with an embedded SD .....	109
5.4	Interface element formulation .....	115
5.5	Damage function .....	119
5.6	Numerical examples .....	120
5.7	Discussion and conclusions .....	130
<b>Chapter 6: Conclusions and future work</b>		
6.1	Conclusions .....	132
6.2	Recommendations for future work .....	135
	Appendices .....	136
	References .....	138

## Table of Figures

Figure 2.1: Stress-strain curve in damage, plastic and coupled damage-plastic models (Nguyen, 2005). .....	15
Figure 3.1: Unloading-reloading and target damage evolution function. ....	38
Figure 3.2: Stress-strain curve of quasi-brittle materials. ....	42
Figure 3.3: Quadrilateral and triangular elements.....	45
Figure 3.4: 1D bar subjected to 0.2 mm prescribed displacement. ....	50
Figure 3.5: Displacement-stress relationship for the 1D bar with 40 and 100 increments (convergence tolerance =0.1%). ....	50
Figure 3.6: Displacement-stress relationship for the 1D bar using SUR approach with $10^{-3}$ and $10^{-6}$ convergence tolerances. ....	51
Figure 3.7: Number of iterations to achieve convergence for the most difficult increments of the 1D bar with 40 increments (convergence tolerance = $10^{-6}$ ). ....	52
Figure 3.8: Number of iterations to achieve convergence for the most difficult increments of the 1D bar with 40 increments (convergence tolerance= $10^{-3}$ ). ....	52
Figure 3.9: Number of iterations to achieve convergence for the most difficult increments of the 1D bar with 100 increments (convergence tolerance= $10^{-6}$ ). ....	53
Figure 3.10: Number of iterations to achieve convergence for the most difficult increments of the 1D bar with 100 increments (convergence tolerance= $10^{-3}$ ). ....	53
Figure 3.11: Dimension of the 2D notched plane stress example.....	54
Figure 3.12: Finite element mesh.....	55
Figure 3.13: Exaggerated deformed mesh plots at final increment for Mesh1 and Mesh2.....	55
Figure 3.14: Damage contour plots for different displacement increment (2D plane stress example).....	56
Figure 3.15: Displacement-Stress relationship for 2D plane stress example with 50 steps.....	56
Figure 3.16: Displacement-Stress relationship for 2D plane stress example with 100 steps.....	57
Figure 3.17: Displacement-Stress relationship for Mesh1 using SUR approach with convergence tolerances $10^{-3}$ and $10^{-6}$ .....	57

Figure 3.18: Number of iterations to achieve convergence for the most difficult increments of Mesh1 with 50 increments (convergence tolerance= $10^{-3}$ ). .....	58
Figure 3.19: Number of iterations to achieve convergence for the most difficult increments of Mesh1 with 50 increments (convergence tolerance= $10^{-6}$ ). .....	58
Figure 3.20: Number of iterations to achieve convergence for the most difficult increments of Mesh2 with 50 increments (convergence tolerance= $10^{-3}$ ). .....	59
Figure 3.21: Number of iterations to achieve convergence for the most difficult increments of Mesh2 with 50 increments (convergence tolerance= $10^{-6}$ ). .....	59
Figure 3.22: Number of iterations to achieve convergence for the most difficult increments of Mesh1 with 100 increments (convergence tolerance= $10^{-3}$ ). .....	60
Figure 3.23: Number of iterations to achieve convergence for the most difficult increments of Mesh1 with 100 increments (convergence tolerance= $10^{-6}$ ). .....	60
Figure 3.24: Number of iterations to achieve convergence for the most difficult increments of Mesh2 with 100 increments (convergence tolerance= $10^{-3}$ ). .....	61
Figure 3.25: Number of iterations to achieve convergence for the most difficult increments of Mesh2 with 100 increments (convergence tolerance= $10^{-6}$ ). .....	61
Figure 3.26: Dimension details of the RC prism. ....	62
Figure 3.27: Finite element mesh of RC prism. ....	62
Figure 3.28: Exaggerated deformed mesh plot at final increment. ....	63
Figure 3.29: Damage value contour plot at final displacement increment. ....	63
Figure 3.30: Load-displacement responses of reinforced bar. ....	64
Figure 3.31: Number of iterations to achieve convergence for the most difficult increments of the RC prism with 50 increments. ....	64
Figure 3.32: Number of iterations to achieve convergence for the most difficult increments of the RC prism with 100 increments. ....	65
Figure 3.33: dimensional details of the double notched specimen. ....	66
Figure 3.34: Exaggerated deformed mesh plot. ....	66
Figure 3.35: Damage indicator contour plots at different displacement increments. ....	68
Figure 3.36: Numerical displacement and vertical stress responses with 40 and 100 prescribed displacement increments. ....	69
Figure 3.37: (a) Minimum principal stress contour plot, (b) Maximum principal stress contour plot, both at final displacement increment. ....	69
Figure 3.38: Number of iterations to achieve convergence for the most difficult increments with 40 increments. ....	70

Figure 3.39: Number of iterations to achieve convergence for the most difficult increments with 100 increments.....	70
Figure 3.40: Dimensional details for 2D specimen.....	71
Figure 3.41: Displacement-Stress relationship for varying the two main parameters of SUR function. ....	72
Figure 3.42: Number of iterations to achieve convergence for the most difficult increments of the SUR solution with Cases 1 and 2. ....	72
Figure 4.1: 1D bar subjected to 0.2 mm prescribed displacement. ....	76
Figure 4.2: Number of iterations to achieve convergence for the most difficult increments of the 1D bar. ....	76
Figure 4.3: Relationship between number of iterations at the most difficult step (step No. 3) and the differences between damage evolution parameters for the 1D bar. ...	77
Figure 4.4: Relation between number of iterations and differences between damage evolution parameters within a time step.....	78
Figure 4.5: Numerical displacement-stress responses for 1D example with $10^{-3}$ convergence tolerance. ....	83
Figure 4.6: Numerical displacement-stress responses for 1D example with $10^{-6}$ convergence tolerance. ....	83
Figure 4.7: Number of iterations to achieve convergence for the most difficult increments for the analysis with 40 steps (convergence tolerance = $10^{-3}$ ).....	84
Figure 4.8: Number of iterations to achieve convergence for the most difficult increments for the analysis with 40 steps (convergence tolerance = $10^{-6}$ ).....	85
Figure 4.9: Number of iterations to achieve convergence for the most difficult increments for the analysis with 100 steps (convergence tolerance = $10^{-3}$ ).....	85
Figure 4.10: Number of iterations to achieve convergence for the most difficult increments for the analysis with 100 steps (convergence tolerance= $10^{-6}$ ).....	86
Figure 4.11: Total number of iterations that needed for each solution in the 1D example using convergence tolerance $10^{-3}$ . ....	86
Figure 4.12: Total number of iterations that needed for each solution in the 1D example with convergence tolerance of $10^{-6}$ .....	87
Figure 4.13: Out of balance force norm at the end of each increment for the analysis with 40 steps and convergence tolerance = $10^{-3}$ . ....	88
Figure 4.14: Out of balance force norm history for increment number 3 with 40 steps and convergence tolerance = $10^{-3}$ .....	88

Figure 4.15: Out of balance force norm at the end of each increment for the analysis with 100 steps and convergence tolerance = $10^{-6}$ .	89
Figure 4.16: Out of balance force norm history for increment number 9 with 100 steps and convergence tolerance= $10^{-6}$ .	89
Figure 4.17: (a) 2D notched plane stress, (b) finite element Mesh1.	90
Figure 4.18: Displacement-Stress relationship for 2D plane stress specimen (convergence tolerance = $10^{-3}$ ).	91
Figure 4.19: Displacement-Stress relationship for 2D plane stress specimen (convergence tolerance = $10^{-6}$ ).	91
Figure 4.20: Damage contour plot at last displacement increment.	92
Figure 4.21: Number of iterations to achieve convergence for the most difficult increments for the analysis with 50 increments and convergence tolerance= $10^{-3}$ .	93
Figure 4.22: Number of iterations to achieve convergence for the most difficult increments for the analysis with 50 increments and convergence tolerance= $10^{-6}$ .	93
Figure 4.23: Number of iterations to achieve convergence for the most difficult increments for the analysis with 100 increments and convergence tolerance= $10^{-3}$ .	94
Figure 4.24: Number of iterations to achieve convergence for the most difficult increments for the analysis with 100 increments and convergence tolerance= $10^{-6}$ .	94
Figure 4.25: Total number of iterations that needed for each solution using convergence tolerance = $10^{-3}$ .	95
Figure 4.26: Total number of iterations that needed for each solution using convergence tolerance = $10^{-6}$ .	95
Figure 4.27: RC prism dimensions.	96
Figure 4.28: Load-displacement responses of RC prism.	97
Figure 4.29: Number of iterations to achieve convergence for the most difficult increments of RC prism with 50 increments.	98
Figure 4.30: Number of iterations to achieve convergence for the most difficult increments of RC prism with 100 increments.	98
Figure 4.31: Total number of iterations that needed for each solution in the RC prism example.	99
Figure 4.32: Geometry of the 2D double notched specimen.	100
Figure 4.33: Numerical displacement and vertical stress responses 2D double notched specimen.	101
Figure 4.34: Damage indicator contour plot at last displacement increment.	101

Figure 4.35: Number of iterations to achieve convergence for the most difficult increments with 40 increments.....	102
Figure 4.36: Number of iterations to achieve convergence for the most difficult increments with 100 increments.....	102
Figure 4.37: Total number of iterations that needed for each solution in the 2D double notched problem.....	103
Figure 5.1: A Domain crossed by a strong discontinuity surface. ....	108
Figure 5.2: A four node element with an embedded strong discontinuity. ....	110
Figure 5.3: An interface element with $n$ pairs of nodes in local coordinates.....	116
Figure 5.4: Loading conditions and deformed meshes using linear elastic analysis for the proposed IESD approach and IEA. ....	124
Figure 5.5: 2D plane stress specimen dimensions. ....	125
Figure 5.6: Coarse and fine meshes with their deformed shapes (magnified 30 times). ....	126
Figure 5.7: Stress-displacement responses with different methods. ....	126
Figure 5.8: Vertical displacement contour plot for the fine mesh.....	127
Figure 5.9: Double notched plane stress example.....	128
Figure 5.10: Exaggerated deformed mesh: (a) smeared approach and (b) proposed interface embedded strong discontinuity (IESD) approach. ....	129
Figure 5.11: Vertical stress and displacement response.....	129

## List of Tables

Table 3.1: Summary of isotropic damage model algorithm Oliver et al (1990; 2002; 2006a).....	34
Table 3.2: Material properties and convergence tolerances. <b>Error! Bookmark not defined.</b>	
Table 4.1: Predictive function algorithm. ....	79
Table 4.2: Material properties and convergence tolerances. ....	82
Table 5.1: Shape functions for the interface element shown in Figure 5.3.....	117
Table 5.2: Horizontal and vertical displacements at the top nodes for 4 studied cases. ....	122
Table A.1: Direct tensor notation (Voyiadjis and Kattan, 2006). ....	136

## Notations

$a_k$	Constant used in computing Softening curve constants
$a_p$	Softening function constant
$a_t$	Softening function constant
<b>B</b>	Conventional strain-displacement matrix
$c_l$	Softening function constant
<b>C</b>	Elastic interface stiffness matrix
<b>D<sub>0</sub></b>	Elastic stiffness matrix
<b>D<sub>tan</sub></b>	Constitutive tangent matrix
$E$	Young's modulus
$E_c$	Young's modulus of concrete
$E_{ck}$	Young's modulus of the discontinuity
$E_s$	Young's modulus of steel
$f_s$	Target softening function
$f_t$	Tensile strength
<b>F<sub>Γ</sub></b>	Force vector at the additional node
$g_f$	Dissipated energy per unit Volume
$G$	Elastic shear modulus
$G_f$	Fracture energy
$h_{ch}$	Crack band thickness
$H_{\Gamma_d}$	Heaviside jump function
$it$	Iteration number
$it_{fix}$	Limit number of iterations in Stage-1 Iteration
<b>J</b>	Jacobian matrix
$K$	Elastic bulk modulus
$K_r$	Opening stiffness
$K_{ri}$	Normal stiffness per unit area to the interface layer
$K_s$	Sliding stiffness
$K_{si}$	Shear stiffness per unit area to the interface layer
<b>K<sub>Γ</sub></b>	Discontinuity stiffness matrix
$K_\theta$	Rotational stiffness
<b>K<sub>Ω</sub></b>	Stiffness matrix for an element with embedded strong discontinuity
$\ell_{ch}$	Characteristic length parameter
$L_d$	Discontinuity length
<b>n</b>	Unit vector normal to the discontinuity ( $\Gamma_d$ )
$N_i$	Shape function for a node
<b>N<sub>Γ</sub></b>	Interpolation function of the interface element

$\mathbf{r}$	Unit vector
$r_{eff}$	Effective damage evolution parameter
$r_g$	Local coordinate range
$r_k$	Damage evolution parameter at the peak of the uniaxial stress curve
$r_p$	Damage evolution parameter
$r_{pp}$	Predictive damage evolution parameter
$r_t$	Effective damage strength parameter = $f_t / \sqrt{E}$
$\mathbf{r}_{xyz}$	Cartesian vector
$\mathbf{R}$	Rotational displacement vector
$r_0$	Effective end of the softening curve
$r_e$	Limiting damage evolution parameter ratio
$r_\zeta$	Relative shear strain intercept
$r_\sigma$	Relative shear stress
$t$	Out-of-plane thickness of an element
$\mathbf{T}_c$	Transformation matrix
$\hat{\mathbf{t}}$	Out of plane unit vector
$\mathbf{s}$	Deviatoric stress
$u_r$	Normal displacement
$u_s$	Sliding displacement
$\mathbf{U}$	Displacement vector
$\bar{\mathbf{u}}$	Continuous displacement field vector
$\tilde{\mathbf{u}}$	Enhanced displacement field vector
$[[\mathbf{u}]]$	Displacement jump vector
$\mathbf{u}^\Gamma$	Nodal displacements of the interface element
$\tilde{\mathbf{W}}$	Additional node
$\mathbf{x}_c$	Cartesian coordinate vector at the centre of a discontinuity
$\alpha_c$	Weighting parameter expresses the degree of compression under loadings
$\alpha_d$	Relative rotation to the two crack phases
$\alpha_t$	Weighting parameter expresses the degree of tension under loadings
$\beta$	Iterative step length
$\Gamma_d$	Discontinuity surface
$\delta\mathbf{U}$	Displacement increment
$\delta_{\Gamma_d}$	Dirac delta function
$\Delta r_p$	Iterative change in damage evolution parameter
$\Delta\mathbf{U}_\Gamma$	Relative displacement of the interface element
$\boldsymbol{\varepsilon}$	Strain tensor
$\boldsymbol{\varepsilon}_{fr}$	The fracture strain
$\varepsilon_k$	Strain at the peak of the uniaxial stress curve
$\varepsilon_t$	Tensile strain measure

$\boldsymbol{\varepsilon}_v$	Volumetric strain
$\widehat{\boldsymbol{\varepsilon}}$	Equivalent strain
$\widetilde{\boldsymbol{\varepsilon}}$	Crack-plane total strain
$\varepsilon_0$	Strain at the effective end of softening curve
$\zeta_{eff}$	Effective strain damage evolution parameter
$\theta$	Discontinuity angle
$\nu$	Target softening curve constant
$\mu$	Residual friction factor
$\mu_e$	Asymptotic shear friction
$\Pi$	Total potential energy
$\boldsymbol{\sigma}$	Stress tensor
$\sigma_k$	Stress to which the SUR function is asymptotic
$\sigma_p$	Smooth unloading-loading function
$\boldsymbol{\sigma}_v$	Volumetric stress
$\boldsymbol{\sigma}_0$	Effective stress tensor
$\nu$	Poisson's ratio
$\Psi_d$	Tolerance value for displacement L2 norm
$\Psi_e$	Convergence tolerance for the energy norm
$\Psi_f$	Tolerance value for out of balance force norm
$\boldsymbol{\chi}_r$	Element local coordinate
$\Omega$	Domain/body
$\omega$	Basic or scalar damage variable ( $\omega \in [0,1]$ )
$\omega_c$	Damage variable corresponds to compressive damage
$\omega_p$	SUR damage parameter
$\omega_{pf}$	Damage parameter controlling linear part of the SUR function
$\omega_t$	Damage variable corresponds to tensile damage

# Chapter 1

---

## 1.1 Introduction

Micro-cracking is a feature of quasi-brittle (QB) materials loaded beyond their elastic limit and is the primary cause of stiffness and strength degradation in materials such as concrete and rocks. Laboratory samples of quasi-brittle material frequently exhibit a post-peak softening response when loaded in tension or unconfined compression. This macro-scopic softening behaviour is sometimes referred to as material softening although it is recognised that this is a structural phenomenon, resulting from the micro-cracking, rather than a fundamental response of the material (Bažant, 1992; Karihaloo, 1995; van Mier, 1996; Bažant and Planas, 1997; van Mier, 2012).

Softening behaviour has presented researchers with two related computational challenges; namely, how to **(i)** obtain mesh-objective predictions and **(ii)** stable and converged solutions. Mathematically, these issues are a consequence of the loss of ellipticity of the governing partial differential equations (De Borst, 2001; Jirásek, 2007), when a certain degree of damage is exceeded, and are characterised by the associated stiffness matrix becoming non-positive definite (De Borst et al., 2012).

The first of the above challenges issue can be dealt with, at least to first order accuracy, by using the crack-band model of Bažant and Oh (1983). More refined means of resolving the mesh-sensitivity problems include the use of integral (Pijaudier-Cabot and Bažant, 1987; Jirásek and Marfia, 2005) and differential (Ru and Aifantis, 1993; Peerlings et al., 1996; De Borst et al., 1999; Rodríguez-Ferran et al., 2011) non-local models. However, resolving the mesh sensitivity issue does not resolve of all the stability and convergence issues associated with modelling QB

materials (Jirásek and Bauer, 2012). The second issue has not yet been fully resolved and is still a topic of intense interest in the computational mechanics community.

The nonlinear equations resulting from the finite element simulation of QB structures are frequently solved using incremental-iterative solution schemes based on Newton-Raphson (NR) algorithms (Crisfield, 1991; De Borst et al., 2012). It is the poor convergence properties of these solution schemes, when solving problems involving QB materials, which so frequently cause frustration to finite element analysts.

Many approaches have been developed for improving the efficiency and robustness of these Newton-Raphson procedures (tangent stiffness matrix is computed in every iteration). These techniques include modified Newton-Raphson (tangent stiffness matrix is only updated occasionally), Quasi-Newton approaches (tangent matrix is computed in the first iteration of each step and in subsequent iterations is obtained by a secant approximation rather than re-evaluating it at every iteration), line search algorithms and arc-length procedures for tracing the complete equilibrium path, etc. (Crisfield, 1991; Crisfield, 1997; De Borst et al., 2012).

None of the aforementioned algorithms are completely robust, nor do they fully resolve all the stability and convergence difficulties encountered when analysing QB structures. These problems are clearly expressed in the following three quotations:

- Oliver et al. (2006a) stated *“It is a very well-known that finite element formulations for modelling material failure suffer, very often from lack of robustness. Even if powerful continuation methods to pass structural unstable points are used, it is noticed that, as the material failure progresses across the solid, the condition number of the structural tangent stiffness deteriorates, the iterative Newton-Raphson fails and, eventually, the numerical simulation cannot be continued”*.
- Graça-e-Costa et al. (2013) reported that *“Localisation of initially distributed cracking is a numerical challenging task, which is difficult to accomplish with conventional iterative methods, e.g. Newton-Raphson methods”*.
- Slobbe (2015) pointed out that *“The conventional way of doing nonlinear FE analysis is by using incremental-iterative procedures, like regular or modified NR procedures, etc. However, in case of modelling failure these procedures may be unstable and convergence problems can be faced”*.

These on-going stability and convergence difficulties of incremental-iterative solution schemes based on NR have undoubtedly been behind the development of solution algorithms that avoid multiple iterations to simulate QB structures. These methods include for example the ‘implicit-explicit’ approach of Oliver et al (Oliver et al., 2006a; Oliver et al., 2008a) or modified implicit-explicit method (Prazeres et al., 2015). The implicit-explicit methods employ a projected state variable, e.g. a damage parameter, to determine a predicted consistent tangent matrix. An alternative approach that also avoids using iterations, is the ‘Sequentially Linear Approach (SLA)’, which was proposed by Rots (2001). This method imposes an increment of damage instead of an increment of displacement or force, and uses a ‘saw-tooth’ function to replace the post-peak softening function. The SLA method has been improved over years by a number of investigators i.e. (Rots and Invernizzi, 2004; Rots et al., 2008; Eliáš et al., 2010; Graça-e-Costa et al., 2012; Vorel and Boshoff, 2015).

The numerical robustness of implicit-explicit and SLA approaches cannot be questioned and their effectiveness at dealing with a certain class of problem has been demonstrated. Despite the fact that there are considerable benefits to using these approaches, they can result in non-smooth responses, and would require further development before being able to cope well with constitutive models that include non-linear crack closure in combined shear and normal modes. Currently they are not compatible with non-linear plasticity models for other materials, which would be an issue for solving soil-structure problems.

The issue of poor convergence properties and the lack of robustness of existing solution schemes, when solving problems involving QB materials, provides the main motivation for the work of this thesis.

The second motivation for this work results from a major drawback of the nonlocal integral and gradient models (which involve a length scale related to the fracture process zone). The particular issue in question is that these non-local approaches require a sufficiently fine resolution of the localized zone (several elements across the thickness of the localized zone) to accurately capture the deformation of the localized region and guarantee mesh objectivity (Mosler and Meschke, 2004; Foster et al., 2007; Dujc et al., 2010; Mosler et al., 2011). This requirement can make the

simulation of large structures computationally very expensive, especially when the location of the strain localization is not known a priori (Oliver et al., 2004; Mosler, 2006; Parvaneh and Foster, 2016).

Therefore, the strong discontinuity approach has been developed in recent years and has become a topic of intense interest for the simulation of material failure either by the embedded SD approach or by XFEM (Belytschko and Black, 1999; Oliver et al., 1999; Borja, 2000; Jirásek, 2000; Oliver et al., 2003b; Oliver et al., 2006b). The main characteristic of the embedded SD approach is the enhancement of finite elements with additional local degrees of freedom to capture the displacement jumps associated with the discontinuities (Armero and Linder, 2008). Indeed, one main advantage of the embedded SD approach, which is considered in this study, is the local (element) nature of this enhancement, which does not affect the number of global equations, since static condensation is performed at the element level (Linder and Armero, 2007; Dias-da-Costa et al., 2010).

It should be noted that most of available embedded discontinuities finite elements approaches are based on constant strain triangle with constant displacement jumps. Quadrilateral elements with linearly varying kinematics of displacement jumps are less common (Armero and Linder, 2008; Dujc et al., 2013; Dias-da-Costa et al., 2009b). A new computationally convenient formulation for introducing discontinuities into elements is described in this thesis.

## **1.2 Aims and objectives**

There are two main aims of this study. The first aim is to develop a robust incremental-iterative solution scheme for non-linear finite element analysis of quasi-brittle materials. The second aim is to develop a new formulation for quadrilateral elements with embedded strong discontinuities. In order to fulfil these main aims, the following specific objectives are addressed in this thesis:

1. Develop a robust incremental-iterative solution scheme, based on a Newton type solution procedure, that employs a smooth unloading-reloading (SUR) function as the basis for an approximate tangent matrix.

2. Employ the proposed SUR approach with a finite element damage model.
3. Develop new acceleration techniques to improve the convergence properties of the SUR approach. ..
4. Assess the robustness and efficiency of the proposed SUR approach by comparing its performance with that of a reference ‘secant’ model for a range of idealised examples.
5. Develop a new formulation for elements with embedded strong discontinuities to simulate failure in quasi-brittle structures.
6. Evaluate the characteristics and efficiency of the proposed SD formulation by comparing its performance with those of a model with interface elements and a smeared crack model.
7. Develop a tractable expression for calculating the element characteristic length parameter.

### **1.3 Outline of the thesis**

The remainder of this thesis is arranged as follows described below.

**Chapter 2** comprises 5 main parts; the first part provides historical background on the finite element modelling of cracking using discrete and smeared crack concepts. Then, constitutive models for concrete materials are discussed, with an emphasis on the type of continuum damage model used for the work described in this thesis. After this, issues associated with strain localization are highlighted. Non-linear finite element solution techniques for simulating quasi-brittle materials are reviewed in Section 2.4. Finally, Section 2.5 reviews previous work on the strong discontinuity approach

**Chapter 3** proposes a robust incremental-iterative method, named the smooth unloading-reloading (SUR) approach, for the numerical simulation of quasi-brittle materials. This chapter has 7 Sections: Section 3.2 describes the continuum damage

model used in this study. The proposed approach for the nonlinear finite element analysis of quasi-brittle materials is described in Section 3.3, after which the method used for fracture energy computations is given. A new method for computing the characteristic length parameter for triangular and quadrilateral elements is presented in Section 3.4, after which a set of convergence criteria are given in Section 3.5. Section 3.6 presents five selected numerical examples used in to assess the performance of the proposed incremental-iterative method. In the last section of this chapter, results are discussed and some conclusions are drawn.

Three acceleration approaches are described in **Chapter 4** for improving the convergence properties of the proposed SUR method described in chapter 3. The performance of these acceleration algorithms is demonstrated using four numerical examples. The advantages of using these three acceleration techniques are discussed and compared with each other.

A new formulation for elements with embedded strong discontinuities to model failure of quasi-brittle materials is presented in **Chapter 5**. This chapter contains 7 Sections: A brief summary of the basic kinematics associated with the strong discontinuity approach is presented in Section 5.2. The derivation of the new formulation for 2D quadrilateral elements is described in detail in Section 5.3. The formulation of a particular interface element, used in some comparisons, is given in Section 5.4. The damage function used to govern the nonlinear behaviour of discontinuities is described in Section 5.5. Section 5.6 presents several representative numerical simulations to illustrate the performance of the newly proposed SD approach. The chapter finishes with discussion and conclusion of the developed approach in Section 5.7.

Finally, based on the work presented in this thesis, overall conclusion and suggestions for further work are given in **Chapter 6**.

## 1.4 List of publications

### a) Journal articles

1. **Alnaas, W. F.** & Jefferson, A. D. 2016. A smooth unloading–reloading approach for the nonlinear finite element analysis of quasi-brittle materials. *Engineering Fracture Mechanics*, **152**, 105-125.
2. **Alnaas, W. F.** & Jefferson, A. D. 2016. A robust method for the simulation of quasi-brittle materials. *ICE - Engineering and Computational Mechanics*. DOI: 10.1680/jencm.15.00019, p.1-20.
3. Jefferson, A. D., Mihai, I. C., Tenchev, R., **Alnaas, W. F.**, Cole, G. & Lyons, P. 2016. A plastic-damage-contact constitutive model for concrete with smoothed evolution functions. *Computers & Structures*, **169**, 40-56.

### b) National and International Conferences

1. **Alnaas, W. F.** & Jefferson, A. D. Nonlinear finite element analysis of quasi-brittle materials, *Proceedings of the 23<sup>rd</sup> UK International Conference on Computational Mechanics in Engineering (ACME-2015)* , 8-10 April 2015, Swansea, UK.
2. **Alnaas, W. F.** & Jefferson, A. D. A Smooth unloading-reloading approach for modelling quasi-brittle failure, *IV International Conference on Computational Modeling of Fracture and Failure of Materials and Structures (CFRAC-2015)*, 3–5 Jun 2015, Cachan, France.
3. Jefferson, A. D., Mihai, I. C. & **Alnaas, W. F.** The benefit of smoothing the unloading-reloading response and rough crack-contact relationships in a finite element concrete model, *XIII International Conference on Computational Plasticity Fundamentals and Applications (COMPLAS-XIII)*, 1–3 Sep 2015, Barcelona, Spain.

4. **Alnaas, W. F.** & Jefferson, A. D. Acceleration techniques for nonlinear finite element analysis of quas-brittle materials, *Proceedings of the 24<sup>th</sup> Conference on Computational Mechanics (ACME-2016)*, 31 Mar-01 Apr 2016, Cardiff, UK.

# Chapter 2

## Literature review

---

### 2.1 Finite element method for modelling cracks

The Finite element method (FEM) has been applied to model fracture in quasi-brittle materials such as concrete since the late of 1960s. The two dominant methods used in finite element modelling of cracking are the discrete crack approach and the smeared crack approach (De Borst, 1997). In the former approach, a crack is treated as a geometrical entity (Rots, 1991; Jirásek, 2011); whereas in the latter approach, the cracked material is assumed to remain as a continuum with continuous displacement field, and cracks are taken into account by capturing the deterioration process through a constitutive relationship, thereby smearing the crack over the a portion of the continuum (De Borst et al., 2004). The following subsections of this chapter provide an brief overview of some historical developments of these two methods and highlight their advantages and disadvantages.

#### 2.1.1 Discrete crack approach

The first discrete crack model was introduced in 1967 by Ngo and Scordelis who studied a simply supported reinforced concrete beam. In their study, cracks were introduced into the finite element mesh by separating elements along the crack trajectory (Rots and Blaauwendraad, 1989). In the early versions of this approach, cracks were restricted to propagate along element boundaries, i.e. between existing elements. Thus, the response was strongly mesh-dependent as cracks could only form along the element boundaries (Cervera and Chiumenti, 2006b). However, Ingraffea and his group at Cornell University in USA developed a technique which

automatically redefines the mesh as cracks propagate (Ingraffea and Manu, 1980; Ingraffea and Saouma, 1985; Wawrzynek and Ingraffea, 1987; Swenson and Ingraffea, 1988). The basic idea of the remesh method is that when a parameter of interest (i.e. stress intensity factor, energy release rate or crack opening displacement) exceeds a critical value, an existing crack advances by a small increment (Xu and Waas, 2015). Despite the fact that the automatic remeshing method allows the mesh dependency to be reduced or even eliminated, this method requires complex code for the remeshing and has a relatively high computational cost (Cervera and Chiumenti, 2006a; Nguyen et al., 2008).

The complexity of code required to continuously change element topologies to model the formation and growth of crack was the main reason behind the development of alternative approaches for modelling cracking. These include meshless methods, a comprehensive review of which can be found in Nguyen et al. (2008), the extended finite element method (X-FEM), which developed by Belytschko and his co-workers in Northwestern school (Moës et al., 1999; Belytschko and Black, 1999; Sukumar et al., 2000), an exhaustive review of recent advances in X-FEM is reported in Fries and Belytschko (2010), and element based strong discontinuity approaches (SDA) (Simo et al., 1993; Jirásek, 2000) which is discussed in Section 2.5. These methods allow the entire crack to be represented independently of the mesh.

Nevertheless, the large computational demand compared with FE methods as well as the complications that ensue when describing phenomena like crack branching, coalescence and curved crack boundaries in three dimensions tend to limit the use of the above mentioned methods and favour the use of the smeared crack approach (Shah et al., 1995; De Borst et al., 2004; May et al., 2015). In summary, it can be argued that the discrete crack approach is most suitable for cases where the behaviour of a structure is governed by a few dominant cracks; and it may not be very effective for RC structures in which the presence of reinforcement generally leads to diffuse cracking (Oliver et al., 2008b).

### 2.1.2 Smearred crack approach

The smeared crack approach was introduced by Rashid in 1968 to model cracks in prestressed concrete pressure vessels. This approach comes directly from computational continuum mechanics, so the criteria of crack initiation and propagation is mostly based on failure criteria expressed in terms of stresses or strains (Bažant and Planas, 1997). The simple concept of the smeared crack approach is that displacement jumps across cracks are smeared over the effective finite elements and the behaviour of the crack is established through a constitutive relationship (Cervera et al., 2011). In the smeared approach, cracks are modelled by modifying the material properties at the integration points of cracked finite elements (Jirásek, 2011). In other words, stress and strain are measured at sampling points (i.e. Gaussian integration points) of an element, thus when the crack initiates or grows, the mechanical properties (stiffness and strength) are reduced at these integration points according to a softening stress-strain relationship (De Borst et al., 2004). This approach has become well-known and widely accepted because it is generally much more convenient to represent cracks by changing the constitutive properties of individual finite elements than to change the topography of an entire finite element mesh.

Over the years, a number of numerical and practical problems have surfaced with the application of the smeared crack models. Among these is spurious mesh dependency (Bažant, 1976; Crisfield, 1982a). This dependency can relate to both the fineness of the mesh and to the orientation of the elements. However, this problem can be greatly alleviated, although not fully resolved, by relating the governing constitutive softening function to the element size and orientation. This is most readily accomplished using the crack-band theory (Bažant and Oh, 1983), with an orientation dependent element characteristic length (Oliver, 1989; Volokh, 2013). Section 2.3 reviews these issues in more depth.

The smeared crack approach has been widely used for modelling concrete materials, and is available in many commercial FE packages (e.g. ABAQUS, ANSYS, DIANA and LUSAS) (Bažant, 2002; Cervera and Chiumenti, 2006b; Cervera, 2008; Slobbe et al., 2014; Jefferson et al., 2016).

However, it can be stated that both discrete crack and smeared crack approaches have their domain of application. Discrete crack models are appropriate for modelling one or more dominant crack, whilst smeared crack models can simulate diffuse cracking patterns that arise due to the heterogeneity of the concrete structures, e.g. reinforcement concrete (ACI, 1997; De Borst et al., 2004).

## **2.2 Concrete modelling**

During recent decades, much effort has been devoted to the development of advanced constitutive models to simulate quasi-brittle materials such as concrete, rocks, ceramics, etc. The behaviour of concrete materials is highly complex and investigators have been carrying out research to better understand and describe its behaviour. Before start the review of available constitutive models, it is necessary to highlight some features of concrete material behaviour that provide the basis for the constitutive models.

### **2.2.1 Mechanical behaviour of Concrete**

Concrete is a heterogeneous material which exhibits complex nonlinear mechanical behaviour under different loading conditions (Karihaloo, 1995). For instance, under uniaxial compression, concrete exhibits considerable ductility and non-linearity prior to reaching the peak stress, whereas in tension, the behaviour of concrete is quasi-brittle. In addition, the uniaxial compressive strength of concrete materials is approximately 10 to 20 times greater than its uniaxial tensile strength (Torrenti et al., 2013). Furthermore, when concrete reaches its compressive capacity, the loss of stiffness and strength occurs in all directions; while in tension, the degradation of strength is predominately confined to one direction (van Mier, 1996).

Moreover, the failure of quasi-brittle materials in tension and unconfined compression is characterised by ‘strain softening’, which describes the post-peak gradual decline of stress at increasing strain (or relative displacement). This structural phenomenon is accompanied by a reduction of the unloading stiffness of the material and permanent deformations, which localize in relatively narrow zones

often called cracks. Whereas when concrete is subjected to compression under high confinement, its behaviour is characterised by a ductile hardening response, in which stress increases with increasing strain (Grassl et al., 2013). Nevertheless, concrete also exhibits strain softening beyond the peak stress in compression. The typical failure modes in concrete are cracking in tension and unconfined compression and crushing in compression (Grassl and Jirásek, 2006).

When concrete is subjected to monotonic tensile or compressive loading beyond the elastic limit, irreversible deformations occur. This can be attributed to interfacial slips between mortar and aggregate when macro-cracks formed and the crushing of the mortar (Chen and Han, 2012). Therefore, due to the distinctive behaviour of concrete under tensile and compressive loadings, researchers have developed constitutive models with different levels of complexity and applicability in order to take into account these aforementioned differences in the concrete behaviour.

### **2.2.2 Constitutive models for concrete**

A large number of constitutive models to describe the nonlinear response of concrete structures under different conditions have been developed over the last few decades. These constitutive models, which are briefly reviewed in this section, fall generally into three categories: damage models, plasticity models and combination of plasticity and damage models. Constitutive models aim at simulating the macroscopic features of concrete materials, in which they describe the relationship between stresses and strains of a material. However, developing a single constitutive model that is able to describe all aspects of concrete behaviour is still quite a challenging task due to the complexity of concrete's behaviour. Indeed, the choice of a constitutive model and the knowledge on its deficiency and limitations is crucial to obtaining model predictions that are in a satisfactory agreement with experimental observations.

Damage models are based on the concept of a gradual reduction of the elastic stiffness. Thus, damage models can be suitable for describing stiffness degradation and the so-called unilateral effect (also referred to as damage deactivation, crack closure effects or stiffness recovery) (La Borderie et al., 1992; Comi and Perego, 2001; He et al., 2015). Extensive research has been conducted on modelling concrete

within the framework of continuum damage mechanics, in which damage is considered as either isotropic or anisotropic. However, it should be mentioned that continuum damage model alone is not able to describe irreversible deformations and inelastic volumetric expansion (dilatancy) in the case of high confined compressive loading (Grassl and Jirásek, 2006; Gernay et al., 2013). See subsection 2.2.3 for more details on damage models.

Plasticity-based constitutive models employ a rule for decomposition of the total strain, which is traditionally assumed to be the sum of elastic strain and accumulated plastic strain. The split of strain into elastic and plastic components provides a convenient means of simulating inelastic deformations. Furthermore, plasticity models are governed by a yield (or failure) function, which is normally described in stress space and bounds an elastic region, a hardening rule, which defines the evolution of the yield surface, and also one or more flow rule to define the evolution of a set of internal variables that uniquely describe the material state. Plasticity models vary in the definition of the yield function as well as hardening and flow rules. Good examples of plasticity models are those proposed by Willam and Warnke (1975), Han and Chen (1987), Etse and Willam (1994), Feenstra and De Borst (1995), Grassl et al. (2002), etc. Many other reviews and references therein can be found in Chen (2007).

Although plasticity models can adequately describe the elastic region, failure conditions and the development of permanent stains, they fail to describe the stiffness degradation due to cracking, as well as other related effects like stiffness recovery upon crack closure (i.e. the so-called ‘unilateral effect’) (Comi and Perego, 2001; Grassl et al., 2013; Omid and Lotfi, 2013).

In spite of the huge progress made in both plasticity and damage models, using neither of these models alone would be able to simulate well all of mechanical behaviour of concrete (Ibrahimbegovic, 2009). For this reason, great efforts have been made to link together the advantages of plasticity and damage theories in a single coupled plastic-damage model. In this combined approach, damage theory is used to model the material deterioration caused by micro-cracks propagation, while the permanent deformations can be captured using plasticity theory (Nguyen and Houlsby, 2008; Nguyen, 2005), see Figure 2.1.

Plastic-damage models usually combine stress-based plasticity with either isotropic (Grassl and Jirásek, 2006; Omid and Lotfi, 2013) or anisotropic damage theory (Ortiz, 1985; Meschke et al., 1998; Jefferson, 2003; Grassl et al., 2013). However, it has been noted by many authors that using anisotropic damage models with plasticity models for modelling concrete is not straightforward due to inherent complexities of the required numerical algorithms. Therefore, isotropic damage models have been widely employed in combination with plasticity model for simulating concrete structures. It should be mentioned here that plasticity and plastic-damage models have not be used in the work described in this thesis and thus they are only briefly reviewed.

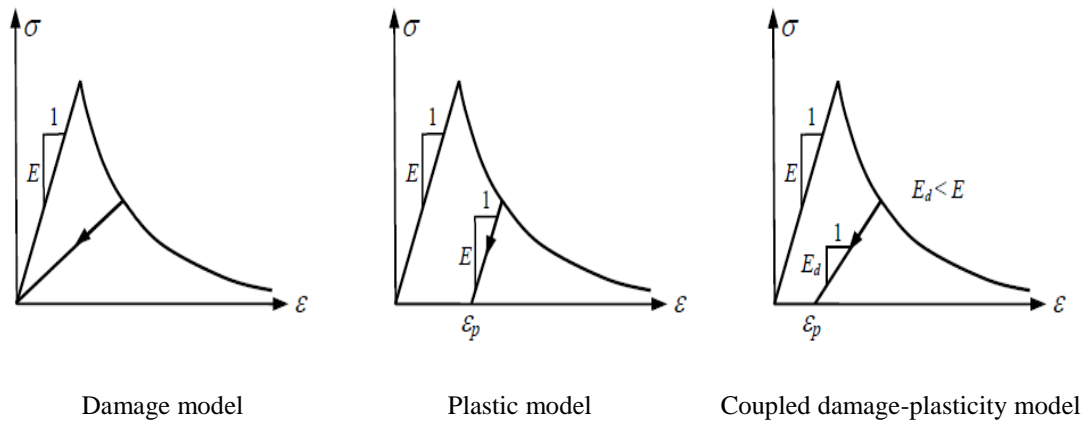


Figure 2.1: Stress-strain curve in damage, plastic and coupled damage-plastic models (Nguyen, 2005).

In summary, there is no doubt that the most appropriate constitutive models for a realistic description of concrete materials behaviour are those based on combination of plasticity and damage models. However, damage models alone are often capable of providing an adequate description of concrete behaviour up to failure for a wide range of loading conditions, especially when the tensile loading is the main cause of the structural failure (Comi and Perego, 2001; Carol et al., 2001; Voyiadjis et al., 2008). As a consequence, continuum damage models are the most used for describing the constitutive behaviour of quasi-brittle materials (Jirásek and Bauer, 2012).

### 2.2.3 Continuum damage mechanics

The term “continuum damage mechanics” (CDM) was coined in 1972 by Hayhurst. However, the essential concept of CDM was first introduced by Kachanov in 1958 to model creep damage in metals using the effective stress concept. The effective stress concept is based on considering a fictitious undamaged configuration of a body and comparing it with the actual damaged configuration (Kattan and Voyiadjis, 2001). Continuum damage mechanics can be defined as a constitutive theory that describes the progressive loss of material integrity due to the propagation and coalescence of micro-defects such as micro-cracks and micro-voids. The influences of these defects and their growth within the microstructure of a material lead to a degradation of the material stiffness observed on the macroscopic scale (Jirásek, 2011).

Continuum damage theory uses a set of damage variables to describe the local loss of material integrity. The damage variable can be related to stress or strain through a damage evolution law. There are many ways to phenomenologically define, or micromechanically derive, damage variables. The damage variable can be as a singular scalar variable (Mazars and Lemaitre, 1985; Oliver et al., 1990; Jirásek and Zimmermann, 1998), a single subdivided scalar variable, or separate two scalar variables, that distinguish between tension and compression damage mechanisms (Mazars, 1986; Faria et al., 1998; Comi and Perego, 2001) , a vector (Krajcinovic and Fonseka, 1981), a second-order tensor (Murakami and Ohno, 1981) and a fourth-order tensor parameters or higher (Chaboche, 1981; Litewka and Debinski, 2003). The choice of which type of damage variables should be used depends on the nature of the problem (Lemaitre and Chaboche, 1990).

The damage of concrete is an anisotropic phenomenon in reality. Nevertheless, isotropic damage models have been extensively used in research because of their simplicity and ability to capture the main macroscopic features of the behaviour of concrete materials in an approximate manner (Mazars, 1986; Tao and Phillips, 2005; Richard et al., 2010; He et al., 2015). An isotropic damage model has been used for the work described in this thesis.

### 2.2.3.1 Mathematical description of Isotropic damage models

As the name suggests, isotropic damage models are based on the assumption that the stiffness degradation is isotropic i.e. the stiffness moduli corresponding to different directions decrease proportionally and independently of the direction of loading. Moreover, Poisson's ratio is generally assumed to remain unaffected by damage in such models. The classical constitutive equation for this type of model is as follows:

$$\boldsymbol{\sigma} = (I - \omega) \mathbf{D}_0 : \boldsymbol{\varepsilon} \quad (2.1)$$

where  $\boldsymbol{\sigma}$  and  $\boldsymbol{\varepsilon}$  are the stress and strain tensors, respectively,  $\mathbf{D}_0$  is the elastic material stiffness tensor,  $\omega$  denotes the scalar damage variable, noting that  $\omega \in [0, 1]$ , here “:” denotes tensor contraction. Tensor and matrix notations are defined in Appendix A.

In the strain-driven version of the model, the damage variable explicitly depends on the maximum previously reached level of a scalar measure of a strain, called the equivalent strain ( $\widehat{\varepsilon}$ ). The maximum level of equivalent strain, i.e. ( $\kappa$ ) plays the role of an internal variable, and is formally described by loading-unloading conditions:

$$f(\boldsymbol{\varepsilon}, \kappa) \equiv \widehat{\varepsilon}(\boldsymbol{\varepsilon}) - \kappa \leq 0; \quad \dot{\kappa} \geq 0; \quad \dot{\kappa} f(\boldsymbol{\varepsilon}, \kappa) = 0 \quad (2.2)$$

The isotropic damage model of Mazars (1986) and Mazars and Pijaudier-Cabot (1989) is one of the most popular isotropic models that was designed specifically for concrete. The model introduces two damage variables to take into account the dissymmetric behaviour of concrete under tension and compression. One damage variable ( $\omega_t$ ) is associated with tensile damage and the other ( $\omega_c$ ) corresponds to compressive damage. These two damage parameters are evaluated from tensile and compressive evolution functions which are assumed to be governed by the equivalent strain. The equivalent strain is a scalar measure of the strain level. The total damage scalar ( $\omega$ ) is assumed to be a linear combination of the tensile damage and the compressive damage, and computed as in the following equation.

$$\omega = \alpha_t \omega_t + \alpha_c \omega_c \quad (2.3)$$

where the coefficients  $\alpha_t$  and  $\alpha_c$  are weighting parameters that express the degree of compression and tension under different loading conditions. For instance,  $\alpha_t = 0$  for pure hydrostatic compression, but  $\alpha_t = 1$  for pure tension.

Another good example of an isotropic damage model with two damage variables to distinguish between tensile and compressive damage was proposed by Comi and Perego (2001). Their model reduces the bulk modulus by factor  $(1 - \omega_t)$  if the volumetric strain is positive and by  $(1 - \omega_c)$  if it is negative, while the shear modulus is always reduced by  $(1 - \omega_t)(1 - \omega_c)$ . In this model the secant stiffness remains isotropic, but with a variable Poisson ratio. The stress-strain law is defined in terms of volumetric stress ( $\sigma_v$ ) and deviatoric stress ( $\mathbf{s}$ ) quantities as follows:

$$\sigma_v = (1 - \omega_t) 3K \langle \boldsymbol{\varepsilon}_v \rangle - (1 - \omega_c) 3K \langle -\boldsymbol{\varepsilon}_v \rangle \quad (2.4)$$

$$\mathbf{s} = (1 - \omega_t)(1 - \omega_c) 2G(\boldsymbol{\varepsilon}_d) \quad (2.5)$$

where  $\langle \boldsymbol{\varepsilon}_v \rangle$  denotes the positive part of volumetric strain,  $-\langle -\boldsymbol{\varepsilon}_v \rangle$  is its negative part and  $\boldsymbol{\varepsilon}_d$  is the deviatoric strain.  $K$  is the elastic bulk modulus and  $G$  is the elastic shear modulus.

Moreover, the isotropic damage model of Oliver et al. (1990) is also one of the most widely cited and most effective isotropic damage models for the simulation of concrete. The model uses a scalar to measure the stiffness degradation of the material. Oliver et al.'s (1990; 2002; 2006a) model was employed in the work reported in this thesis and a full description of the model is given in Chapter 3 of this thesis.

### 2.3 Localization of strain

Failure of quasi-brittle materials is preceded by the development of nonlinear fracture process zones, which can be macroscopically described as zones of highly localized strains. The degradation of strength and stiffness due to the progressive growth of micro-cracks and their coalescence is conveniently described by models based on continuum damage mechanics, as discussed in the previous section, (Jirásek et al., 2004; Cervera et al., 2010). However, when conventional damage models are applied with the finite element method to describe strain softening behaviour, issues associated with mesh-dependent behaviour and zero energy dissipation are encountered (Bažant, 1976; Needleman, 1988; Jirásek and Bauer, 2012).

It was found that damage generally localises to a narrow band, e.g. a region of only one element width independent of the element size. Therefore, numerical results obtained with standard continuum constitutive laws suffer from lack of objectivity to spatial discretization (Jirásek and Patzák, 2002; Cervera and Chiumenti, 2006b; Murakami, 2012). Furthermore, when continuum models with fixed stress-strain evolution relationships are applied in finite elements, the energy dissipated per unit volume of material under analysis is constant; thus different damage zone widths result in different energy dissipations during the fracture process. Therefore, the total amount of energy dissipated during the failure process vanishes for infinitesimally small elements, which is physically unacceptable (Lin and Whu, 1992; Karihaloo, 1995; Bažant and Planas, 1997).

From the mathematical point of view, the above pathological features of using conventional continuum mechanics are caused by the fact that, beyond a certain level of accumulated damage, the governing differential equations lose their ellipticity. Thus, the boundary value problem becomes ill-posed. From the numerical standpoint, ill-posedness of the boundary value problem is manifested by pathological sensitivity of numerical results to the discretization (De Borst, 1997; De Borst, 2001; Jirásek, 2007; Jirásek, 2011).

One remedy for the spurious mesh-size sensitivity is the crack band model of Bažant and Oh (1983). Indeed, the crack band model is the simplest remedy and the most

frequently used in practical applications to eliminate the pathological dependence of the solution on the finite element meshes and ensure that the global energy dissipation in fracture process is captured correctly (Jirásek and Bauer, 2012). In fact, the crack band model is inspired by the fictitious crack model developed by Hillerborg et al. (1976), which ensured a mesh-independent energy release upon crack propagation. The advantage of the crack band model is that it can be easily implemented in finite element codes, since the formulation in this model remains local and the algorithmic structure of the FE code requires only minor adjustment relatively to the amount of code that needed to evaluate the stress and stiffness corresponding to a given increment of displacement (Bažant, 2002; Červenka et al., 2005; Cervera and Chiumenti, 2006b; Slobbe et al., 2013).

The crack band model of Bažant and Oh (1983) is based on the assumption that strains localize to a band one element in width, irrespective of the finite element size. The basic concept of this model is to modify the constitutive law in such a way that the energy dissipated over a completely fractured finite element can be equated to a given value that relates to the fracture energy of the material and on the element geometric dimension (Cervera and Chiumenti, 2006a; Cervera and Chiumenti, 2006b). In other words, to make sure that the dissipated energy per unit volume ( $g_f$ ) is equal to the fracture energy ( $G_f$ ), which considered as a material property, the fracture energy  $G_f$  is smeared out over the width of area in which a crack localizes, thus,  $g_f = G_f / \ell_{ch}$ . This means that the governing stress-strain evolution function is no longer unique, but is modified according to the width of the numerically resolved band of localized inelastic strain ( $\ell_{ch}$ ), which in turn depends on the mesh refinement (Jirásek et al., 2004; Jirásek and Bauer, 2012). The fracture energy can be defined as the amount of energy required to create one unit of surface area of a crack (Hu and Wittmann, 1992).

More refined remedies which can avoid not only mesh size sensitivity but also mesh orientation bias were developed and called localization limiting techniques. These methods prevent damage localizing into a zone of zero volume by introducing, either implicitly or explicitly, a length scale (material characteristic length) to the governing equations. Thus, the damage is forced to grow in an arbitrarily small zone

with a finite width that is independent of spatial finite element discretization (Sankar et al., 2013). As the enrichments of these methods enforce a certain minimum width of numerically resolved process zone, they are called localization limiters. These regularization techniques include, for instance, integral-type nonlocal models (Pijaudier-Cabot and Bažant, 1987; Bažant and Pijaudier-Cabot, 1988; Bažant and Jirásek, 2002; Jirásek and Marfia, 2005) and nonlocal gradient models (Peerlings et al., 1996; Peerlings et al., 2001; Rodríguez-Ferran et al., 2011). In non-local models, the stress at a point depends not only on the strain at the same point but also on the strains in the neighbourhood of that point (Bažant and Planas, 1997). The localization limiters are beyond the scope of this study. It should be pointed out here that, these approaches can overcome the mesh-size and mesh bias issues, but they are unable to resolve all the stability and convergence problems associated with modelling quasi-brittle materials, as it will be discussed in the next section.

## **2.4 Solution techniques for nonlinear finite element analysis**

Stability and convergence problems are frequently encountered in nonlinear finite element solutions when using material models that include strain softening behaviour, independent of the constitutive model adopted (Crisfield, 1984; De Borst, 1987; Bažant and Cedolin, 2010). As a consequence, the nonlinear finite element simulation of quasi-brittle structures is a truly numerical challenging undertaking in the computational mechanics community. In this section, the most well-known numerical solution techniques for nonlinear finite element analysis of structures with softening materials are discussed.

The most commonly used solution technique in nonlinear finite element (FE) codes is the Newton-Raphson (NR) method (Crisfield, 1997). In the NR procedure, the applied load is divided into small increments, and the displacement increment within each step is computed by using the tangent stiffness matrix. The resistant force can be calculated by accumulated displacement, and the out-of-balance force vector can be determined as the difference between the applied and the resistant forces. When both the out-of-balance force and the residual displacements errors, measured for instance by Euclidean norms ( $L_2$ ), are less than a specified tolerance, convergence is

assumed to be obtained. If convergence criteria are not satisfied, the residual force vector is re-evaluated (the stiffness matrix is updated) and thus a new solution is obtained. This iterative procedure continues until the problem converges, then next load increment is applied (Zienkiewicz and Taylor, 2000).

However, if a full Newton solution procedure or even its modified form is used for a problem that involves strain softening, the tangent stiffness matrix becomes non-positive definite and the solution process can diverge and break down or simply fail to converge (Crisfield and Wills, 1988; De Borst et al., 2012). Indeed, in the initial time-steps of a nonlinear analysis, before any cracking occurs, the tangent stiffness matrix is linear elastic and thus positive definite. In the subsequent steps, micro-cracks initiate and form, therefore, the associated equilibrium solutions can become singular or non-unique, and thus the tangent stiffness matrix loses its positive definiteness. As a consequence, numerical instability and divergence may occur at these time-increments of the Newton-based incremental-iterative solution schemes (Crisfield, 1991; Nguyen, 2005; Oliver et al., 2006a; Graça-e-Costa et al., 2012; Graça-e-Costa et al., 2013; Pohl et al., 2014; Slobbe, 2015).

Although the divergence of the solution process can be avoided if a secant stiffness matrix is employed in place of the true tangent stiffness matrix; however, with the secant approach, the number of iterations needed to satisfy a given convergence criterion can become very large and sometimes it proves impossible to obtain a converged solution (Bathe and Cimento, 1980; Crisfield, 1997).

Many approaches have been made to improve the efficiency of these NR procedures and to improve their robustness (Dennis and Moré, 1977; Crisfield, 1982b; Ma and May, 1986; Crisfield, 1991; Crisfield, 1997; De Borst et al., 2012). These techniques include, for instance, line search algorithms, which are one of the most effective techniques for speeding up the convergence of Newton methods (Matthies and Strang, 1979; Crisfield, 1982b; Ma and May, 1986; Crisfield, 1991; De Borst et al., 2012). Line search methods attempt to stabilize NR iterations by shrinking or expanding the current displacement increment to minimize the resulting out-of-balance forces and/or residual displacements. The rationale behind the line search approach is that the direction (i.e.  $\delta\mathbf{U}$ ) found by the NR method is to some extent a good direction, but the step size is not optimal. Thus, it is much cheaper to find the

best point along the direction  $\delta\mathbf{U}$  by several computations of residual than to compute a new direction by using a new Jacobian matrix (Wriggers, 2008; Belytschko et al., 2013). Therefore, before proceeding to the next direction, in the line search method, a measure of the residual is minimized along the line. The displacements are updated according to:

$$\mathbf{U}^i = \mathbf{U}^{i-1} + \beta \delta\mathbf{U} \quad (2.6)$$

where  $\mathbf{U}^{i-1}$  is the displacement vector at the last iteration,  $\beta$  is a scalar which controls the iterative step length and  $\delta\mathbf{U}$  is the displacement increment. We find the parameter  $\beta$  so that  $\mathbf{U}^{i-1} + \beta \delta\mathbf{U}$  minimizes some measure of the residual along the line. However, in cases when the current search direction is poor and the out-of-balance forces are non-smooth functions of displacements, line search techniques may be of limited use (Daichao et al., 2002).

In addition, Quasi-Newton methods are also among the most widely used Newton-type methods for improving the convergence properties with a modest computational effort. Essentially, quasi-brittle methods do not require explicit reformation of the tangent matrix at every single iteration, instead the stiffness matrix or its inverse are continuously updated as the iterations proceed. In fact, quasi-newton algorithms attempt to compromise between the standard NR and modified NR methods for computing the stiffness matrix (Crisfield, 1991). Since a detailed description of line search and quasi-brittle methods goes beyond the scope of this literature, only the basic ideas behind the line search and quasi-newton methods are given. A comprehensive review of all of the aforementioned incremental-iterative Newton-based solution schemes can be found the following text books (Crisfield, 1991; Crisfield, 1997; Wriggers, 2008; De Borst et al., 2012).

When the global response of a structure softens and exhibits ‘snap-back’ behaviour, arc-length procedures can allow the complete equilibrium path to be traced. The arc-length method was originally introduced by Wempner (1971) and Riks (1979), with modifications being introduced by a number of researchers, i.e. (Crisfield, 1981; Crisfield, 1983; De Borst, 1987; Crisfield and Wills, 1988; May and Duan, 1997;

Hellweg and Crisfield, 1998; Ritto-Corrêa and Camotim, 2008; Verhoosel et al., 2009), The central concept of the arc-length method is that the solution path is forced to remain within the vicinity of the last converged equilibrium point. This can be done by introducing an additional constraint equation for the incremental load multiplier, which plays the role of an extra degree of freedom in the global linearized equilibrium equations. Various constraint methods have been proposed such as direct or indirect displacement control methods. The indirect displacement method is used in situations when a structure exhibits snap-back behaviour (Jirásek and Bazant, 2002). Indeed, the choice of an appropriate constraint equation in the arc-length method is crucial and affects the convergence properties decisively (Crisfield, 1997).

Another approach for tracing global snap-back is Ladeveze's Large Time Increment method (LATIN) (Ladeveze, 1999). The method is a non-incremental-iterative approach and builds the solution using a local and global phase. A key characteristic of the LATIN method is that the whole loading process is iteratively calculated in a single time increment, and at each iteration the algorithm provides an approximation of the solution over the entire time domain (Dureisseix et al., 2003). The LATIN has undergone significant development in recent years (Kerfriden et al., 2009; Vandoren et al., 2013). Generally, it can be stated that the use of the LATIN method is not widespread in the computational mechanics community and its application in modelling softening materials is limited (Vandoren et al., 2013). It should be mentioned here that tracing snap-back behaviour is not in the focus of the present work, as a result, only brief introduction of most frequently used approaches to trace the snap-back response of strain softening materials were given.

As a response to the stability and convergence difficulties of incremental-iterative solution methods, researchers have developed solution algorithms that avoid multiple iterations. These methods include the 'Sequentially Linear Approach' (SLA), which was introduced by Rots (2001). In the SLA method, the softening stress-strain curve is approximated by a saw-tooth diagram of positive slopes, and the incremental-iterative process is replaced by a scaled sequence of linear analysis. In every analysis, the most critical element is traced, the stiffness and strength of that element are reduced according to the saw-tooth curve, and the process is repeated (Slobbe et al., 2013). The sequence of scaled critical steps provides the global load-

displacement response (Invernizzi et al., 2011). The global procedure is as follows, in which the following steps are subsequently carried out:

- Add the external load as a unit load.
- Perform a linear-elastic analysis
- Extract the critical element from the results. The critical element is the element for which the principal tensile stress level divided by its current strength is the highest in the whole structure.
- Calculate the ‘global load factor’ as the ratio between the current strength and the stress level in the critical element. The present solution step is obtained by scaling the unit load times the global load factor.
- Increase the damage in the critical element by reducing its stiffness and strength according to a saw-tooth tensile softening stress strain curve. Different approaches for a saw-tooth approximation of the constitutive law can be found in (Rots et al., 2008).
- Repeat the previous steps for the new configuration, i.e. re-run the linear analysis for structure in which the stiffness and strength of previous critical element are reduced. Repeat this process until the damage is spread into the structure.
- Construct the overall stress-displacement curve by connecting all load-displacement sets consecutively found in the above steps.

The SLA method was later improved by Rots and Invernizzi (2004) and Rots et al. (2008) to achieve objectivity with respect to mesh grading. However, the major drawbacks of the above mentioned approach is the inability to properly capture non-proportional loading. An extension of the SLA concept towards the non-proportional loading was proposed in (DeJong et al., 2008; Eliáš et al., 2010; Graça-e-Costa et al., 2013). This approach has been applied successfully to masonry structures, reinforced concrete beams and nonlinear behaviour in mortar and engineering cementations composites in flexure as well as concrete beams with shear failure (Graça-e-Costa et al., 2012; Slobbe et al., 2012; Hendriks and Rots, 2013; Vorel and Boshoff, 2015).

However, it can be claimed that the main disadvantages of the SLA method are its problematic application to non-proportional loading and non-smoothness of the obtained load-displacement response (Eliáš, 2015; Slobbe, 2015). In addition, it

should be kept in mind that the advantages of the SLA approach are sometimes diminished by its relatively high computational cost (Vorel and Boshoff, 2015).

Another approach which avoids using multiple iterations is the implicit-explicit “IMPL-EX” approach of Oliver et al (2006a; 2008a). The proposed implicit-explicit integration scheme is based on two stages per time step. The first stage consists of an explicit extrapolation of local variables (e.g. a damage evolution parameter) and the associated stresses according to the implicit quantities calculated at the previous time step. The extrapolated local quantities are used for the assembly of the total tangent matrix and the determination of the vector of internal forces. The balance equation, which is function of extrapolated values, is solved and thus the nodal displacements are obtained. These nodal displacements are not subsequently modified in the current time step. Following the first stage, the standard implicit integration of the constitutive model is performed at the same time step, based on the known nodal displacements from the first stage, thus the implicitly integrated stresses and local variables are obtained. It should be borne in mind that the accuracy of the solution of the IMPL-EX strategy depends on the length of the time step (Oliver et al., 2006b).

More recently, Prazeres et al. (2015) proposed the so-called ‘modified implicit-explicit approach’ for elasto-plastic models. In the modified method, the internal variables (i.e. plastic multiplier, total plastic strains and total stresses) are updated in terms of the explicit evaluation of the plastic strain tensor components instead of the explicit evaluation of the plastic multiplier. The main advantage of the modified IMPL-EX approach for elastoplasticity problems, in comparison to the standard IMPL-EX method, is that the tangent stiffness matrix becomes constant. However, the main drawbacks of the standard IMPL-EX approach is also inherited by the modified IMPL-EX method, in which the accuracy depends to a large extent on the step size.

## **2.5 Elements with embedded SD approach**

To the best knowledge of the author, the first attempt to incorporate discontinuities directly into individual finite elements was made by Ortiz et al. (1987). They enriched the approximation of the strain field to improve the resolution of shear bands. This method became known later as the weak discontinuity approach. The approach was further developed by Belytschko et al. (1988), who developed a formulation which could capture a band of localization strain bounded by two parallel weak discontinuity lines within an single element. Significant progress in the development of finite elements with embedded strong discontinuities was achieved by Simo et al. (1993) In this seminal paper, Simo et al. (1993) describe a method for approximating the failure kinematics of solids by means of discontinuous displacement fields locally embedded within elements. Their method allows incompatible displacement fields, that include displacements jumps, to be simulated. They applied the enhanced assumed strain concept, in which only the enhanced strains resulting from the discontinuous displacement field appear explicitly in the formulation. The variational basis of the enhanced strain and displacements fields was established by Simo and co-workers (Simo and Rifai, 1990; Simo and Armero, 1992; Simo and Oliver, 1994). The embedded SD approach of Simo et al. (1993) was further elaborated by many authors in the last decade of the last century, see for example (Lotfi and Shing, 1995; Armero and Garikipati, 1996; Oliver, 1996a; Oliver, 1996b; Oliver et al., 1999; Rugeiro and Borja, 1999). A thorough review of all of these methods was provided by (Jirásek, 2000).

Due to the huge number of papers that have been published on the SD approach; the author will focus the remainder of this review on what he considers to be the most important recent developments.

### **2.5.1 Work of the Delft research group**

Wells and Sluys (2001a) and (Wells et al., 2002) developed a formulation for incorporating discontinuous displacements within finite elements based on the partition of unity concept (Melenk and Babuška, 1996). Unlike methods based on

enhanced assumed strain fields, their approach places no restrictions on allowable element types and allows displacement jumps to be continuous across element boundaries. The displacement jump across a crack was represented by extra degrees of freedom located at existing nodes. Considerable complexities are involved in the 3D implementation, when the SD formulation is based on the partition of unity concept.

In addition, Wells and Sluys (2001b) extended the SD approach developed by Simo et al. (1993) to a three-dimensional embedded discontinuity model for simulating brittle materials. They included the effect of a discontinuity in the displacement field as an incompatible strain mode. In this method, the additional degrees of freedom associated with the discontinuous displacement mode are eliminated at the element level by static condensation, therefore the system of global degrees of freedom remain unchanged. Also, (Alfaiate et al., 2002) used the same principal for modelling mixed-mode fracture in quasi-brittle materials with triangular elements.

Furthermore, Alfaiate et al. (2003) proposed a formulation for embedding interface elements into any parent element to capture linear jumps along a discontinuity. This formulation was developed within the framework of the discrete crack approach. The displacement jumps were approximated by global additional degrees of freedom which were evaluated at the discontinuity surface and introduced as a crack propagates.

Moreover, In Dias-da-Costa et al. (2009a), a global formulation was introduced using a linear variation of the displacement jump along the discontinuity. This approach was named the discrete strong discontinuity approach (DSDA). In the DSDA, a rigid body motion, induced by the opening of the discontinuity, was transmitted to the parent element nodes. As a consequence, shear jumps are constrained such that they must remain constant along the discontinuity. This can be considered as a limitation from the kinematical point of view. A variationally consistent formulation with traction continuity, called generalized strong discontinuity approach (GSDA), was introduced by Dias-da-Costa et al. (2009b). The GSDA considers both rigid body motions and the relative expansion (or contraction) of the sub-domains either side of a discontinuity. More recently, the DSDA and GSDA were improved by Dias-da-Costa et al. (2013), in such a way that

a new embedded formulation built upon the framework of the discrete crack approach were proposed to deal with strong discontinuities using conforming finite elements.

### **2.5.2 Work of the research group at UPC**

The most well-known work by Oliver and co-workers, i.e. Oliver (2000), Oliver et al. (2002), Oliver et al. (2003a), Oliver et al. (2003b), Oliver and Huespe (2004) and Oliver et al. (2008b) is the development of the so-called continuum strong discontinuity approach (CSDA) to model material failure. The CSDA provides a link between continuum stress-strain models and cohesive fracture models, such that a strong discontinuity (displacement jump) is obtained as the limit of a weak discontinuity band when the crack bandwidth tends to zero (Oliver et al., 2012). In other words, in the CSDA, instead of using an explicit fictitious crack model for modelling the constitutive behaviour at the embedded discontinuity interface, a continuum constitutive model (stress-strain relationship) is used. The strong discontinuity kinematics projects the continuum stress-strain model onto the interface as a traction-separation law.

In the CSDA formulation the same continuum constitutive model can be used for modelling the bulk stress-strain relationship during the elastic or the unloading stages, and the traction-separation law at the fracture path in the inelastic-strain softening stages of the material (Oliver et al., 2012). It should be also mentioned that the CSDA requires the use of tracking algorithms that ensure continuity of the crack path when passing from one element to another (Oliver and Huespe, 2004; Oliver et al., 2004; Mosler and Meschke, 2004). However, Gálvez et al. (2013) argued that whilst the CSDA is an elegant solution for simulating shear bands in soils and metals, but that it is simpler and more effective to use a discrete constitutive model that relates the tractions and displacements jumps at the discontinuity interface when modelling fracture in quasi-brittle materials.

### 2.5.3 Work of other research groups

Mosler and Meschke (2003) presented a new algorithmic formulation for 3D quadrilateral elements with embedded discontinuities for plane problems using an elastoplastic model. The numerical formulations suggested were not based on the static condensation technique; rather, the parameters defining the displacement jump within the finite element are condensed out at the material point level. Thus, they claimed that the resulting constitutive equations are formally identical to those of standard continuum models (Mosler, 2005; Mosler, 2006). A similar approach was presented by (Borja, 2000), but his approach was restricted to constant strain triangle elements.

In 2007, Linder and Armero presented new finite elements that incorporate strong discontinuities with linear interpolations of the displacement jumps for modelling failure in 2D solids. They used the concept of the strain-based approach. Linder and Armero (2007) focused on the improvement of higher-order plane continuum finite elements such as quadrilateral elements within the small-strain regime. Later on, they extended their method to model also cracking branching (Linder and Armero, 2009) and dynamic failure (Armero and Linder, 2009). A thorough description of the contributions of Armero and co-workers to this field is available in the theses of Armero's former PhD students Linder (2007) and Kim (2013).

Ibrahimbegovic and co-workers ( Dujc et al. (2010) and Dujc et al. (2013) ) presented a formulation to incorporate strong discontinuities within quadrilateral finite elements to model the failure in plane stress solids. The key feature of the derived embedded element with strong discontinuity is that it linearly interpolates the displacement jumps in both normal and tangential directions with respect to the discontinuity line. In fact, they proposed four kinematic parameters to model four modes of element separations along the discontinuity interface. Those kinematic parameters are condensed out on the element level to provide a standard form of element stiffness matrix.

Embedding discontinuous displacements in the element formulation is not the only way to implement the SD approach in the finite element method. The major alternative is the so-called extended finite element method (X-FEM), which is based

on nodal enrichments and allows displacement discontinuities to be introduced into finite element meshes independently of its boundaries (Belytschko and Black, 1999; Moës et al., 1999; Belytschko et al., 2001; Belytschko et al., 2009). Indeed, this ability makes this method very appealing for capturing arbitrary crack propagation with fixed finite element meshes without loss of mesh objectivity (Oliver et al., 2008b). It should be emphasised here again that the XEFM approach is beyond the scope of this thesis. A comparison between the EFEM (elements with embedded strong discontinuities) and the XFEM approach can be found in Jirásek and Belytschko (2002), Oliver et al. (2006b), Borja (2008) and (Dias-da-Costa et al., 2010). According to these references, the nodal enrichment technique (XFEM) is computationally more expensive and requires a greater implementation effort compared with elements with embedded discontinuities.

# Chapter 3

## An incremental-iterative method for numerical simulation of quasi-brittle materials

---

### 3.1 Introduction

The progressive failure of quasi-brittle materials such as concrete under various loading conditions is mainly due to the development, growth and coalescence of micro-cracks, which induce degradation in both the strength and stiffness of the material. The degradation is reflected macroscopically as strain softening behaviour (Bažant, 1992; Karihaloo, 1995; van Mier, 2012) and it is well-known that this behaviour gives rise to numerical difficulties (De Borst et al., 2012). Therefore it is necessary to use a robust solution algorithm when implementing a numerical model for QB materials.

Incremental-iterative procedures are generally considered to be the most effective algorithms for the finite element analysis of nonlinear problems (Crisfield, 1991; Crisfield, 1997). However, it is known from previous work (see Section 2.4) that existing Newton-based incremental-iterative schemes often suffer from stability and convergence difficulties and thus can be inappropriate for the numerical simulation of many quasi-brittle materials problems. As a consequence, many methods that avoid using iterations, or minimise their use, have been proposed, as mentioned in Section 2.4.

A novel incremental-iterative numerical approach for the nonlinear finite element analysis of quasi-brittle materials has been developed by the author. The new method, named smooth unloading-reloading (SUR) approach, improves the robustness and convergence properties of a finite element isotropic damage model when applied to fracture problems in quasi-brittle materials. The SUR approach uses a target function and a smooth unloading-reloading function to compute an

approximate tangent matrix with an incremental-iterative Newton type solution procedure.

A number of idealised quasi-brittle fracture examples are used to evaluate the performance of the proposed SUR approach. These examples were mainly chosen for their numerical characteristics and, with one exception, were not based upon real experiments or structures. In all cases, the ‘reference solution’ was obtained using a model with secant unloading-reloading behaviour.

## **3.2 Constitutive model**

An isotropic damage model with a single damage variable, driven by the equivalent stress parameter, is used in this study. The reason that a relatively simple isotropic damage model has been chosen for the present work is because the purpose of this study is not to evaluate the accuracy of isotropic damage models and their ability to simulate the behaviour of fracture problems in a finite element context, which have been established elsewhere (Oliver et al., 1990; Comi and Perego, 2001; Oliver et al., 2002; Oliver et al., 2006a; Oliver et al., 2008b; Manzoli et al., 2008), but rather to illustrate the convergence characteristics of the proposed SUR method and to demonstrate its potential benefits.

Before describing the new smooth unloading-reloading (SUR) algorithm, the basic form of the damage model employed for the work will be described.

### **3.2.1 Isotropic damage model**

The SUR algorithm developed is employed with the isotropic damage model of Oliver et al (1990; 2002; 2006a). This isotropic damage model is based on the simplifying assumption that stiffness degradation is isotropic and the loss of material stiffness is characterised by a scalar damage variable ( $\omega \in [0, 1]$ ), in which  $\omega = 0$  for undamaged materials and  $\omega = 1$  for fully damaged materials. The constitutive equation for the isotropic damage model is expressed as:

$$\boldsymbol{\sigma} = (1 - \omega) \mathbf{D}_0 : \boldsymbol{\varepsilon} \quad (3.1)$$

where  $\boldsymbol{\sigma}$  and  $\boldsymbol{\varepsilon}$  are the stress and strain tensors respectively;  $\mathbf{D}_0$  donates the elastic stiffness tensor of the undamaged material and the damage variable  $\omega$  is a function of a damage evolution parameter  $r_p$ .

The standard form of constitutive equations for the isotropic damage model are summarised in the following Table 3.1.

Table 3.1: Summary of isotropic damage model algorithm Oliver et al (1990; 2002; 2006a).	
$\boldsymbol{\sigma} = (1 - \omega) \mathbf{D}_0 : \boldsymbol{\varepsilon}$	Constitutive equation
$r_p = r_{eff} \quad r_p /_{t=0} = r_k \quad r_p \geq r_k$ $r_{eff} = \sqrt{\boldsymbol{\sigma}_0^+ : \mathbf{D}_0^{-1} : \boldsymbol{\sigma}_0^+}$	Damage evolution parameter
$f(r_{eff}, r_p) = r_{eff} - r_p$	Damage function
$\dot{r}_p \geq 0; \quad f \leq 0; \quad \dot{r}_p f = 0;$	Damage loading/unloading Conditions
$\mathbf{D}_{tan} = \begin{cases} (1 - \omega) \mathbf{D}_0 & \forall r_{eff} < r_p \\ (1 - \omega) \mathbf{D}_0 - \frac{d\omega}{dr_p} \boldsymbol{\sigma}_0 : \left( \mathbf{D}_0 \otimes \frac{dr_p}{d\boldsymbol{\sigma}} \right)^T & \forall r_{eff} \geq r_p \end{cases}$	Constitutive tangent operator

The effective stress is defined as follows:

$$\boldsymbol{\sigma}_0 = \mathbf{D}_0 : \boldsymbol{\varepsilon} \quad (3.2)$$

$r_{eff}$  is a scalar measure of the current ‘effective’ stress and is computed by:

$$r_{eff} = \sqrt{\boldsymbol{\sigma}_0^+ : \mathbf{D}_0^{-1} : \boldsymbol{\sigma}_0^+} \quad (3.3)$$

where  $\boldsymbol{\sigma}_0^+$  denotes the positive part of the effective stress tensor, and is given by the following form:

$$\boldsymbol{\sigma}_0^+ = \sum_{i=1}^3 \langle \boldsymbol{\sigma}_{0i} \rangle \mathbf{p}_i \otimes \mathbf{p}_i \quad (3.4)$$

where  $\langle \boldsymbol{\sigma}_{0i} \rangle$  stands for the positive part of the  $i$ th principal effective stress  $\boldsymbol{\sigma}_{0i}$ ,  $\mathbf{p}_i$  represents the  $i^{\text{th}}$  stress eigenvector. Symbol  $\otimes$  denotes the tensor product, and symbol  $\langle x \rangle$  is the Macaulay bracket, in which  $\langle x \rangle = x$ , if  $x \geq 0$ ;  $\langle x \rangle = 0$ , if  $x < 0$ . The effective stress norm is only computed from the positive part of the effective stress, as can be seen in equation 3.3. For this reason, the damage in this model is only associated with tensile stress states, which is mainly appropriate for modelling tensile failure in quasi-brittle materials.

The damage loading function is expressed in terms of the effective stress and the scalar damage evolution parameter ( $r_p$ ). The damage loading function is given by:

$$f(r_{eff}, r_p) = r_{eff} - r_p \quad (3.5)$$

Physically,  $r_p$  is a scalar measure of the largest effective stress ever reached in the history of the material up to the current state. Initially, the damage evolution parameter value  $r_p$  is equal to  $r_k$ , which is the damage evolution parameter at the peak of the uniaxial stress curve and is related to the peak stress  $f_t$  of the material in uniaxial tension. The method used to compute  $r_k$  is explained in Section 3.2.

When the damage loading function  $f(r_{eff}, r_p)$  equals 0, the stress state lies on the damage surface.  $f(r_{eff}, r_p) < 0$  means there is no growth of the damage, the material behaves elastically and stress remains within the damage surface. The damage evolution parameter can only increase when the effective damage evolution

parameter  $r_{eff}$  exceeds the current value of the damage evolution scalar  $r_p$ , in the case of  $f(r_{eff}, r_p) > 0$ . Theoretically, the damage is initiated when the  $r_{eff}$  exceeds for the first time the value of  $r_p$ .

Quasi-brittle materials can be modelled by assuming that the stress state always remains on or within the loading surface  $f(r_{eff}, r_p) \leq 0$ , which means that the damage evolution parameter  $r_p$  must satisfy the Kuhn-Tucker condition:

$$\dot{r}_p \geq 0; \quad f \leq 0; \quad \dot{r}_p f = 0; \quad (3.6)$$

The first condition illustrates that  $r_p$  cannot decrease. The second condition means that  $r_p$  can never be smaller than  $r_{eff}$ . Finally, the third condition indicates that  $r_p$  can only grow if the current values of  $r_{eff}$  and  $r_p$  are equal (Peerlings et al., 2000).

The derivation of the constitutive tangent tensor is given in Appendix B, and takes the form:

$$\mathbf{D}_{tan} = \begin{cases} (1 - \omega) \mathbf{D}_0 & \forall r_{eff} < r_p \\ (1 - \omega) \mathbf{D}_0 - \frac{d\omega}{dr_p} \boldsymbol{\sigma}_0 : \left( \mathbf{D}_0 \otimes \frac{dr_p}{d\boldsymbol{\sigma}} \right)^T & \forall r_{eff} \geq r_p \end{cases} \quad (3.7)$$

The tangent constitutive operator  $\mathbf{D}_{tan}$  changes for unloading ( $\forall r_{eff} < r_p$ ) and reloading ( $\forall r_{eff} \geq r_p$ ) processes.

In the standard form of the model, the damage parameter ( $\omega$ ) depends directly upon a softening function  $f_{ss}(r_p)$  according to the following relationship;

$$\omega(r_p) = 1 - \frac{f_{ss}(r_p)}{r_p} \quad (3.8)$$

A standard exponential form for this softening function is as follows:

$$f_{ss}(r_p) = \begin{cases} f_t & \forall r_{eff} \leq r_t \\ f_t e^{-c_I \frac{(r_{eff} - r_t)}{(r_0 - r_t)}} & \forall r_{eff} > r_t \end{cases} \quad (3.9)$$

in which  $f_t$  is the tensile strength,  $E$  is Young's modulus,  $\varepsilon_t$  defines the tensile strain measure,  $r_t = \varepsilon_t \cdot \sqrt{E}$  is the damage strength parameters effective strength,  $c_I=5$ ,  $\varepsilon_t = f_t/E$ ,  $r_0 = \varepsilon_0 \cdot \sqrt{E}$  and  $\varepsilon_0$  is the strain at the effective end of the softening curve. In other words, the strain at which the transmitted stress becomes negligible is denoted by  $\varepsilon_0$ .

It should be noted that the above form of  $f_{ss}$  is introduced only to provide a complete description of the standard model. This softening function is not used in the new model but is replaced by the target function  $f_s$  given in Section 3.2 of this chapter.

### 3.2 Smooth unloading-reloading and target damage functions

The proposed SUR approach uses a target function  $f_s(r_p)$  and a smooth unloading-reloading function  $\sigma_p(r_p, r_{eff})$ , as illustrated in Figure 3.1. It may be seen that the SUR function has two parts; **(i)** when  $r_{eff} < a_p r_p$ , for which linear unloading-reloading with a slope  $(1 - \omega_{pf})E$  is assumed, and **(ii)** when  $r_{eff} \geq a_p r_p$ , for which nonlinear unloading-reloading is assumed, according to the function  $\sigma_p(r_p, r_{eff})$ . Where  $\omega_{pf}$  is the damage parameter that controls the linear part of the SUR function, and  $\sigma_k(r_p)$  is stress to which the SUR function is asymptotic, as can be seen in Figure 3.1.

The SUR function depends on the damage evolution parameter ( $r_p$ ), which is updated for every iteration within each load/displacement increment from the value obtained at the last converged increment.

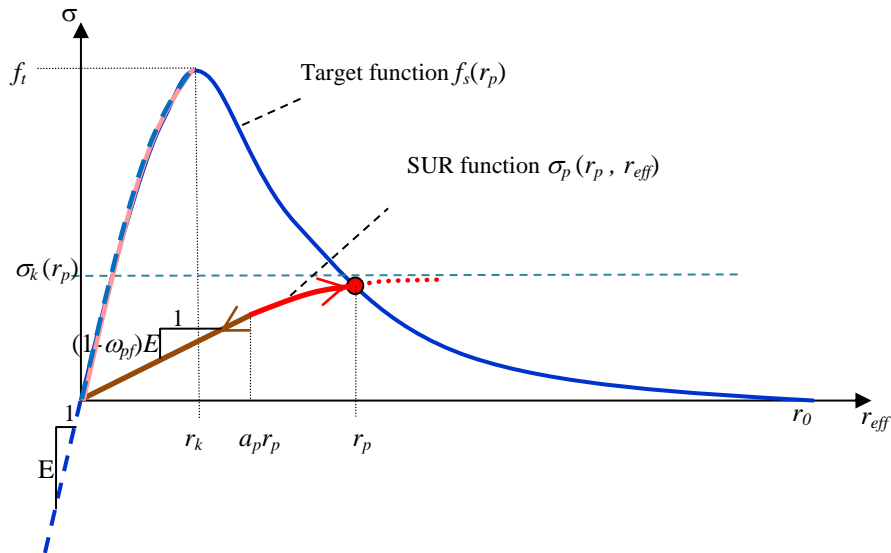


Figure 3.1: Unloading-reloading and target damage evolution function.

It should be noted that the unloading-reloading response shown in Figure 3.1 more accurately represents the response measured in tests than does a function based on secant unloading-reloading (Reinhardt, 1984). The true unloading-reloading response exhibits hysteresis behaviour that is not simulated here. Rather, the model employs a function that closely represents the real reloading curve. This is a simplification, but these hysteresis effects are considered to be of secondary importance in the simulation of most plain and reinforced concrete structures.

The target function gives the equivalent uniaxial stress and depends on the damage evolution parameter  $r_p$ , which in 1D, is directly proportional to the maximum strain experienced. The complete uniaxial curve, upon which the target curve is based, is given in equation (3.10).

$$f_s(r_p) = \begin{cases} f_t & \forall r_p < r_k \\ f_t \cdot e^{-\epsilon_0 \left( \frac{r_p - r_k}{r_0 - r_k} \right)} & \forall r_p \geq r_k \end{cases} \quad (3.10)$$

where,  $r_k = r_t \cdot a_k$  and  $\epsilon_0$  is the strain at the effective end of the of the target softening curve. The parameter  $a_k$  is given after equation (3.12). It is noted that this function is the same as that given in equation (3.9) with the exception that  $r_k$  replaces  $r_t$  and  $r_p$  replaces  $r_{eff}$ .

Whilst the pre-peak and post-peak parts of the target function are given in equation (3.10) for completeness, the proposed algorithm only employs  $f_s$  from the peak onwards, as explained later in this section.

The SUR function is tangential to the secant curve with modulus  $[(1 - \omega_{pf}) E]$ , and is asymptotic to the stress  $\sigma_k(r_p)$  in equation (3.12) and takes the form as:

$$\sigma_p(r_p, r_{eff}) = \sigma_k(r_p) \cdot \left[ 1 - \left( 1 - \frac{a_p}{\nu} \right) \cdot e^{-\left[ \frac{r_{eff} - a_p r_p}{(\nu - a_p) r_p} \right]} \right] \quad (3.11)$$

in which the constants  $\nu$  and  $a_p$  take default values of 0.70 and 0.75 respectively, although the effect on the numerical performance of the model of varying these parameters is explored in example 3.6.5. These default values provide a reasonable representation of the reloading response measured in cyclic uniaxial fracture tests (Reinhardt, 1984) and the values can be directly calibrated using data from such tests. However, it is emphasised that the aim of the present work is directed towards improving the stability and robustness of solutions to fracture problems and not towards improving the accuracy of existing damage models. The value of the damage evolution parameter at the peak of the uniaxial stress curve is denoted  $r_k$ . The initial value of  $r_p$  is set to  $r_k$  (i.e. the value at the peak of the target softening function).

$\sigma_p$  depends upon the asymptotic stress function  $\sigma_k$ , which is defined as follows;

$$\sigma_k(r_p) = \begin{cases} f_s(r_k) \cdot v \cdot a_k & \forall r_p \leq r_k \\ f_s(r_p) \cdot v \cdot a_k & \forall r_p > r_k \end{cases} \quad (3.12)$$

noting that  $f_s(r_k) = f_t$ .

The above expressions for  $\sigma_k$  are obtained by equating  $\sigma_p$  from equation (3.11) to  $f_s$  from equation (3.10), for a given value of  $r_p$  i.e. the curve coincides at  $r_{eff} = r_p$ .

Using equation (3.12) in (3.11) and again considering the condition  $f_s(r_p) = \sigma_p$  at  $r_{eff} = r_p$ , leads to the following expression for  $a_k$ :

$$a_k = \frac{1}{v \cdot \left[ 1 - \left( 1 - \frac{a_p}{v} \right) \cdot e^{\left[ \frac{1-a_p}{v-a_p} \right]} \right]}$$

The damage parameter that controls the linear part of the SUR function is computed as:

$$\omega_{pf}(r_p) = \begin{cases} 0 & \forall r_p \leq r_k \\ 1 - \frac{\sigma_k}{v \cdot r_p \cdot \sqrt{E}} & \forall r_p > r_k \end{cases} \quad (3.13)$$

and the damage parameter for the SUR function is given by:

$$\omega_p(r_p, r_{eff}) = \begin{cases} \omega_{pf} & \forall r_{eff} \leq a_p r_p \\ 1 - \frac{\sigma_p(r_p, r_{eff})}{\sqrt{E} \cdot r_{eff}} & \forall r_{eff} > a_p r_p \end{cases} \quad (3.14)$$

In the above equations, it may be seen that the target function is used solely as a dependent function in  $\sigma_p$  via equation (3.12), and, since the value of the function  $\sigma_p$  is fixed until  $r_p$  exceeds  $r_k$ , only the post-peak part of the  $f_s$  function is actually used in the model.

Overall, the introduction of the SUR function results in changes to two of the model equations presented in Table 3.1; these being the overall constitutive equation (3.15) and the expression for the tangent  $\mathbf{D}$  matrix (equation 3.16), as follows:

$$\boldsymbol{\sigma} = (1 - \omega_p(r_p, r_{eff})) \mathbf{D}_0 : \boldsymbol{\varepsilon} \quad (3.15)$$

$$\mathbf{D}_{tan} = \begin{cases} (1 - \omega_{pf}) \mathbf{D}_0 & \forall r_{eff} < a_p r_p \\ (1 - \omega_p) \mathbf{D}_0 - \frac{d\omega_p}{dr_p} \boldsymbol{\sigma}_0 : \left( \mathbf{D}_0 \otimes \frac{dr_p}{d\boldsymbol{\sigma}} \right)^T & \forall r_{eff} \geq a_p r_p \end{cases} \quad (3.16)$$

The overall stress-strain relationship (3.15) now depends on  $\omega_p$ , rather than  $\omega$ , which in turn is governed by the value of SUR function  $\sigma_p$ .

The new form of the matrix  $\mathbf{D}_{tan}$  is evaluated using the SUR function and therefore is always positive definite. However, this means that  $\mathbf{D}_{tan}$  is not the exact tangent when there is loading with respect to the damage function. The implications of this are illustrated in the examples given in Section 3.6.

### 3.3 Fracture energy for simplified softening curve

The precise definition of the fracture energy has been a subject of debate, because it has been found to vary with the size and shape of the test specimen (Karihaloo et al., 2003; Jirásek et al., 2004). However, Jirásek et al. (2004) defined the fracture energy as the total work needed to completely break a specimen per unit ligament area, in

which the area under the stress-strain curve represents the total work of fracture. Using this definition gives the following standard expression for the fracture energy:

$$G_f = \int_0^{\infty} \sigma du = \ell_{ch} \int_0^{\infty} \sigma d\varepsilon \quad (3.17)$$

In which  $\sigma$  and  $\varepsilon$  are the uniaxial stress and average uniaxial strain in a fracture process zone, and  $\ell_{ch}$  is the characteristic length.

The integral in equation (3.17) is equal to the area under the governing uniaxial stress-strain curve, as illustrated in Figure 3.2, which mathematically is given by:

$$\int_0^{\infty} \sigma d\varepsilon = \left( \frac{1}{2} E (a_p \varepsilon_k)^2 + \int_{a_p \varepsilon_k}^{\varepsilon_k} \sigma_k \left( 1 - \left( 1 - \frac{a_p}{\nu} \right) e^{\frac{-(\varepsilon - a_p \varepsilon_k)}{(\nu - a_p) \varepsilon_k}} \right) d\varepsilon + \int_{\varepsilon_k}^{\infty} f_t \cdot e^{-c_f \left( \frac{\varepsilon - \varepsilon_k}{\varepsilon_0 - \varepsilon_k} \right)} d\varepsilon \right) \quad (3.18)$$

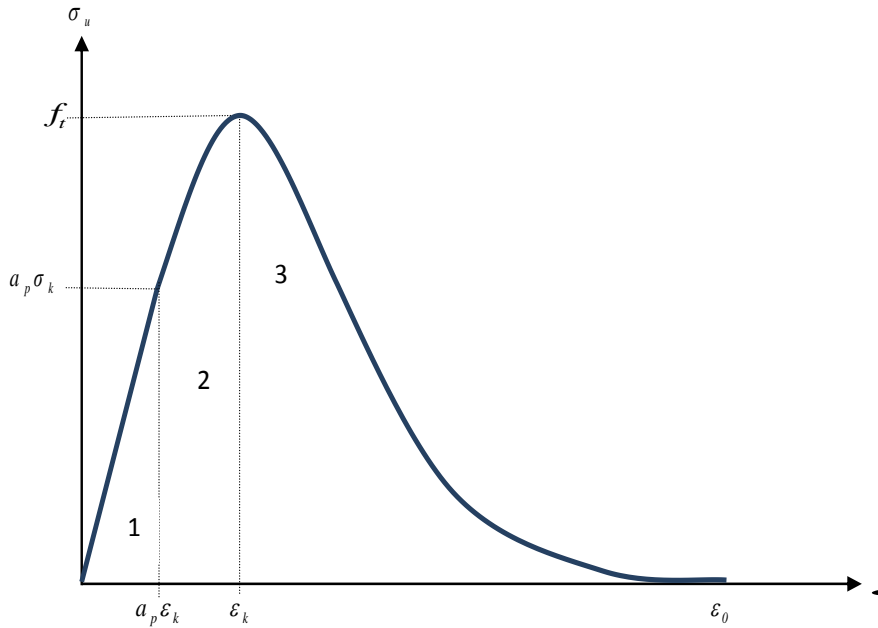


Figure 3.2: Stress-strain curve of quasi-brittle materials.

where  $\sigma_k = E \cdot \varepsilon_k$ . The fracture energy is then given by:

$$G_f = \ell_{ch} \left( \frac{1}{2} E (a_p \varepsilon_k)^2 + \int_{a_p \varepsilon_k}^{\varepsilon_k} \sigma_k \left( 1 - \left( 1 - \frac{a_p}{v} \right) e^{\frac{-(\varepsilon - a_p \varepsilon_k)}{(v - a_p) \varepsilon_k}} \right) d\varepsilon + \int_{\varepsilon_k}^{\infty} f_t \cdot e^{-c_I \left( \frac{\varepsilon - \varepsilon_k}{\varepsilon_0 - \varepsilon_k} \right)} d\varepsilon \right) \quad (3.19)$$

from which the following is obtained;

$$G_f = \ell_{ch} \left( \frac{a_p^2}{2} \varepsilon_k \sigma_k + \varepsilon_k \sigma_k \left( (1 - a_p) - (a_p - v) \left( e^{\frac{1 - a_p}{(v - a_p) \varepsilon_k}} - 1 \right) \left( 1 - \frac{a_p}{v} \right) \right) + \frac{f_t (\varepsilon_0 - \varepsilon_k)}{c_I} \right) \quad (3.20)$$

Equation (3.20) can be simplified to:

$$G_f = \ell_{ch} \left[ f_t \varepsilon_{ad} + \frac{f_t \varepsilon_0}{c_I} \right] \quad (3.21)$$

hence

$$\varepsilon_0 = \left( \frac{G_f}{\ell_{ch} f_t} - \varepsilon_{ad} \right) \cdot c_I \quad (3.22)$$

in which  $\varepsilon_{ad} = a_d \varepsilon_t$ .

$$a_d = a_k^2 \left( \frac{a_p^2}{2} + \left( (1 - a_p) - (a_p - v) \left( e^{\frac{1 - a_p}{(v - a_p) \varepsilon_k}} - 1 \right) \left( 1 - \frac{a_p}{v} \right) \right) \right) - \frac{a_k}{c_I} \quad (3.23)$$

The primary input parameters governing cracking behaviour are  $G_f$  and  $f_t$ . In addition, the characteristic length (see next section) is obtained from the element geometry and the parameters  $v$  and  $a_p$  are fixed at chosen values, as explained in Section 3.2.

### 3.4 Element characteristic length calculation

It has been shown that the method used to calculate the element characteristic length in the crack-band model (Bažant and Oh, 1983) can have a significant influence on computed responses (Oliver, 1989; Jirásek and Grassl, 2008; Jirásek and Bauer, 2012; Volokh, 2013; Slobbe, 2015; Mosalam and Paulino, 1997). It is essential for the characteristic length ( $\ell_{ch}$ ) to vary with element orientation, for all but circular elements, and for this length to equal the full width of the fracture process zone that crosses an element. The author has devised a convenient method for computing  $\ell_{ch}$  that employs the element Jacobian matrix. This results in the maximum length, measured in convected coordinates, of a line perpendicular to a crack-band. In this work, the orientation of a crack-band is determined from the major principal strain axis.

The proposed method for computing the characteristic length is as follows:

- i. Consider a unit normal vector to a crack  $\mathbf{r}$ , which is related to the equivalent vector in the element local coordinate  $\boldsymbol{\chi}_r$  by the Jacobian matrix ( $\mathbf{J}$ ), as follows:

$$\begin{bmatrix} \frac{\partial x}{\partial \xi} & \frac{\partial x}{\partial \eta} & \frac{\partial x}{\partial \zeta} \\ \frac{\partial y}{\partial \xi} & \frac{\partial y}{\partial \eta} & \frac{\partial y}{\partial \zeta} \\ \frac{\partial z}{\partial \xi} & \frac{\partial z}{\partial \eta} & \frac{\partial z}{\partial \zeta} \end{bmatrix} \begin{bmatrix} \Delta \xi \\ \Delta \eta \\ \Delta \zeta \end{bmatrix} = \begin{bmatrix} r_x \\ r_y \\ r_z \end{bmatrix} \quad \text{Or} \quad \mathbf{J}^T \boldsymbol{\chi}_r = \mathbf{r} \quad (3.24)$$

in which  $\xi$ ,  $\eta$  and  $\zeta$  are the local parametric coordinates of an element.

In order to work out the vector length in the local direction  $\boldsymbol{\chi}_r$  in an element, firstly a unit vector in the direction of  $\boldsymbol{\chi}_r$  is created, which is denoted  $\hat{\boldsymbol{\chi}}$ . For quadrilateral and hexahedral elements, the local coordinates range from (-1 to +1) and the largest absolute component of  $\hat{\boldsymbol{\chi}}$  is scaled to 1 to give vector  $\boldsymbol{\chi}$ , see Figure 3.3. For

triangular and tetrahedral elements, the local coordinates range between 0 and +1. Two cases in triangular and tetrahedral elements should be considered:

- **Case 1:** If all local vector components have the same sign, the local vector has to be scaled to the boundary ( $\xi + \eta + \zeta = 1$ ).
- **Case 2:** If the local vector points into the element from a corner such that the vector components have different signs, then the local vector is scaled to the appropriate local axis boundary, i.e. the largest absolute component of  $\hat{\chi}$  is scaled to 1 to give vector  $\chi$ .

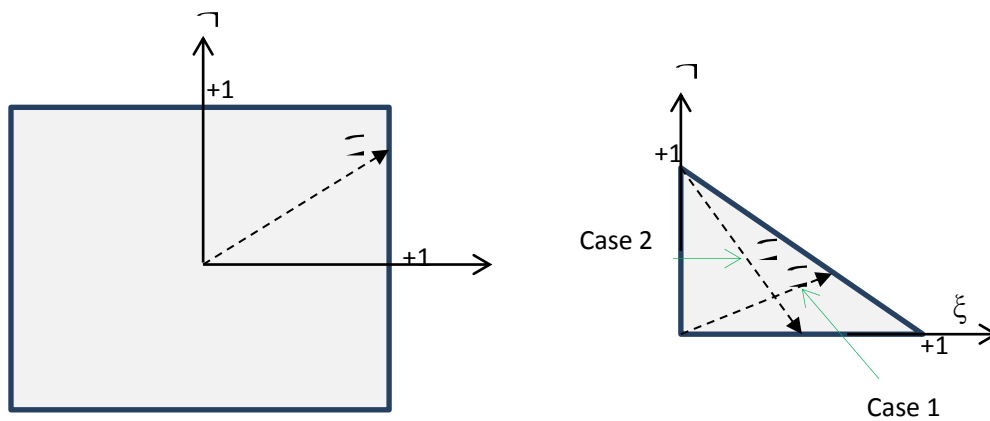


Figure 3.3: Quadrilateral and triangular elements.

The vector  $\chi$  is computed as follows:

$$\chi_r = \mathbf{J}^{-1} \mathbf{r} \quad (3.25)$$

$$\hat{\chi} = \frac{1}{|\chi_r|} \chi_r \quad (3.26)$$

$$\chi = \frac{\hat{\chi}}{\max(|\hat{\chi}|)} \quad (3.27)$$

ii. The Cartesian vector  $\mathbf{r}_{xyz}$  corresponding to the vector  $\boldsymbol{\chi}$  can be computed as:

$$\mathbf{r}_{xyz} = \mathbf{J}^T \boldsymbol{\chi} \quad (3.28)$$

iii. The characteristic length  $\ell_{ch}$  is then given by the magnitude of  $\mathbf{r}_{xyz}$ , scaled by the range of the local coordinates:

$$\ell_{ch} = r_g * |\mathbf{r}_{xyz}| \quad (3.29)$$

in which the local coordinate range ( $r_g$ ) for quadrilateral and hexahedral elements is 2, and equals to 1 for triangular elements.

This method for computing  $\ell_{ch}$  was implemented in the finite element code developed for the present work and used for all of the examples presented in this thesis.

### 3.5 Convergence criteria

The termination of the iterations in nonlinear algorithms is determined by convergence criteria. Customarily, three types of convergence criteria are used to measure how well the obtained solution satisfies equilibrium (Belytschko et al., 2013):

- A criterion based on force
- A criterion based on displacement
- An energy error criterion

L2 iterative displacement and out of balance force norms are used in this thesis. The L2-norm is known as a Euclidean norm, and can be defined as the square-root of the sum of the squared values of the vector elements. Sometimes, the norm of iterative displacement change can be very small while the residual force norm is very large.

Hence, it is recommended to adopt both displacement-based and out-of-balance-force norm criteria (Crisfield, 1991).

Convergence is achieved when the L2-norm reaches a certain convergence tolerance. Indeed, the convergence tolerance determines, in one sense, the accuracy of a calculation and also can affect the solution time. If the tolerance is too coarse, the solution may be quite inaccurate. On the other hand, using an excessively tight convergence tolerance can result in time consuming and unnecessary computations (Becker, 2004; Bathe, 2006).

The force criterion is given by;

$$\frac{\|\Delta \underline{F}_{\text{residual}}^{(it)}\|_2}{F_{\text{norm}}} \leq \Psi_f \quad (3.30)$$

and the displacements criterion by;

$$\frac{\|\Delta \underline{U}^{(it)}\|_2}{D_{\text{norm}}} \leq \Psi_d \quad (3.31)$$

where ‘*it*’ denotes the iteration number,  $F_{\text{norm}}$  is  $\max \|\Delta \underline{F}_{\text{external}}\|_2$  and  $D_{\text{norm}}$  is  $\|\underline{U}\|_2$ . Also,  $\Psi_f$ ,  $\Psi_d$  and  $\Psi_e$  are prescribed force, displacement and energy tolerances, respectively, where the energy criterion is given by:

$$\frac{\Delta \underline{U}^{(it)T} (\Delta \underline{F}_{\text{residual}}^{(it)})}{\Delta \underline{U}^{(1)T} (\Delta \underline{F}_{\text{residual}}^{(1)})} \leq \Psi_e \quad (3.32)$$

### 3.6 Numerical examples

Five numerical examples are used to illustrate the performance of the proposed SUR approach for the non-linear FE analysis of QB structures. The purpose of the study is not to examine the accuracy of the isotropic damage model, but rather to illustrate the convergence characteristics of the new SUR approach and illustrate its potential benefits. Therefore, the examples were chosen for their numerical characteristics and, with one exception, are not based upon real experiments or structures.

The first example considers a 1D bar problem, fixed at one end and loaded by prescribed displacement at the other end (see Figure 3.4). The second example is a 2D notched fracture specimen, loaded by prescribed displacement along its upper boundary, as shown in Figure 3.11. The third example is based on the reinforced concrete prism tested by Elfgren and Noghabai (2001) (see Figure 3.26). The fourth example is a 2D double notched specimen subject to mixed mode loading by prescribed displacement, as illustrated in Figure 3.33. The final example adopts the same configuration as used in example 3.6.2 but with larger dimensions (see Figure 3.40). However, this example is only used to explore the effect of varying the two main parameters of SUR function ( $\nu$  and  $a_p$ ) on the convergence performance of the solution. The material parameters used for all examples are given in Table 3.2. All 2D meshes comprised bilinear isoparametric elements.

Examples 3.6.1 to 3.6.4 are considered with the proposed SUR approach and reference solution ‘secant’ method.

In all examples, the loading was monotonic and consistent convergence parameters were used for all analyses within an example. Thus, the form of the unloading-reloading curve would not be expected to have a major influence on the overall predicted response but predominantly affect the convergence characteristics. The former was indeed the case, as may be seen from the load-displacement responses given below. It should be mentioned that the true unloading-reloading response exhibits hysteresis behaviour that is not simulated here, thus the unloading path is assumed to follow the smooth unloading-reloading curve shown in Figure 3.1.

Table 3.2: Material properties and convergence tolerances.							
Example No.	$E_c$ (GPa)	$E_s$ (GPa)	$\nu$	$f_t$ (MPa)	$G_f$ (N/mm)	$\Psi_f$	$\Psi_d$
3.4.1	20	-	0.20	2.5	0.10	$10^{-3}$ & $10^{-6}$	$10^{-3}$ & $10^{-6}$
3.4.2	20	-	0.20	2.5	0.10	$10^{-3}$ & $10^{-6}$	$10^{-3}$ & $10^{-6}$
3.4.3	42	200	0.20	2.5	0.10	$10^{-3}$	$10^{-3}$
3.4.4	20	-	0.20	2.5	0.10	$10^{-3}$	$10^{-3}$
3.4.5	30	-	0.20	2.5	0.10	$10^{-3}$	$10^{-3}$

Convergence of the incremental-iterative solutions was based on the decay of both the L2 iterative displacement and out of balance force norms, i.e. the convergence of both of these norms was achieved for all steps of every solution. Two levels of convergence tolerance have been used in the examples: the first being a tolerance of 0.1%, which is considered adequate for all practical analyses. The second tolerance of 0.0001% is used in the first two examples to explore the convergence characteristics beyond the first limit. The latter was not used in all examples because, (i) the results show that there is no appreciable difference in the results from a solution with a 0.1% limit compared with those obtained using 0.0001% tolerance, and (ii) the very high number of iterations required by the reference ‘secant’ solution made full comparisons difficult to obtain for the later examples.

In these examples, the solution characteristics are illustrated by showing the number of iterations required to achieve convergence for selected increments. In all cases, the increments chosen are those which required the most iterations to achieve convergence thus are termed ‘difficult increments’.

### Example 3.6.1: One-dimensional tensile test

The 1D bar problem considered in this example, as can be seen in Figure 3.4, was fixed at one end and loaded by prescribed displacement of 0.2 mm at the other end. The 1D bar was divided into 3 linear elements of equal length, with the middle

element being assigned a small amount of initial damage such that damage only occurred in this central element.

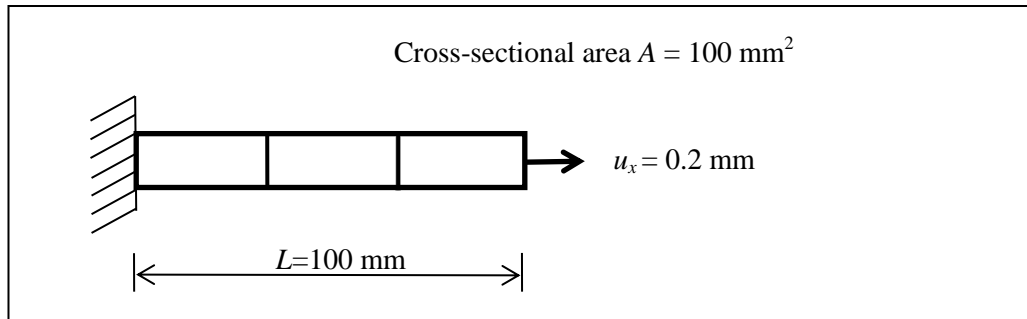


Figure 3.4: 1D bar subjected to 0.2 mm prescribed displacement.

Two sets of analyses were undertaken, one in which the 0.2mm displacement was applied over 40 increments and the other set with 100 increments. In addition, both sets of analyses were carried out with 0.1% and 0.0001% convergence tolerances.

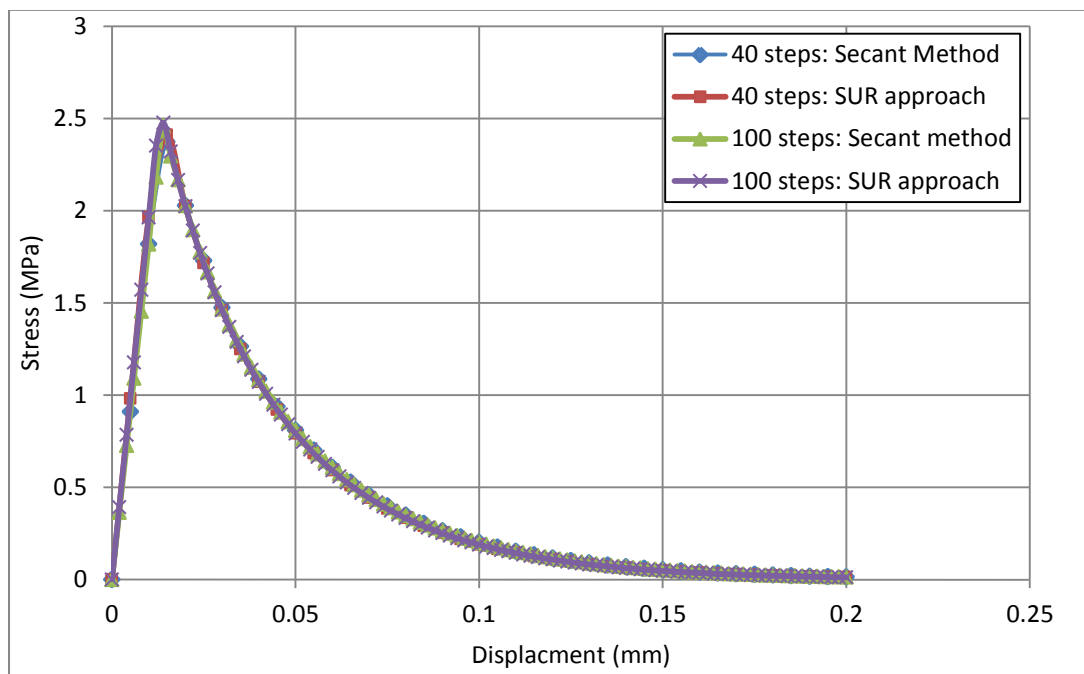


Figure 3.5: Displacement-stress relationship for the 1D bar with 40 and 100 increments (convergence tolerance =0.1%).

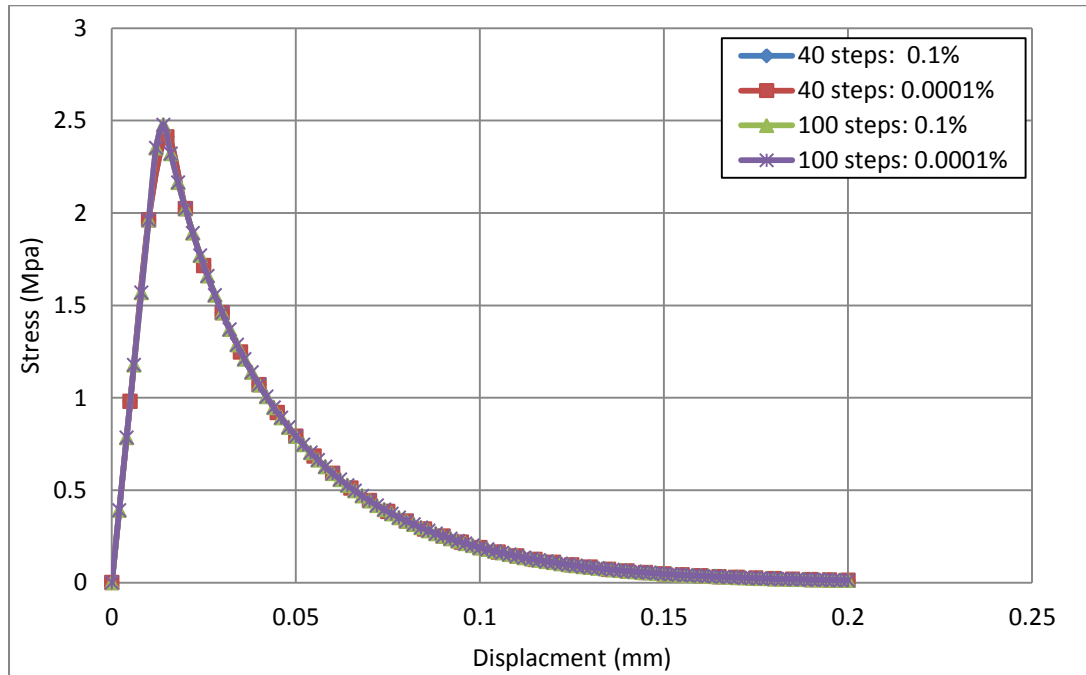


Figure 3.6: Displacement-stress relationship for the 1D bar using SUR approach with  $10^{-3}$  and  $10^{-6}$  convergence tolerances.

The resulting stress-displacement responses from the two sets of analyses are shown in Figure 3.5 and, as expected, the results from the various analyses are indistinguishable from each other. This is also the case for the results obtained using the different convergence tolerances of  $10^{-3}$  and  $10^{-6}$ , as can be seen in Figure 3.6.

Figures 3.7 to 3.10 present the number of iterations required to achieve convergence at the most difficult steps. In all sets of analyses, the developed SUR approach achieved converged solutions with far fewer iterations than the secant method.

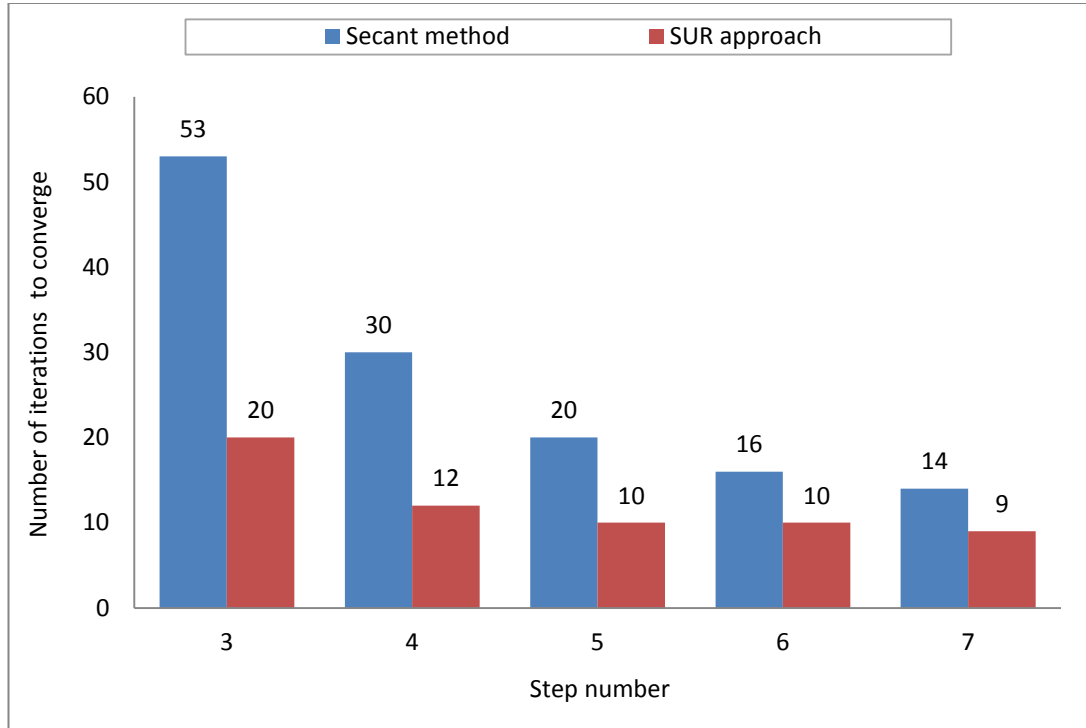


Figure 3.7: Number of iterations to achieve convergence for the most difficult increments of the 1D bar with 40 increments (convergence tolerance =  $10^{-6}$ ).

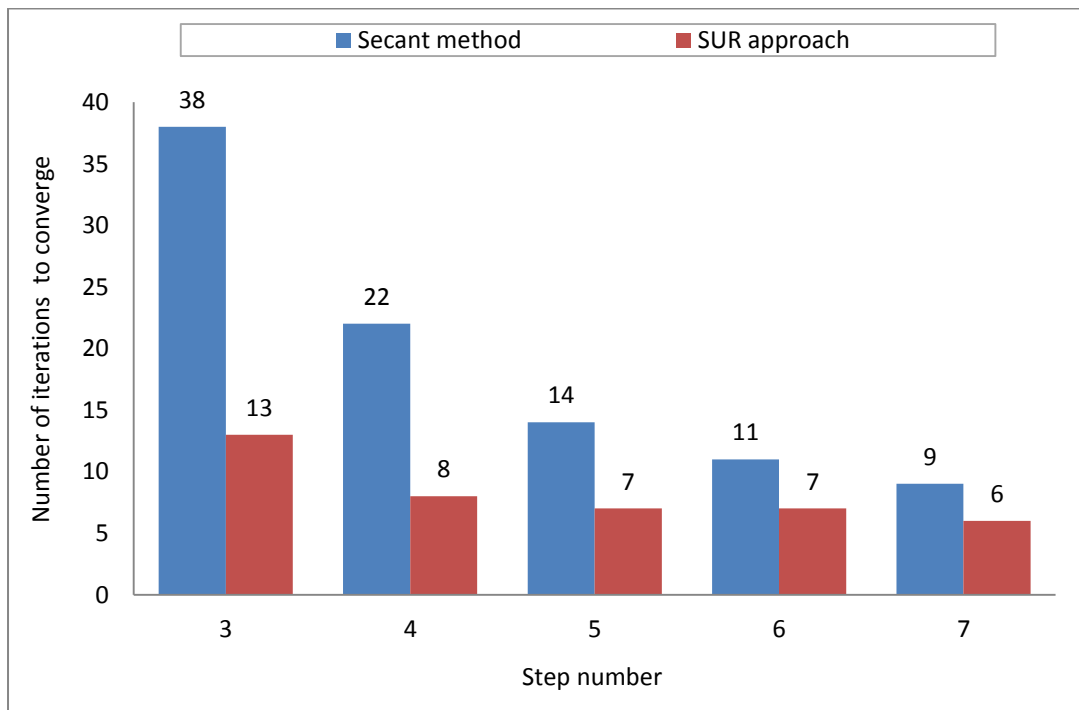


Figure 3.8: Number of iterations to achieve convergence for the most difficult increments of the 1D bar with 40 increments (convergence tolerance =  $10^{-3}$ ).

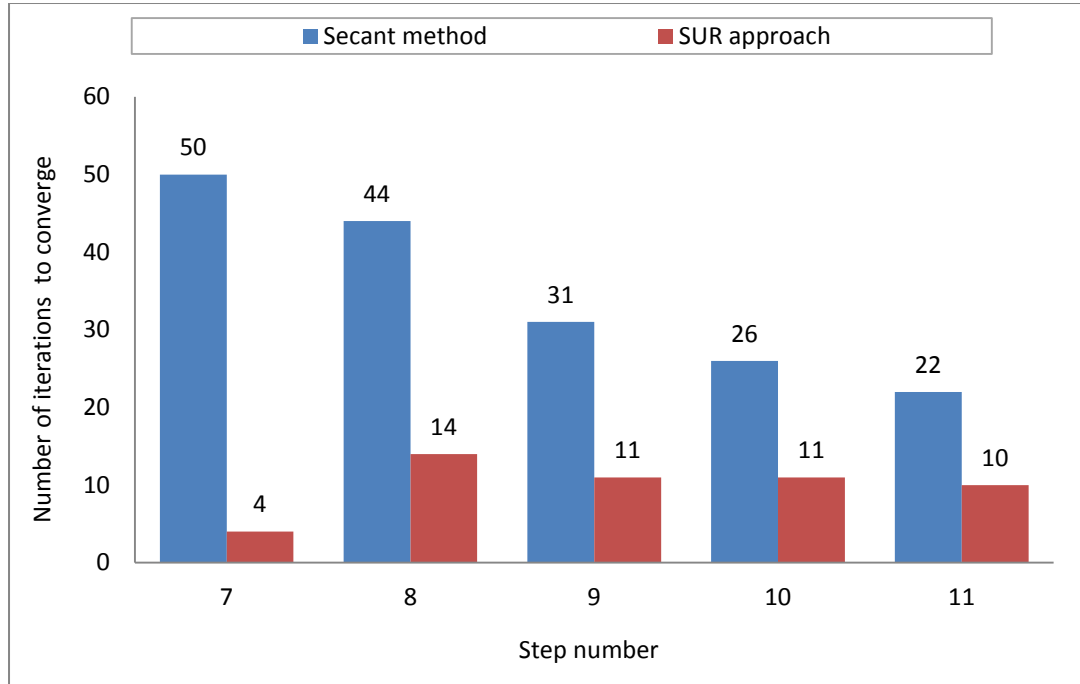


Figure 3.9: Number of iterations to achieve convergence for the most difficult increments of the 1D bar with 100 increments (convergence tolerance= $10^{-6}$ ).

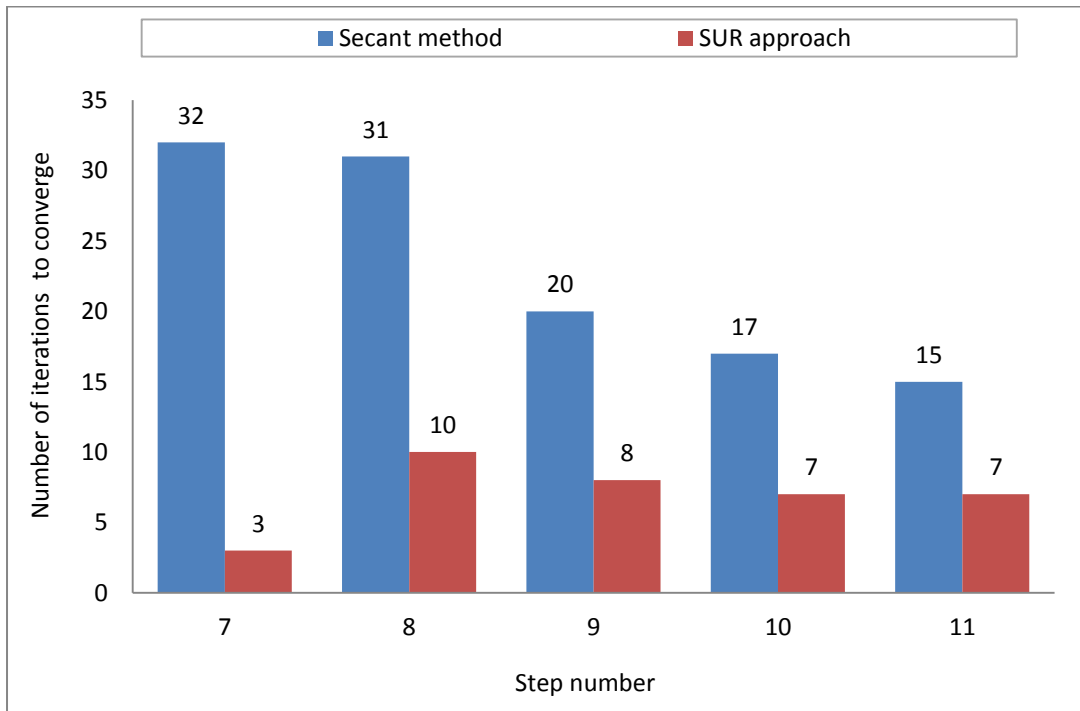


Figure 3.10: Number of iterations to achieve convergence for the most difficult increments of the 1D bar with 100 increments (convergence tolerance= $10^{-3}$ ).

### Example 3.6.2: Two-dimensional plane stress specimen

The idealised 2D structure, shown in Figure 3.11, considered in this example is discretised with the coarse and fine meshes, as can be seen in Figure 3.12. The analysis was undertaken using 2 different prescribed displacement increments, one using 50 steps and the other 100 steps. Also, two convergence tolerances  $10^{-3}$  and  $10^{-6}$  were used for the analysis. In addition, Figure 3.14 shows damage contour plots at different displacement increments for Mesh1 with 50 increments.

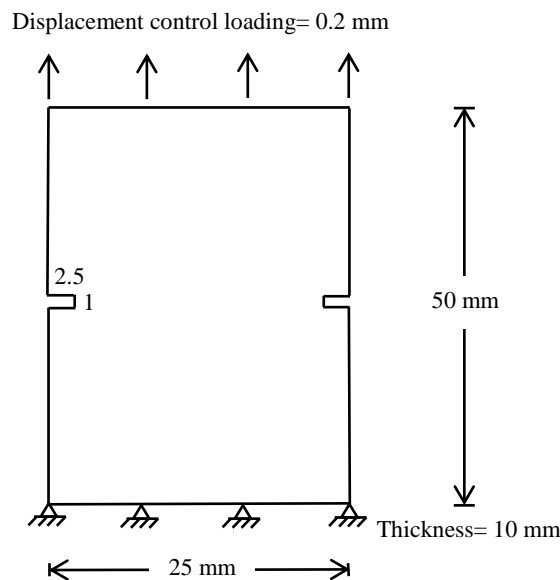


Figure 3.11: Dimension of the 2D notched plane stress example.

Exaggerated deformed mesh plots are given in Figure 3.13. The numerical load displacement responses from the analyses using the two approaches with Mesh1 and Mesh2 using 50 and 100 steps are shown in Figures 3.15 and 3.16. Also, the stress-displacement responses for Mesh1 using the SUR approach for two convergence tolerances  $10^{-3}$  and  $10^{-6}$  are presented in Figure 3.17. In addition, a comparison between the number of iterations needed for the two solutions to converge at the most difficult steps can be seen in Figures 3.18 to 3.25. The increments requiring the most iterations are those associated with crack initiation and early crack propagation.

These normally coincide with the peak and early post-peak sections of the overall response curve (Hellweg and Crisfield, 1998).

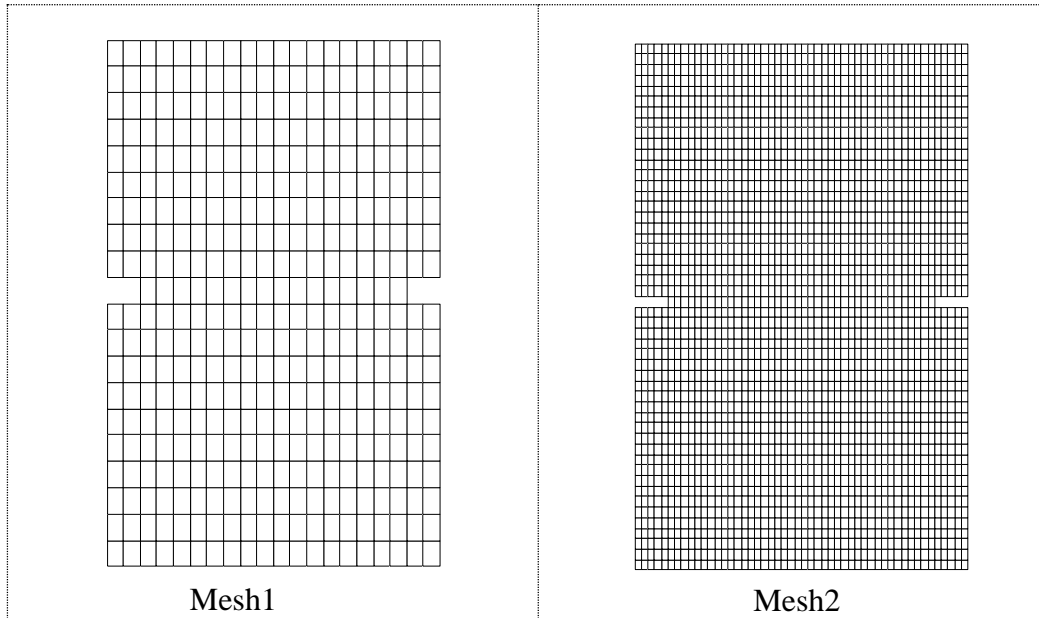


Figure 3.12: Finite element mesh.

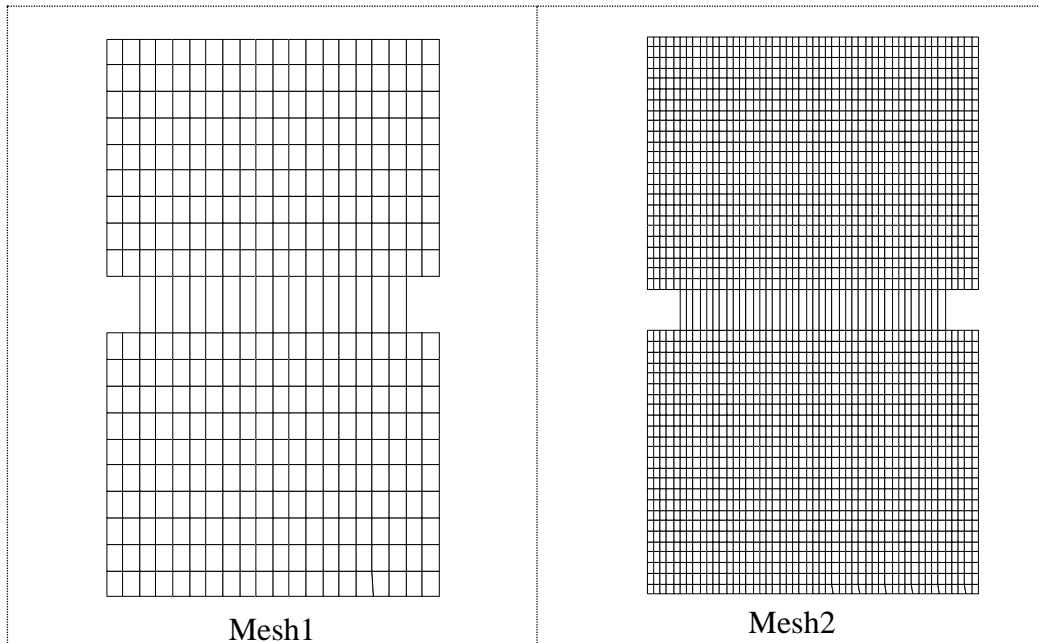


Figure 3.13: Exaggerated deformed mesh plots at final increment for Mesh1 and Mesh2.

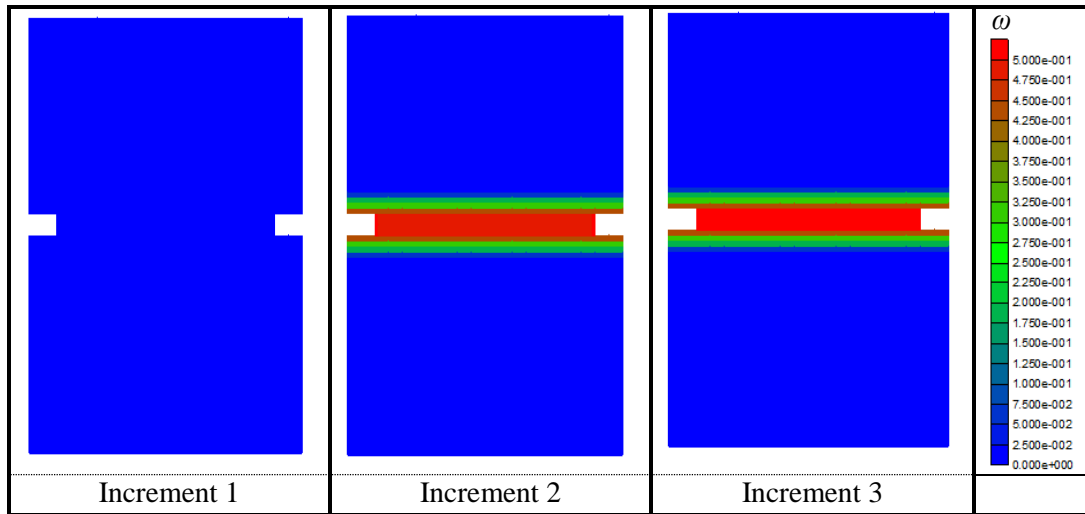


Figure 3.14: Damage contour plots for different displacement increment (2D plane stress example).

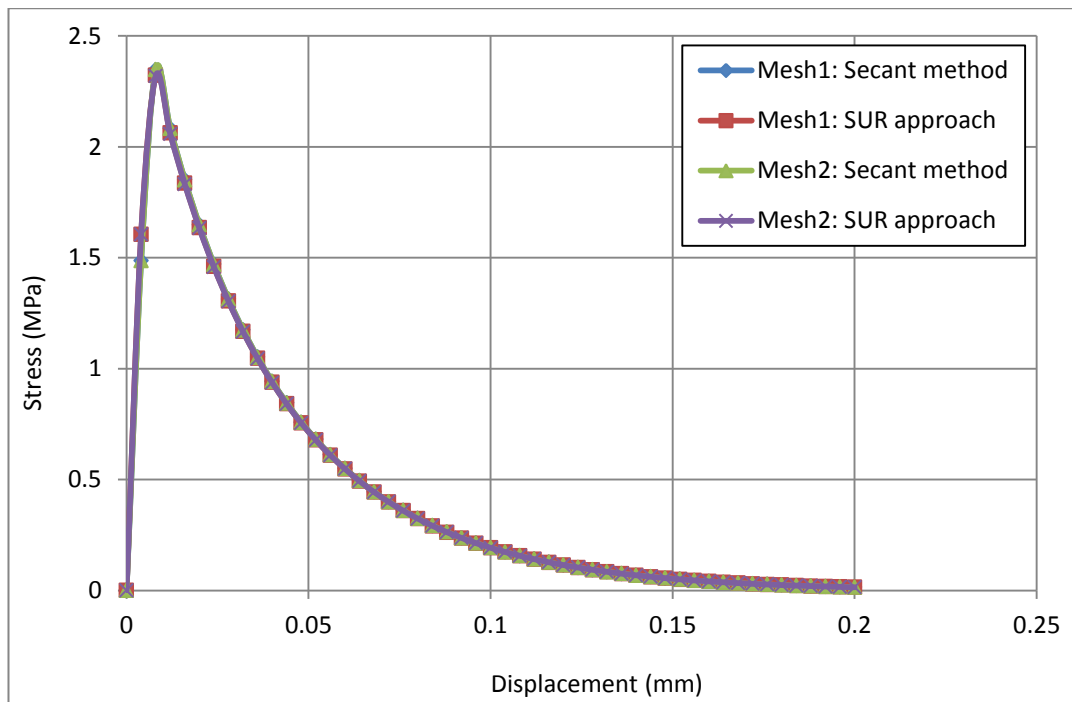


Figure 3.15: Displacement-Stress relationship for 2D plane stress example with 50 steps.

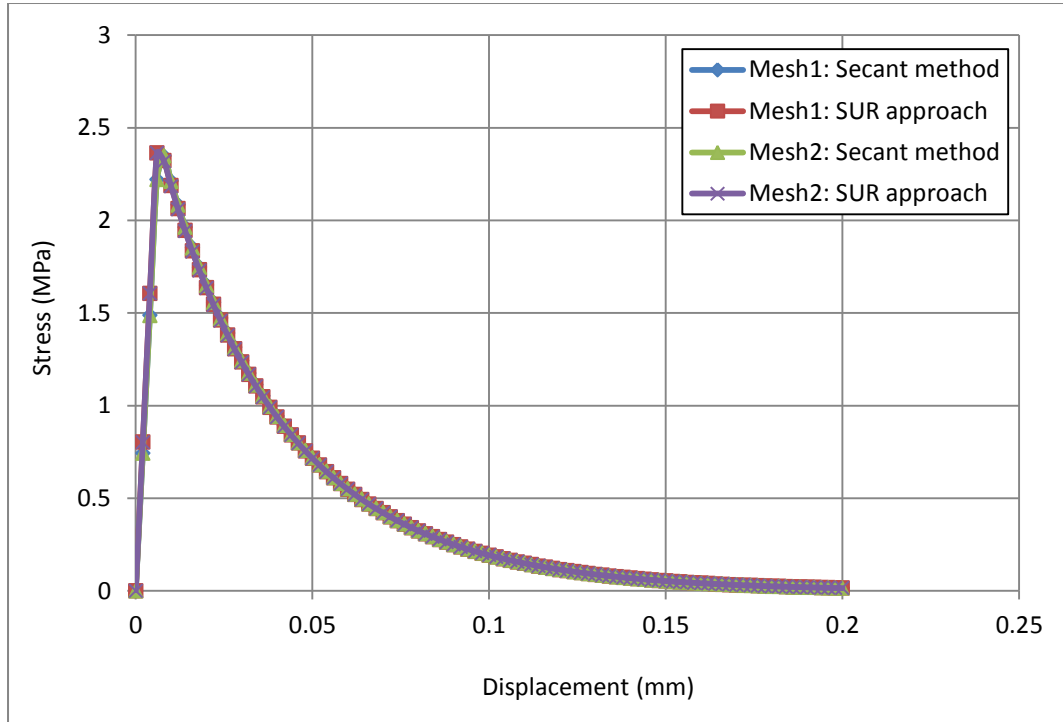


Figure 3.16: Displacement-Stress relationship for 2D plane stress example with 100 steps.

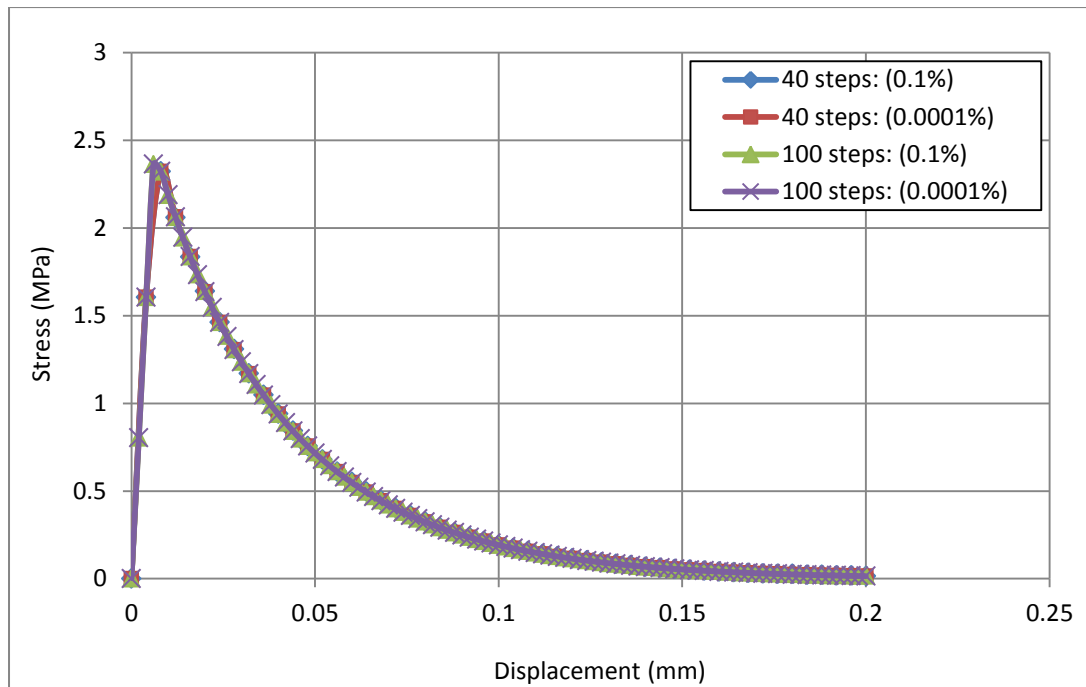


Figure 3.17: Displacement-Stress relationship for Mesh1 using SUR approach with convergence tolerances  $10^{-3}$  and  $10^{-6}$ .

As in example 3.6.1, the stress-displacement results obtained with both convergence tolerances ( $10^{-3}$  and  $10^{-6}$ ) are indistinguishable from each other, as can be seen in Figure 3.17. Also, as with example 3.6.1, the savings gained by using the SUR approach are considerable.

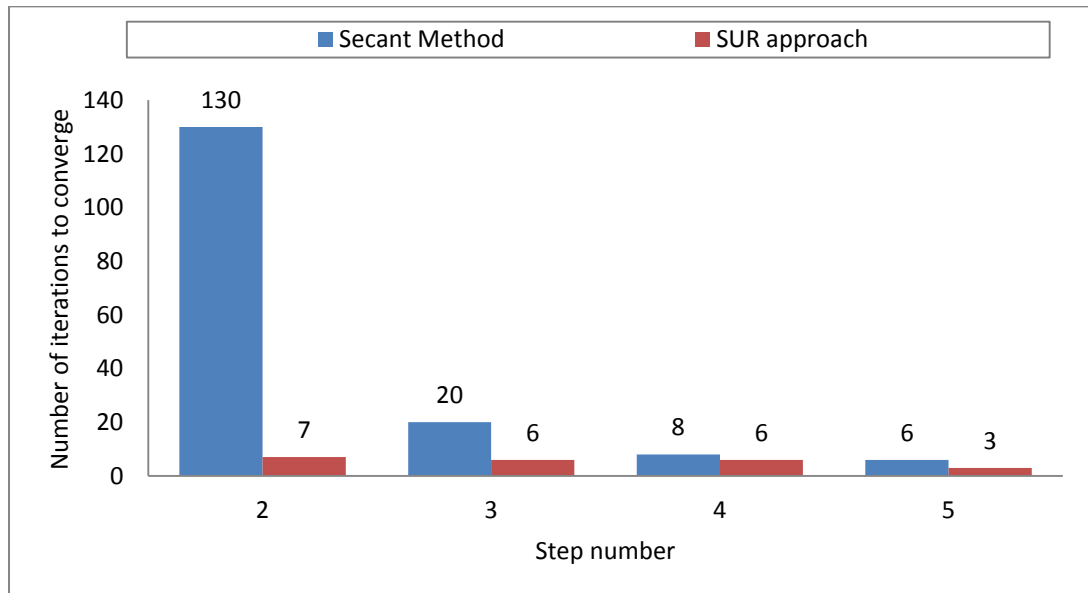


Figure 3.18: Number of iterations to achieve convergence for the most difficult increments of Mesh1 with 50 increments (convergence tolerance= $10^{-3}$ ).

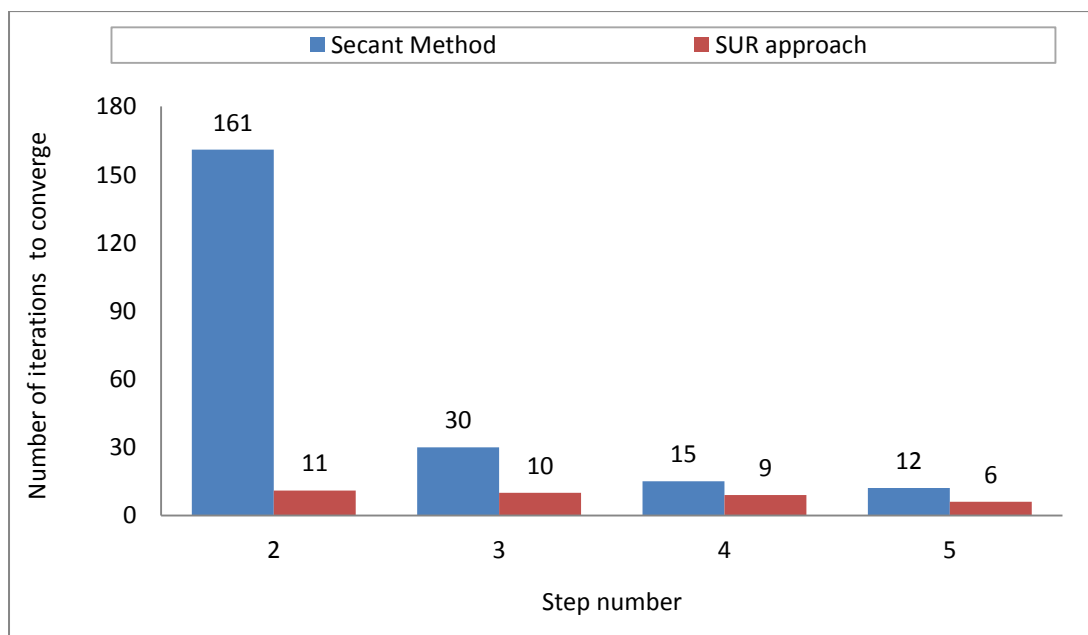


Figure 3.19: Number of iterations to achieve convergence for the most difficult increments of Mesh1 with 50 increments (convergence tolerance= $10^{-6}$ ).

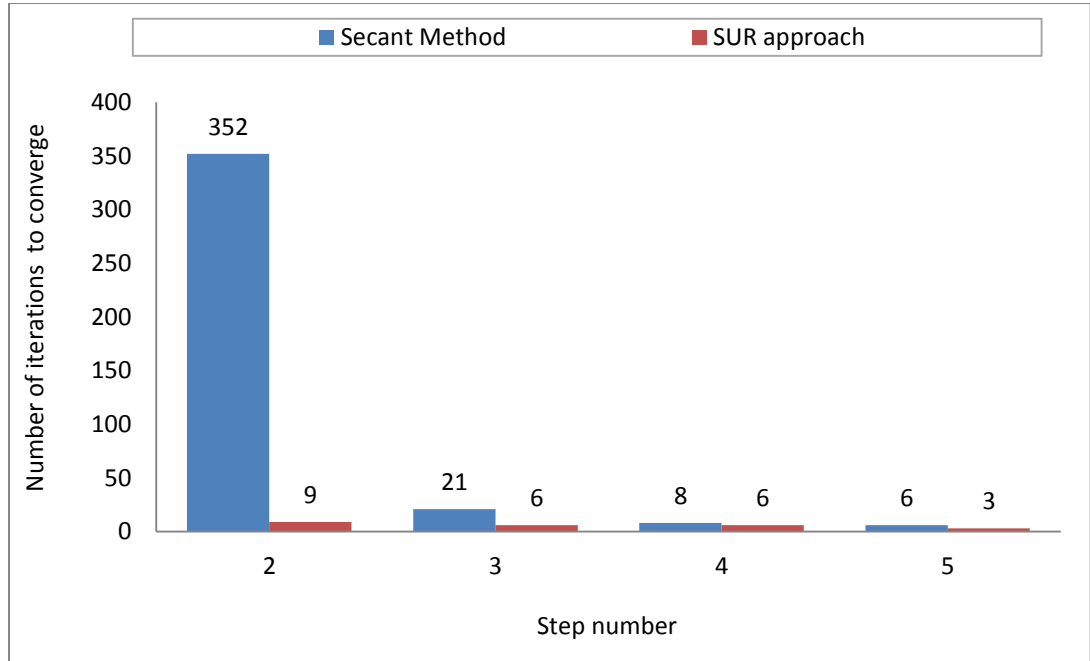


Figure 3.20: Number of iterations to achieve convergence for the most difficult increments of Mesh2 with 50 increments (convergence tolerance= $10^{-3}$ ).

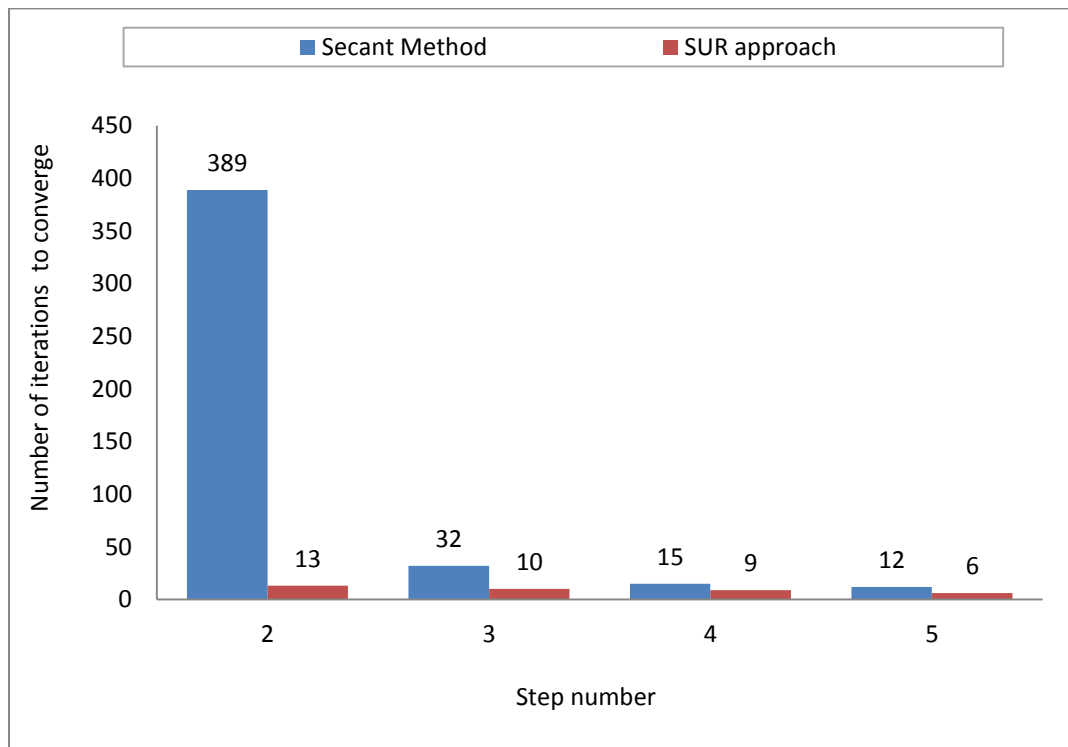


Figure 3.21: Number of iterations to achieve convergence for the most difficult increments of Mesh2 with 50 increments (convergence tolerance= $10^{-6}$ ).

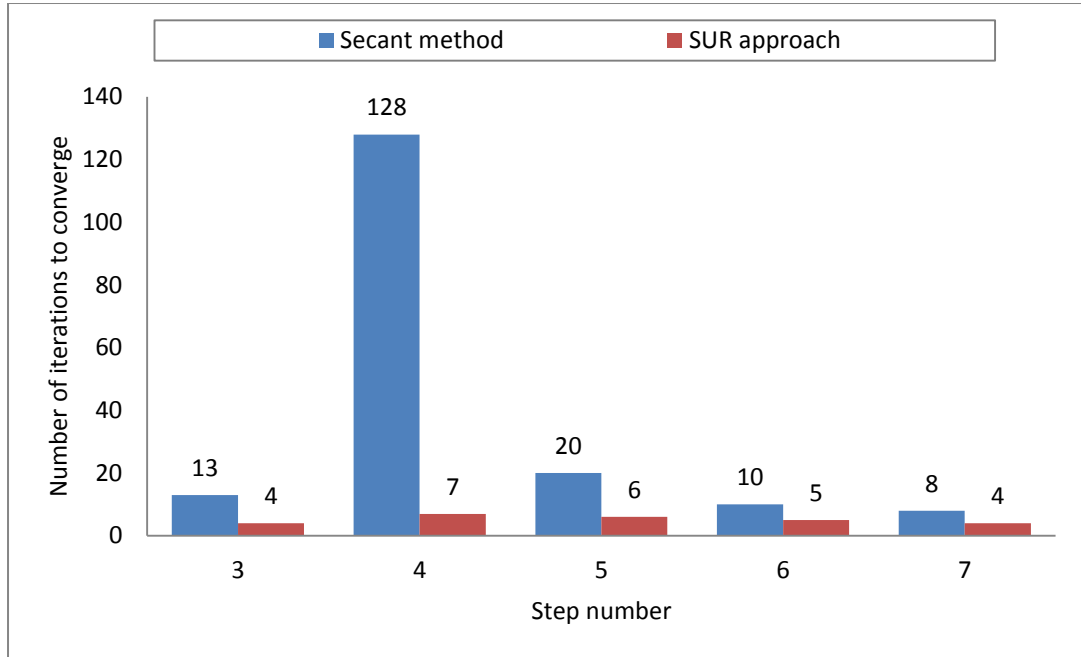


Figure 3.22: Number of iterations to achieve convergence for the most difficult increments of Mesh1 with 100 increments (convergence tolerance= $10^{-3}$ ).

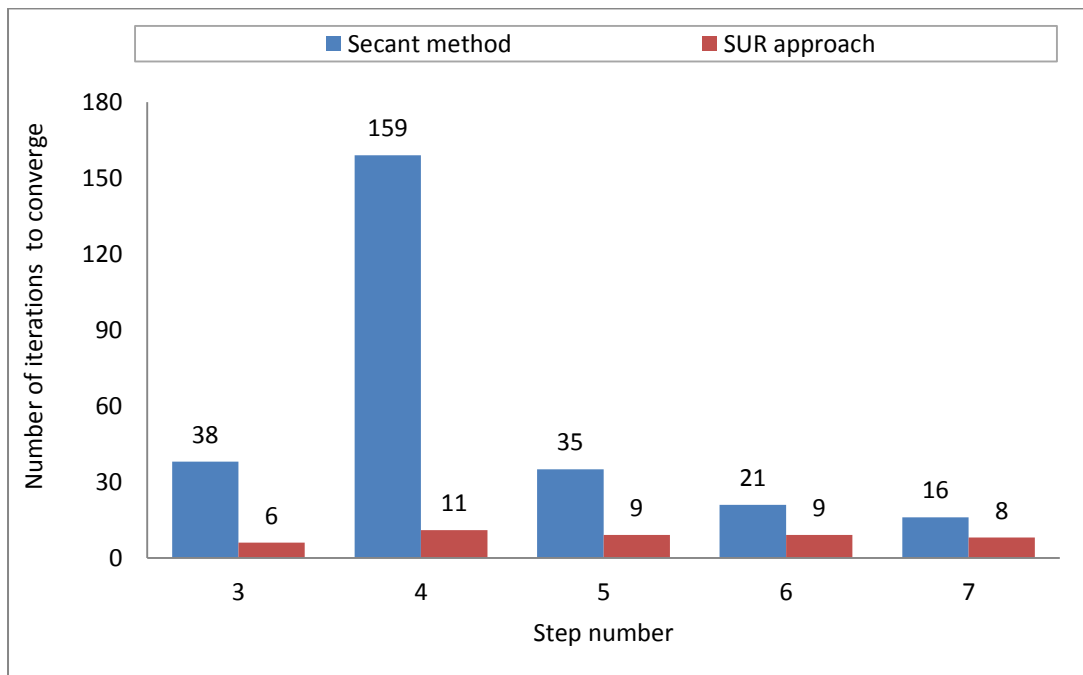


Figure 3.23: Number of iterations to achieve convergence for the most difficult increments of Mesh1 with 100 increments (convergence tolerance= $10^{-6}$ ).

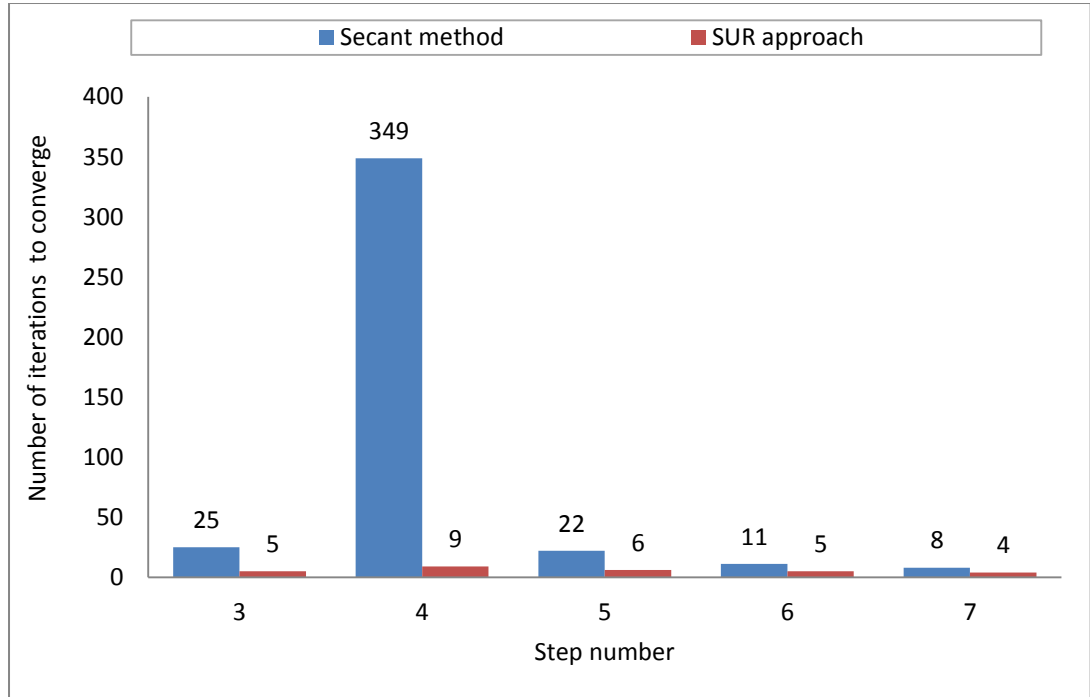


Figure 3.24: Number of iterations to achieve convergence for the most difficult increments of Mesh2 with 100 increments (convergence tolerance= $10^{-3}$ ).

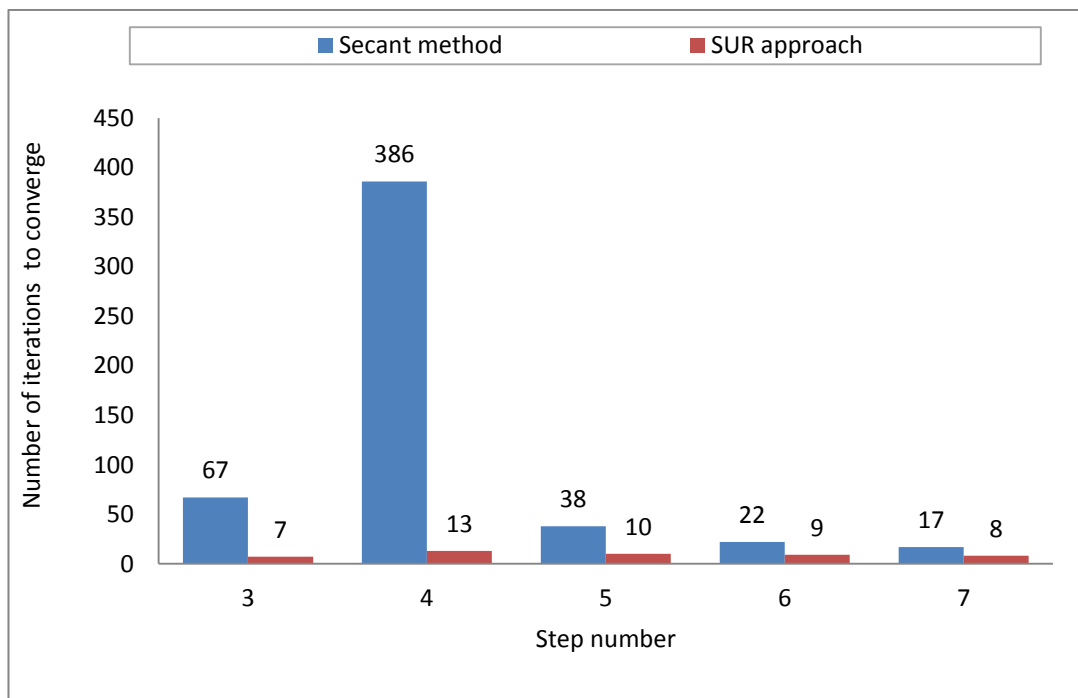


Figure 3.25: Number of iterations to achieve convergence for the most difficult increments of Mesh2 with 100 increments (convergence tolerance= $10^{-6}$ ).

### Example 3.6.3: Reinforced concrete prism

The RC specimen considered in this example was reinforced with a single central reinforcement bar, as illustrated in Figure 3.26. The specimen is modelled in 2D with plane stress elements. As illustrated in Figure 3.26, the bar is assumed to be square and the concrete at this level is ignored. It is recognised that this represents a considerable simplification of the true 3D specimen. The analyses were carried out with 50 and 100 prescribed displacement increments to reach a displacement of 1mm at the load position. The finite element mesh, which represents  $\frac{1}{4}$  of the specimen, is shown in Figure 3.27. The exaggerated deformed mesh plot of the  $\frac{1}{4}$  of the RC prism at the final increment (0.01 mm) is given in Figure 3.28. Furthermore, Figure 3.29 shows a contour plot of the damage parameter at the final increment.

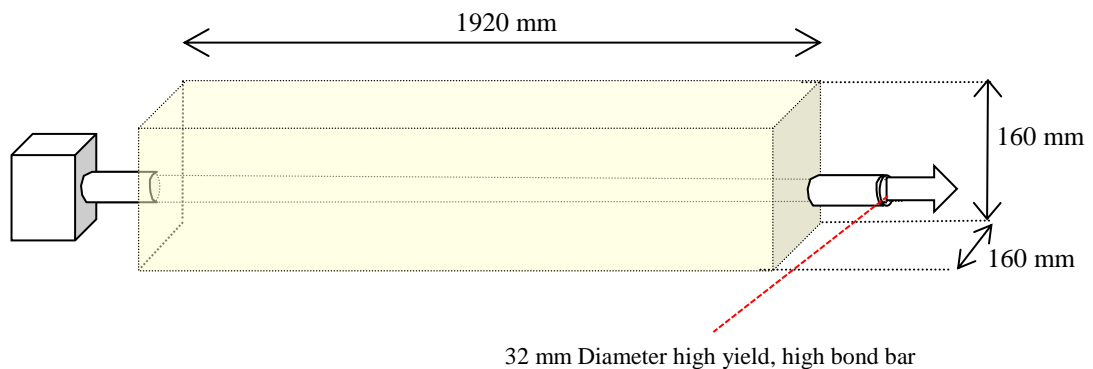


Figure 3.26: Dimension details of the RC prism.

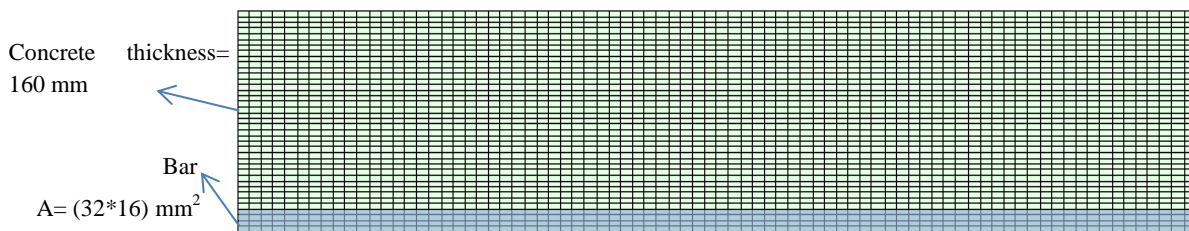


Figure 3.27: Finite element mesh of RC prism.

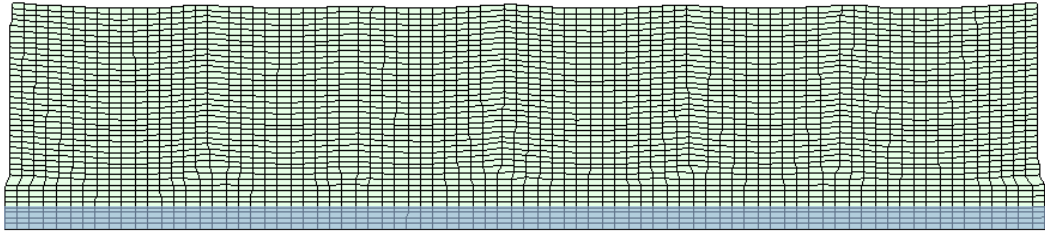


Figure 3.28: Exaggerated deformed mesh plot at final increment.

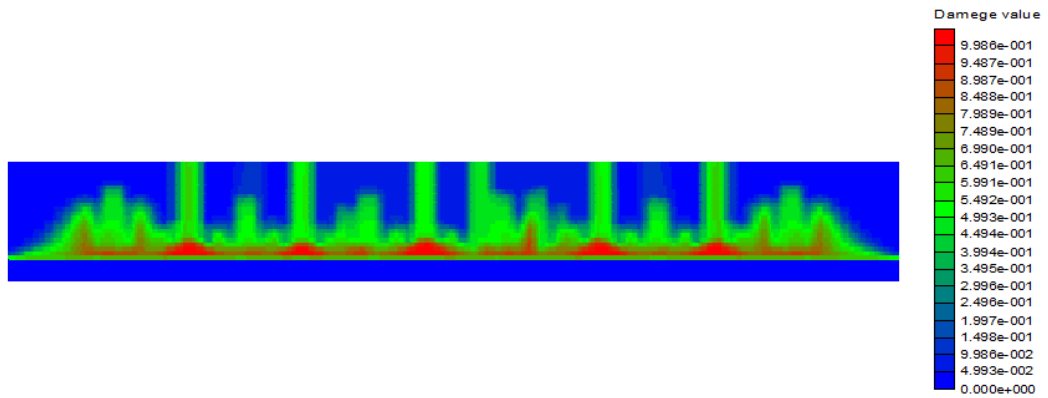


Figure 3.29: Damage value contour plot at final displacement increment.

Numerical stress-displacement responses from all of the analyses of this specimen are shown in Figure 3.30, in which the average stress is that in the elastic reinforcing bar.

The number of iterations required, for both the 50 and 100 step solutions, are presented in Figures 3.31 and 3.32, respectively. The efficiency of the SUR approach, relative to the secant approach, is again evident.

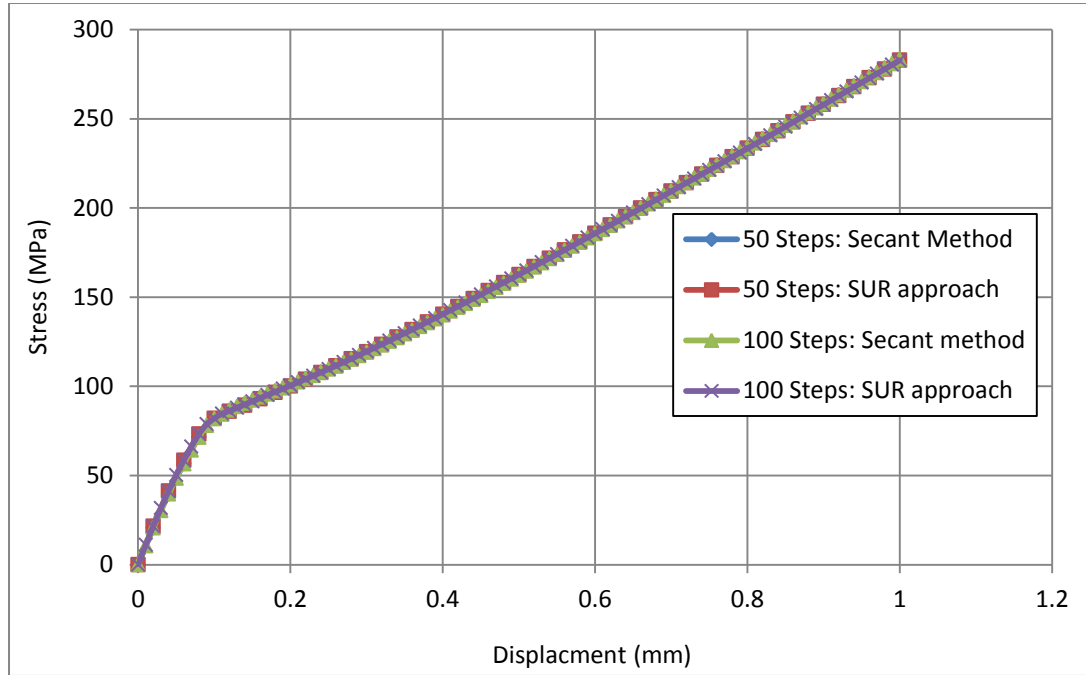


Figure 3.30: Load-displacement responses of reinforced bar.

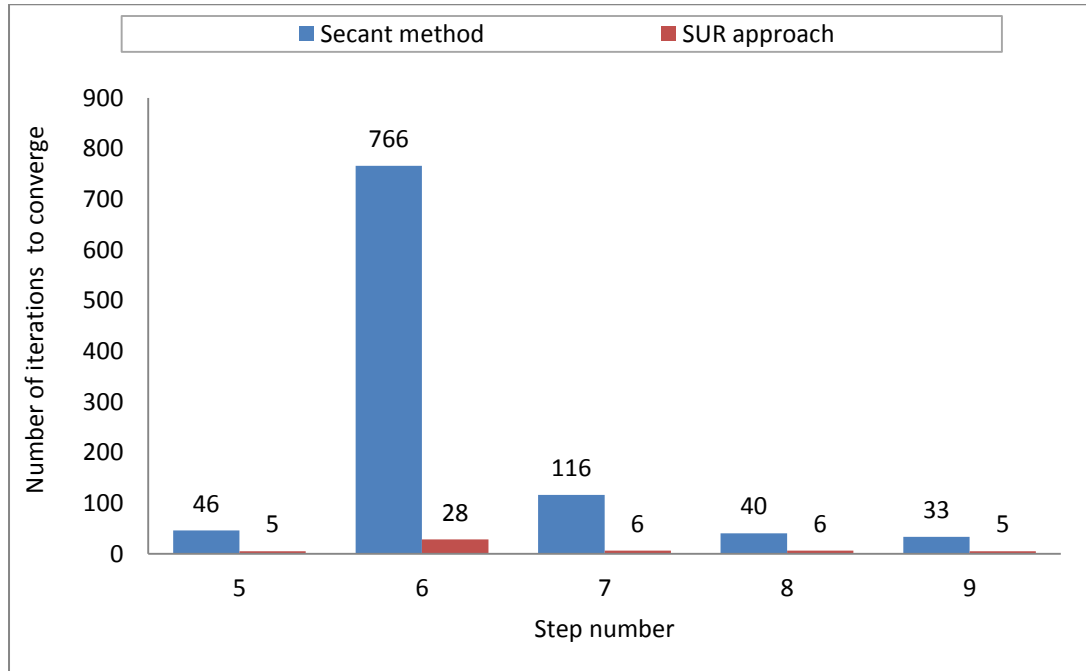


Figure 3.31: Number of iterations to achieve convergence for the most difficult increments of the RC prism with 50 increments.

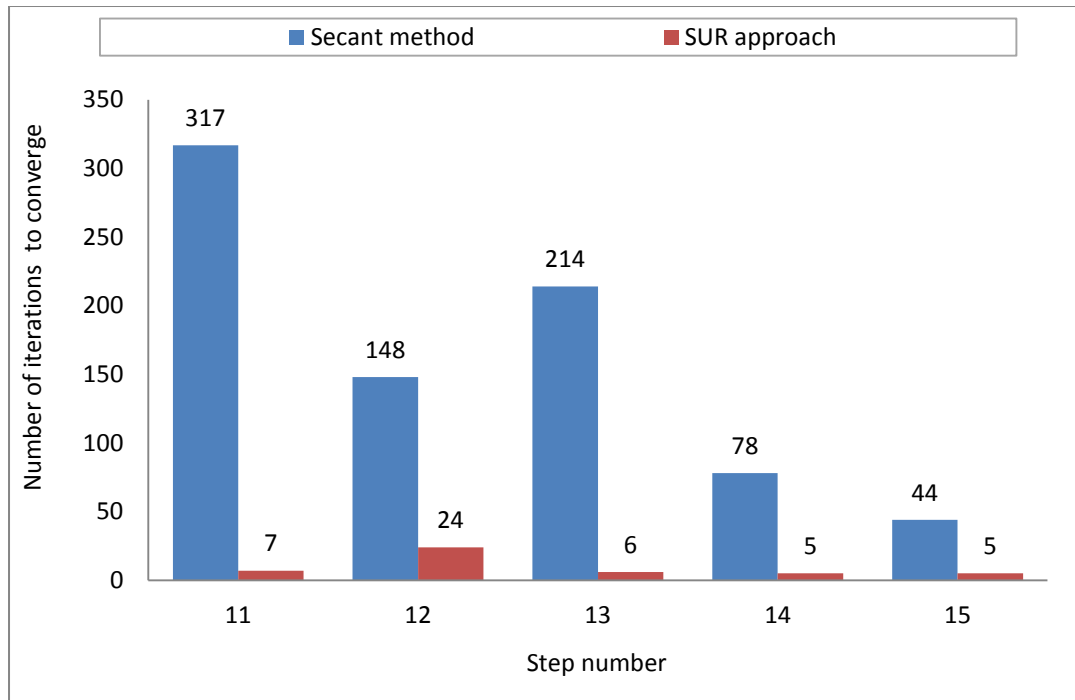


Figure 3.32: Number of iterations to achieve convergence for the most difficult increments of the RC prism with 100 increments.

#### Example 3.6.4: 2D double notched example

Figure 3.33 shows the 2D double notched specimen used for this example. This is subjected to a combination of shear and tensile loading via prescribed vertical and horizontal displacements. The analyses were undertaken using 40 and 100 prescribed displacement increments. The exaggerated deformed mesh plot of the 2D specimen using 100 steps at the final displacement increment is depicted in Figure 3.34. Also, contour plots of the damage parameter and principal stresses are shown in Figures 3.35 and 3.37, respectively.

Vertical displacement control loading = 0.15 mm, and 0.25 mm horizontally.

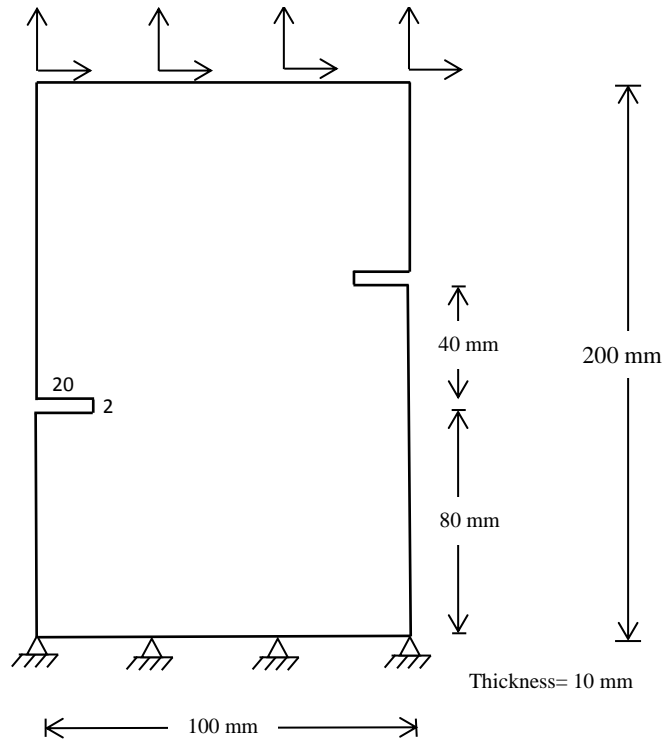


Figure 3.33: dimensional details of the double notched specimen.

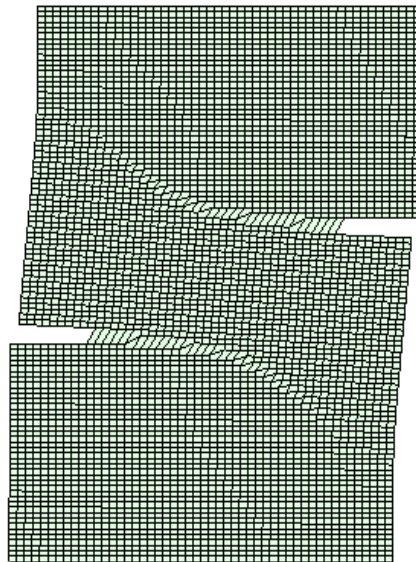


Figure 3.34: Exaggerated deformed mesh plot.

The results in Figure 3.36 give a graph of displacement versus average vertical stress for both the 40 and 100 step solutions. The average vertical stress in these plots is the sum of the vertical forces (reactions) on the upper surface divided by the un-notched cross-sectional area (i.e. the area at the top of the specimen). It can be noted that the average vertical stress becomes compressive in the latter stages of the analysis. This is consistent with the formation of a diagonal compression zone across the centre of the specimen (see Figure 3.37).

As with all other examples, the SUR solution is far more efficient than the reference Secant solution. Indeed, the SUR approach is robust and results in significant savings in terms of the total number of iterations required for a complete solution as illustrated in Figures 3.38 and 3.39.

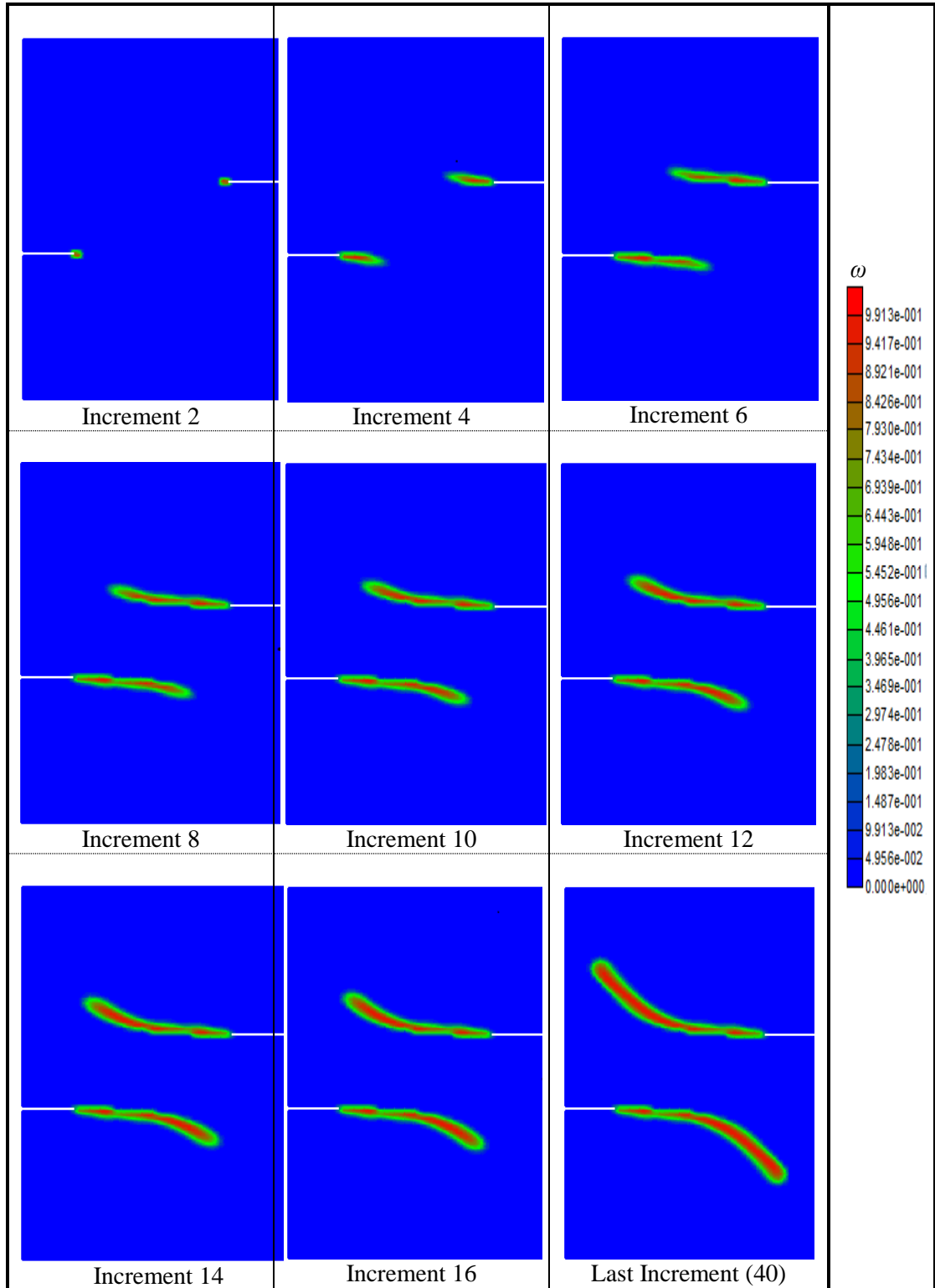


Figure 3.35: Damage indicator contour plots at different displacement increments.

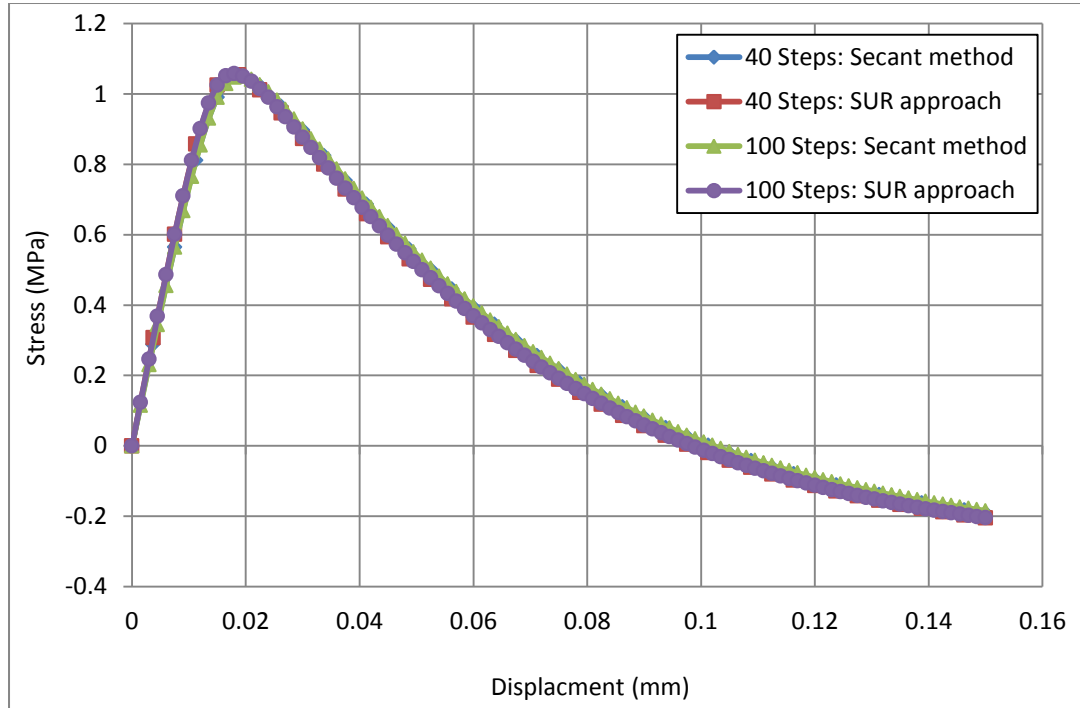


Figure 3.36: Numerical displacement and vertical stress responses with 40 and 100 prescribed displacement increments.

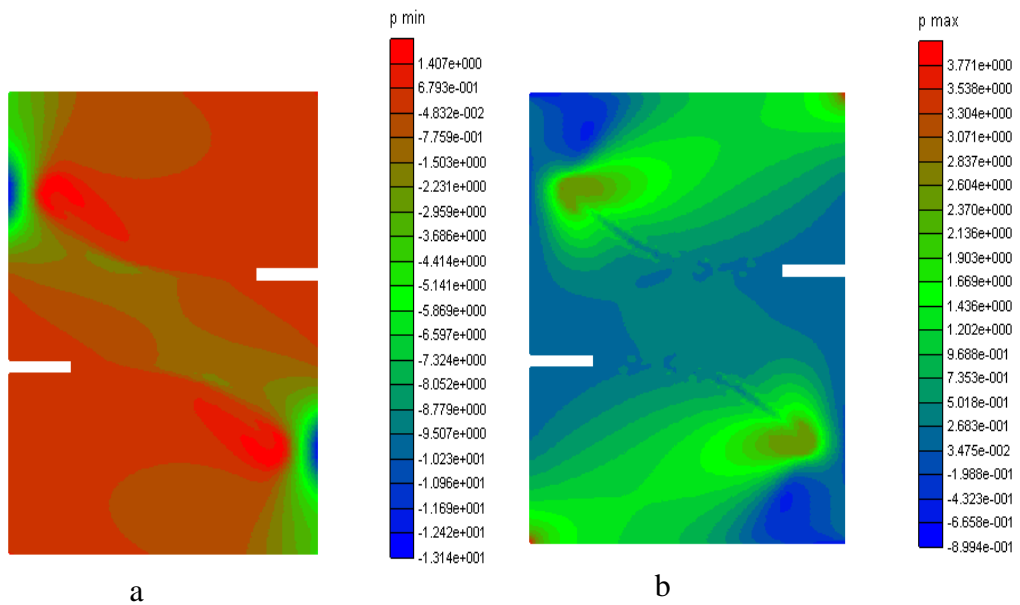


Figure 3.37: (a) Minimum principal stress contour plot, (b) Maximum principal stress contour plot, both at final displacement increment.

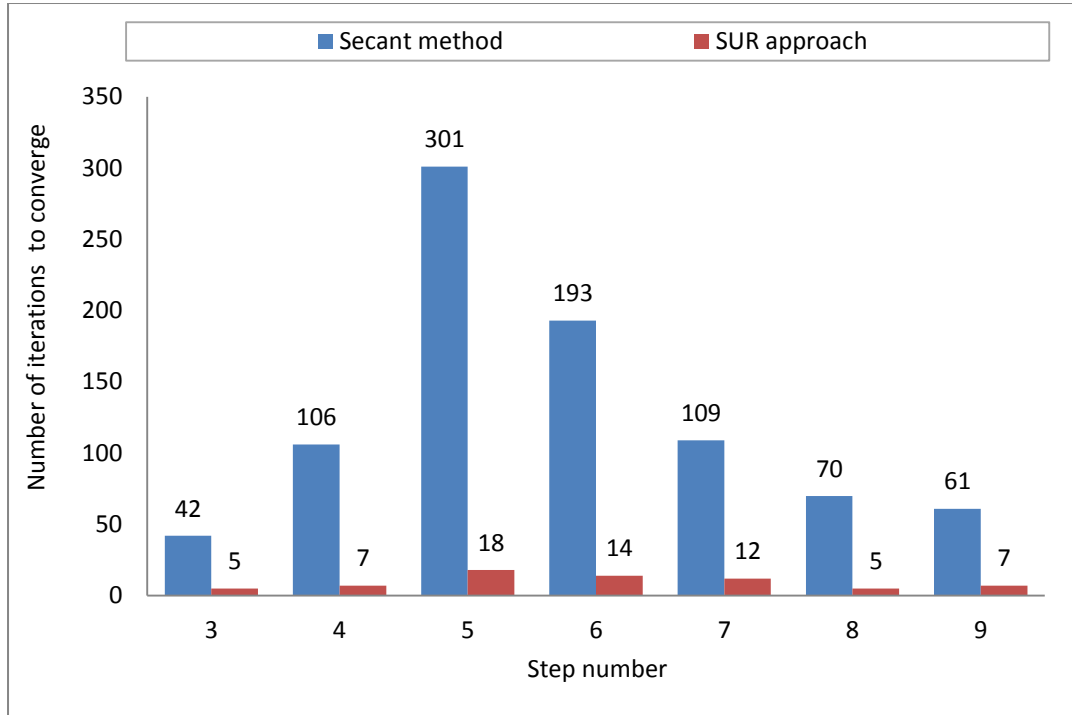


Figure 3.38: Number of iterations to achieve convergence for the most difficult increments with 40 increments.

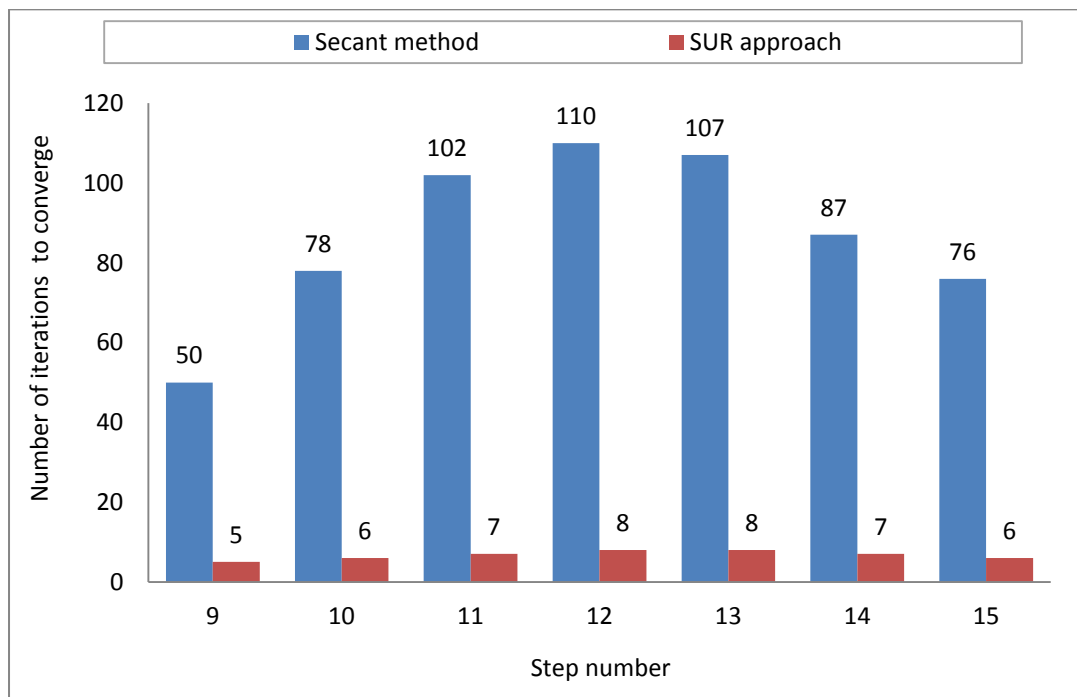


Figure 3.39: Number of iterations to achieve convergence for the most difficult increments with 100 increments.

### Example 3.6.5: Two-dimensional specimen

The purpose of this example is to illustrate the effect of varying the SUR parameters on the nonlinear solution characteristics. Therefore, unlike all of the previous examples, only the standard SUR approach is used for the analyses. The cases considered are; Case 1 ( $\nu=0.75$  and  $a_p=0.70$ ) and Case 2 ( $\nu=1.0$  and  $a_p=0.8$ ).

The analyses were carried out using a total prescribed displacement of 0.2 mm, applied evenly over 50 steps.

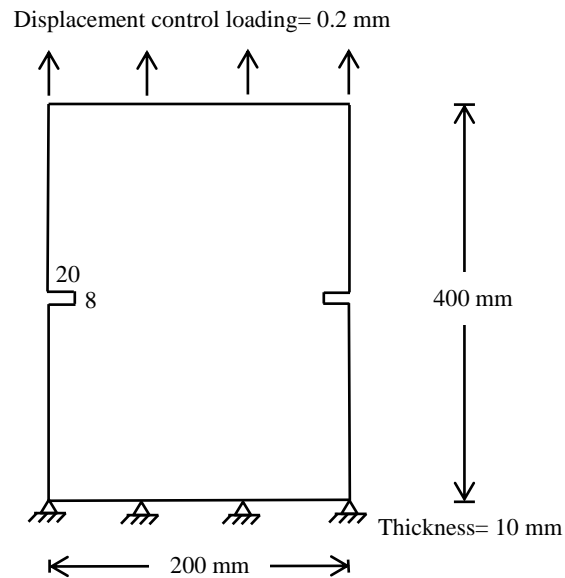


Figure 3.40: Dimensional details for 2D specimen.

The stress-displacement responses for both cases are given in Figure 3.41. The iteration history in Figure 3.41 shows that the Case 1 solution, with the standard SUR parameters, uses far fewer iterations than the Case 2 solution. The better performance of the former is attributed to the fact that the Case 1 SUR curve has a much smaller gradient at the intersection with the target curve than does the Case 2 SUR curve. This means that the ‘tangent matrix’ used in the Case 1 solution was closer to the true (negative) tangent and therefore resulted in less drift from the target solution in each iteration than in the Case 2 solution.

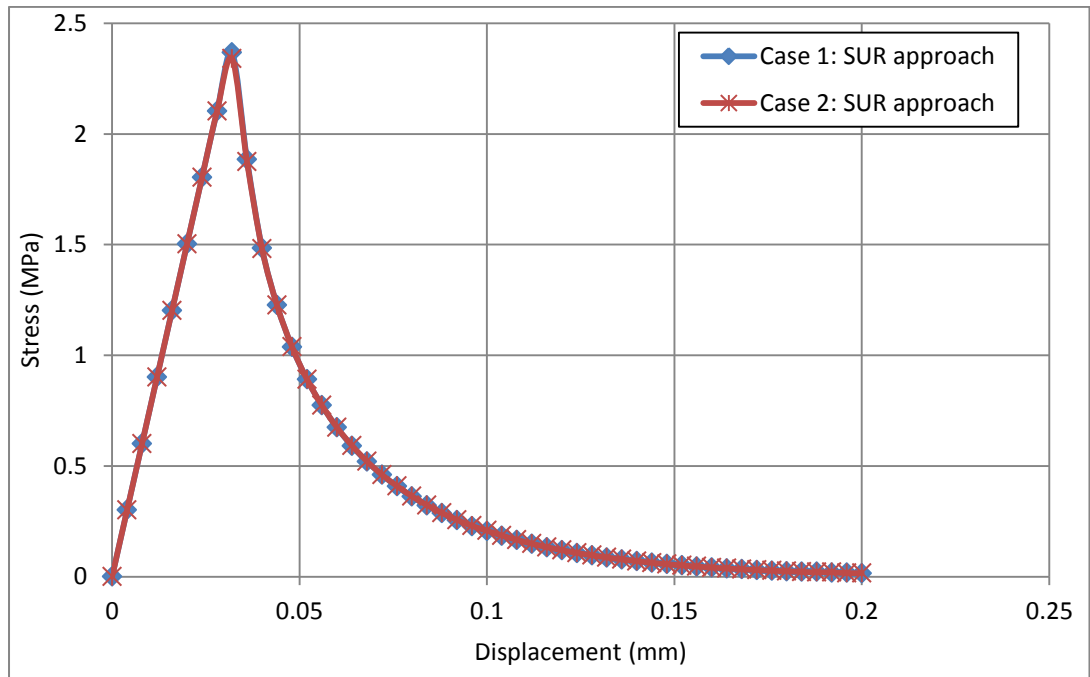


Figure 3.41: Displacement-Stress relationship for varying the two main parameters of SUR function.

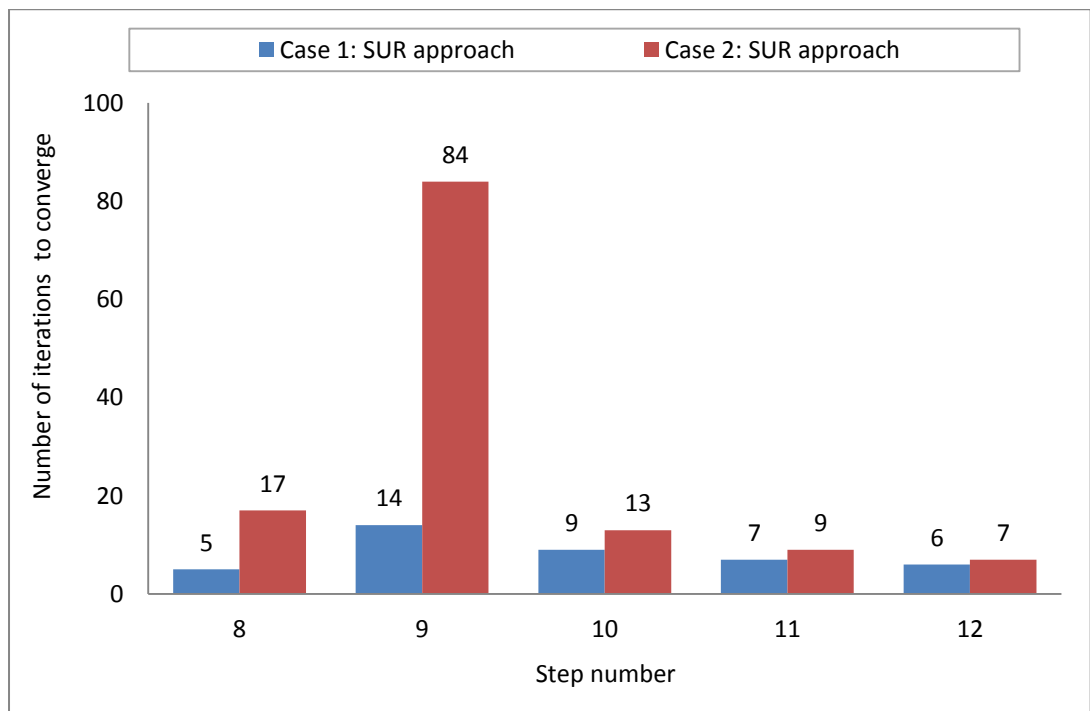


Figure 3.42: Number of iterations to achieve convergence for the most difficult increments of the SUR solution with Cases 1 and 2.

### 3.7 General discussion and conclusions

The conclusion from this study, and from the experience gained by using the SUR algorithm for all of the analyses presented as well as for other unreported examples, is that the suggested default parameters of 0.75 and 0.70, for  $\nu$  and  $a_p$  respectively, are suitable for a wide range of problems and provide the best overall balance between robustness and efficiency. These parameters may not result in the absolute minimum number of iterations in every case, but they did always result in very substantial reductions in iteration numbers relative to the reference secant solution. Overall, it has been found that the proposed SUR approach was robust and never resulted in a breakdown of the nonlinear solution procedure.

It can be observed that examples 3.6.3 and 3.6.4 have more than one ‘difficult increment’ which differs from the other examples. This can be attributed to the fact that the crack pattern evolves throughout the analysis and is not established in one defined step, which is in contrast to the behaviour in the other three examples.

A convergence tolerance of 0.1%, based on L2 norms of iterative displacements and out of balance forces, is sufficient for practical analyses. Using a tighter tolerance results in no appreciable change in results, as judged from damage patterns and response graphs. Using a tighter tolerance (e.g.  $10^{-6}$ ) results in more iterations than obtained with the slacker tolerance (e.g.  $10^{-3}$ ), but the conclusion that the SUR algorithm always uses far fewer iterations than the reference secant solution remains unchanged.

Solutions were attempted using a standard Newton solution with a consistent tangent matrix i.e. using a form of  $\mathbf{D}_{tan}$  based on the negative tangent of the target curve. The author found that frequent numerical breakdown occurred when such solutions were attempted, which is in agreement with the findings reported in much of the literature reviewed in Chapter 2 in Section 2.4.

The proposed SUR approach, which applies a smooth unloading-reloading function in a damage model and then uses this function as a basis for computing an approximate positive-definite finite element tangent matrix, is robust and results in considerable savings relative to a model that uses a secant unloading-reloading

function. Furthermore, results proved that numerical breakdown of the nonlinear solution procedure never arose when SUR approach was carried out.

The form of the SUR function greatly affects the convergence characteristics of the model, with functions that have small gradients at the intersection with the target softening curve performing best.

The method proposed for calculating the characteristic length parameter from an element Jacobian matrix is both accurate and efficient.

# Chapter 4

## Acceleration techniques for the smooth unloading-reloading method

---

### 4.1 Introduction

In this chapter, three acceleration techniques to improve the convergence properties of the recently developed smooth unloading-reloading (SUR) method, which was presented in Chapter 3, are proposed. The aim in developing these three acceleration algorithms was to enhance the efficiency of the SUR method. The effectiveness of these three approaches is examined using the same examples as those used in Chapter 3. The reason for this choice is that this allows the new SUR strategies to be compared directly with the standard SUR method described in the previous chapter.

### 4.2 Acceleration techniques

In this section three acceleration techniques are proposed for improving the convergence performance of the SUR solution procedure. These acceleration approaches are described below:

#### 4.2.1 Predictive-SUR approach

The one dimensional problem shown in Figure 4.1 is used to explain the theory of the proposed predictive-SUR approach. This problem comprises a one-dimensional bar, fixed at one end and loaded by prescribed displacement at the other end. A prescribed displacement ( $u_x$ ) of 0.2 mm is applied evenly over 40 increments. The bar is divided into 3 linear elements of equal length, with the middle element being

assigned a small amount of initial damage such that damage only occurs in this central element.

The material properties used for the analysis are: Young's modulus ( $E=20000$  MPa), Poisson's ratio ( $\nu=0.2$ ), tensile strength ( $f_t=2.5$  MPa) and the fracture energy ( $G_f=0.1$  N/mm).

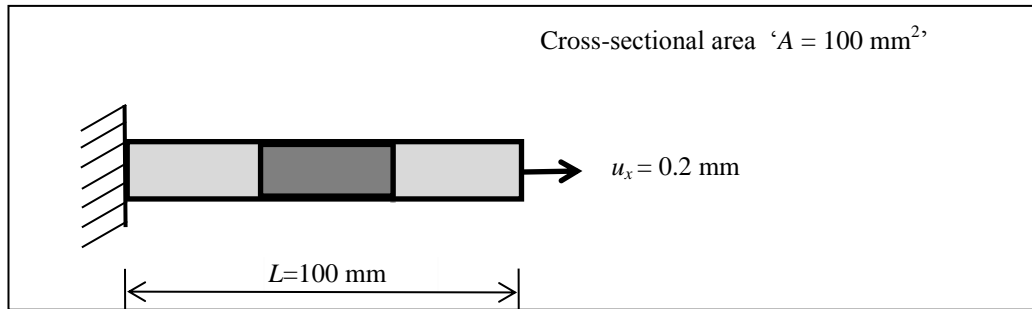


Figure 4.1: 1D bar subjected to 0.2 mm prescribed displacement.

Figure 4.2 shows the number of iterations required to achieve convergence to a tolerance of  $10^{-6}$ , based on an L2 out of balance force norm ( $\Psi_f$ ). This shows that the 'most difficult' increment was number 3, i.e. the increment that required the greatest number of iterations to achieve convergence.

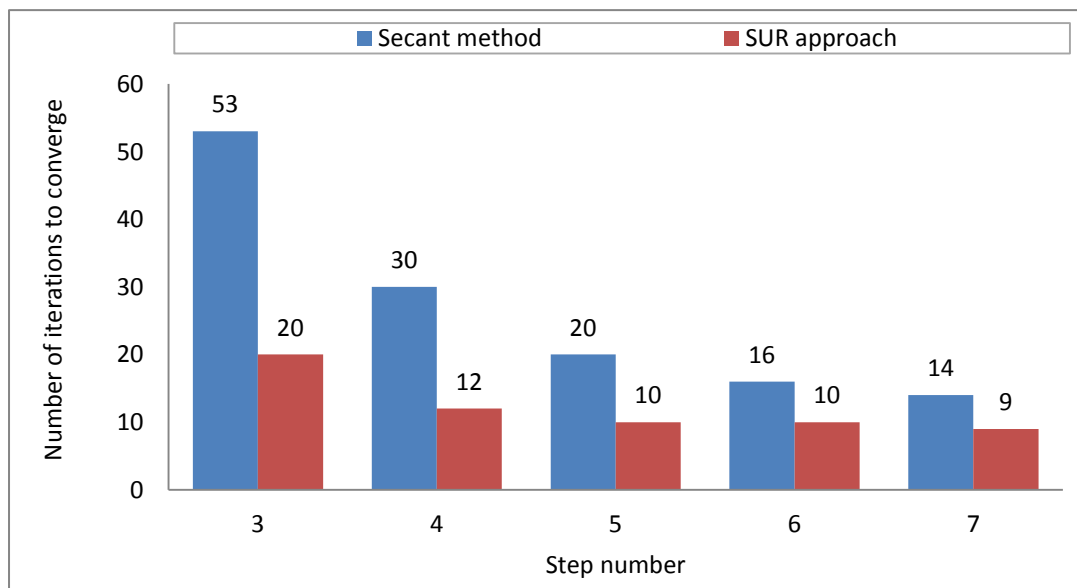


Figure 4.2: Number of iterations to achieve convergence for the most difficult increments of the 1D bar.

In Figure 4.3, the iterative change in the damage evolution parameter ( $\Delta r_p$ ) is plotted against the iteration number in semi-log space. It can be seen from this graph that, after a certain point,  $\Delta r_p$  exhibits a linear decay in semi-log space.

The observation that ‘ $\log \Delta r_p$ ’ reaches a linear decay line led to the development of an algorithm for the prediction of  $r_p$ , which was subsequently tested using the examples described Section 4.3.

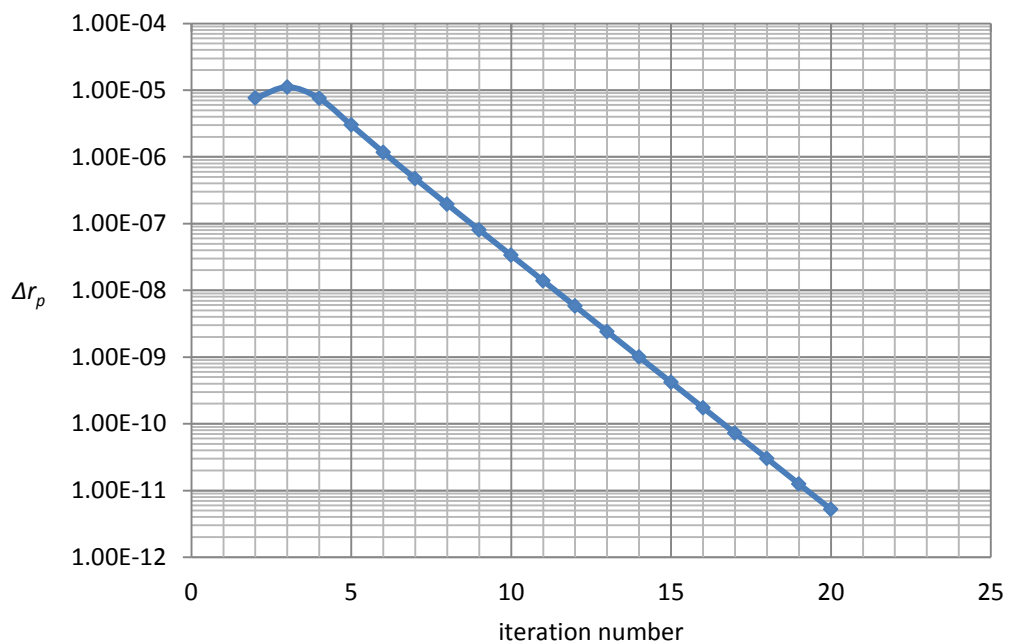


Figure 4.3: Relationship between number of iterations at the most difficult step (step No. 3) and the differences between damage evolution parameters for the 1D bar.

The predictive function is based on two main principles:

1. The relationship between the number of iterations ( $it$ ) within an increment and the iterative change of the damage evolution parameter ( $\Delta r_{p_i} = r_{p_i} - r_{p_{i-1}}$ ) decays linearly in semi-log space, once stable convergence has been achieved, as shown in Figure 4.3.

2. When the slope of the  $it$  vs  $(\log \Delta r_p)$  curve starts decreasing (see Figure 4.3), a trial prediction of the damage evolution parameter ( $r_{pp}$ ) can be computed using equation (4.4). Once the normalised difference between two consecutive predictions is less than 5%,  $r_p$  is set to the most recently computed trial value, i.e.  $r_p = r_{pp}$ .

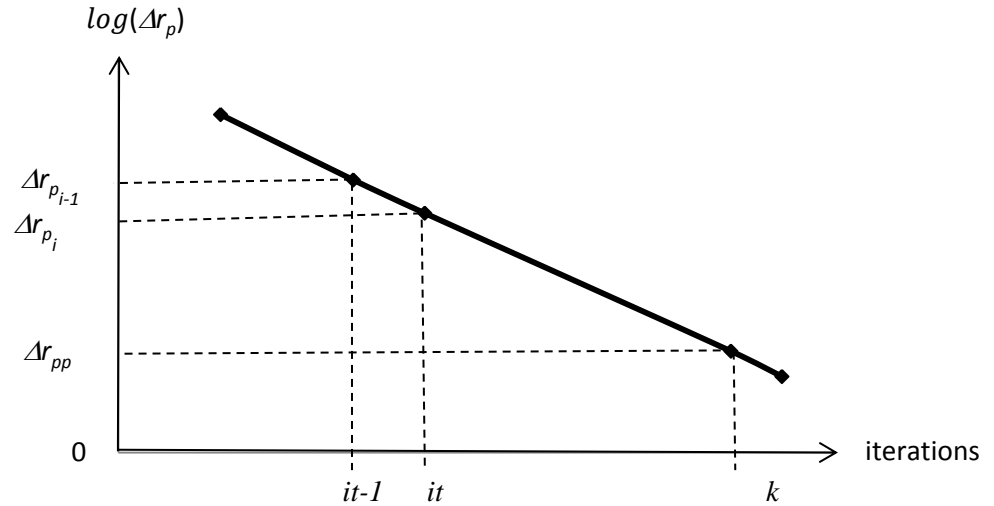


Figure 4.4: Relation between number of iterations and differences between damage evolution parameters within a time step.

Based on Figure 4.4, the following extrapolation can be obtained:

$$\frac{\log(\Delta r_{p_i}) - \log(\Delta r_{p_{i-1}})}{1} = \frac{\log(\Delta r_{pp}) - \log(\Delta r_{p_i})}{k - it} \quad (4.1)$$

Equation (4.1) can be simplified to:

$$\log(\Delta r_{pp}) = (k - it) \cdot [\log(\Delta r_{p_i}) - \log(\Delta r_{p_{i-1}})] + \log(\Delta r_{p_i})$$

$$\Delta r_{pp} = 10^{\log(\Delta r_{pp})} = 10^{(k-it)[\log(\Delta r_{p_i}) - \log(\Delta r_{p_{i-1}})] + \log(\Delta r_{p_i})}$$

Then the equation (4.1) becomes

$$\Delta r_{pp} = 10^{j \cdot b + a} \quad (4.2)$$

in which  $j = k - it$ ,  $b = \log(\Delta r_{p_i}) - \log(\Delta r_{p_{i-1}})$  and  $a = \log(\Delta r_{p_i})$ .

It follows that the predicted damage evolution parameter is;

$$r_{pp} = r_{p_i} + \sum_{j=1}^{\infty} \Delta r_{pp_j} \quad (4.3)$$

The summation in equation (4.3) may also be written as;

$$\sum_{j=1}^{\infty} \Delta r_{pp_j} = \frac{10^a (10^b - 10^{b\infty})}{1 - 10^b}$$

The prediction is only considered when  $\Delta r_p$  is reducing and this means that  $b$  always satisfies  $b < 0$ , and therefore  $10^{b\infty} = 0$ . The predictive damage evolution parameter  $r_{pp}$  can now be written:

$$r_{pp} = r_{p_{it}} + \frac{\Delta r_{p_i}^2}{\Delta r_{p_{i-1}} - \Delta r_{p_i}} \quad (4.4)$$

Table 4.1 summarises the steps involved in computing the  $r_p$  prediction.

Table 4.1: Predictive function algorithm.		
$r_{pp_i}$	if $\Delta r_{p_i} < \Delta r_{p_{i-1}}$	Compute 1 <sup>st</sup> $r_p$ prediction at $it$
$r_{pp_{i+1}}$	if $\Delta r_{p_{i+1}} < \Delta r_{p_i}$	Compute 2 <sup>nd</sup> $r_p$ prediction at $it+1$
$r_p = r_{pp_{i+1}}$	if $\frac{r_{pp_{i+1}} - r_{pp_i}}{r_{pp_{i+1}}} \leq 5\%$	Set $r_p$ value to $r_{pp_{i+1}}$ , if the second principal is satisfied

The predictive algorithm has been derived from the response of a 1D three element example and relies on the iterative solution reaching a point at which the change in the damage evolution parameter exhibits the semi-log decay shown in Figure 4.3 for all active damage zones. The point at which this semi-log decay occurs will be problem dependent and may be expected to be reached in fewer iterations in small 1D problems than in larger multi-element 2D and 3D cases. This issue is explored in the numerical implementation section of this chapter which assesses the performance of the predictive algorithm for range of multi-element 1D and 2D problems.

### 4.2.2 Fixing algorithm

An alternative acceleration technique, named the ‘fixing approach’, in which a two-stage algorithm is employed with the standard SUR approach, is now described. The philosophy behind this acceleration approach is that, since the majority of cracks will occur during the first few iterations of any load increment, the damage evolution parameter ( $r_p$ ) is allowed to be updated from the last converged increment in early ‘Stage-1 iterations’ and then it is fixed for the subsequent ‘Stage-2 iterations’, within each increment. However, in Stage-2 iterations, the effective damage evolution parameter  $r_{eff}$  is only updated when the value of  $r_{eff}$  exceeds the frozen scalar of  $r_p$ .  $it_{fix}$  is used to denote the limit number of iterations in Stage-1. It should be mentioned that quadratic convergence is achieved once  $it > it_{fix}$ .

Two different values of  $it_{fix}$  were considered in the study, with a comparison being made between solutions with  $it_{fix}=3$  and  $it_{fix}=5$ .

### 4.2.3 Slack tolerance technique

In the incremental-iterative solution procedure, the total load/displacement is divided into small increments and each increment is applied individually. In order to achieve the equilibrium at the end of each step, iterations are performed within each load/displacement increment. Convergence is assessed using the L2 norms of the out-of-balance force vector and the iterative displacement vector (Becker, 2004).

Convergence is achieved, if both of iterative displacement and out-of-balance force norms are smaller than a specified tolerance. When convergence is not achieved, a correction to the displacement vector is required, in which the residual force is used to obtain a correction to the displacement. The correction procedure is repeated until the both norms became below a certain tolerance. The user of the FE code normally sets the convergence tolerance, but it is not generally recommended to be less than 1% (Bathe, 2006). The standard tolerance of ‘0.1% or 0.0001%’ employed with the SUR technique to-date is considerably smaller than this recommended value and therefore a third SUR option was devised that involves switching to slacker tolerance of 1% when ‘difficult increments’ are encountered. These are defined as increments in which the number of iterations exceeds 5 iterations ( $it > 5$ ) with the standard SUR solution. The tolerance reverts to ‘0.1% or 0.0001%’ for subsequent increments.

### 4.3 Numerical implementation

Four examples are used in this section to investigate the benefit of implementing the proposed acceleration algorithms for improving the convergence properties of the standard SUR method when analysing quasi-brittle structures. The examples are the same as those used in the previous chapter to enable a direct comparison.

Table 4.2 provides a summary of the material properties used in these examples. The four examples were analysed using the following four approaches:

- Smooth unloading reloading (SUR) approach.
- Predictive-SUR approach.
- Fixing approach with  $it_{fix}=3$  and 5 in Stage-1 iterations.
- Slack tolerance technique.

The solution characteristics of the examples are presented by showing the number of iterations required to achieve convergence for selected ‘difficult increments’. Indeed, the most difficult increments frequently coincided with the crack initiation or started in the initial stages of crack propagation (Hellweg and Crisfield, 1998). Furthermore, the total number of iterations required for each solution for all examples is presented.

In the first two examples, the convergence history for SUR, predictive-SUR and fixing solutions is plotted. The information provided includes the out of balance force norm at the end of each load increment. The out of balance force norm history for a selected increment is also given.

Table 4.2: Material properties and convergence tolerances.							
Example No.	$E_c$ (GPa)	$E_s$ (GPa)	$\nu$	$f_t$ (MPa)	$G_f$ (N/mm)	$\Psi_f$	$\Psi_d$
1	20	-	0.20	2.5	0.10	$10^{-3}$ & $10^{-6}$	$10^{-3}$ & $10^{-6}$
2	20	-	0.20	2.5	0.10	$10^{-3}$ & $10^{-6}$	$10^{-3}$ & $10^{-6}$
3	42	200	0.20	2.5	0.10	$10^{-3}$	$10^{-3}$
4	20	-	0.20	2.5	0.10	$10^{-3}$	$10^{-3}$

### Example 4.3.1: One-dimensional tensile test

The first example is the 1D tensile test specimen shown in Figure 4.1, which was used to explain the theory of the proposed predictive-SUR approach. In this example, 40 and 100 increments were used in the analyses with convergence tolerances equal to  $10^{-3}$  and  $10^{-6}$ .

The equilibrium paths for the standard SUR and SUR with acceleration approaches are shown in Figures 4.5 and 4.6. Moreover, Figures 4.7 to 4.10 present the number of iterations to achieve convergence for the most difficult increments. Also, the total number of iterations required for completing the analysis for each approach is given in Figures 4.11 and 4.12.

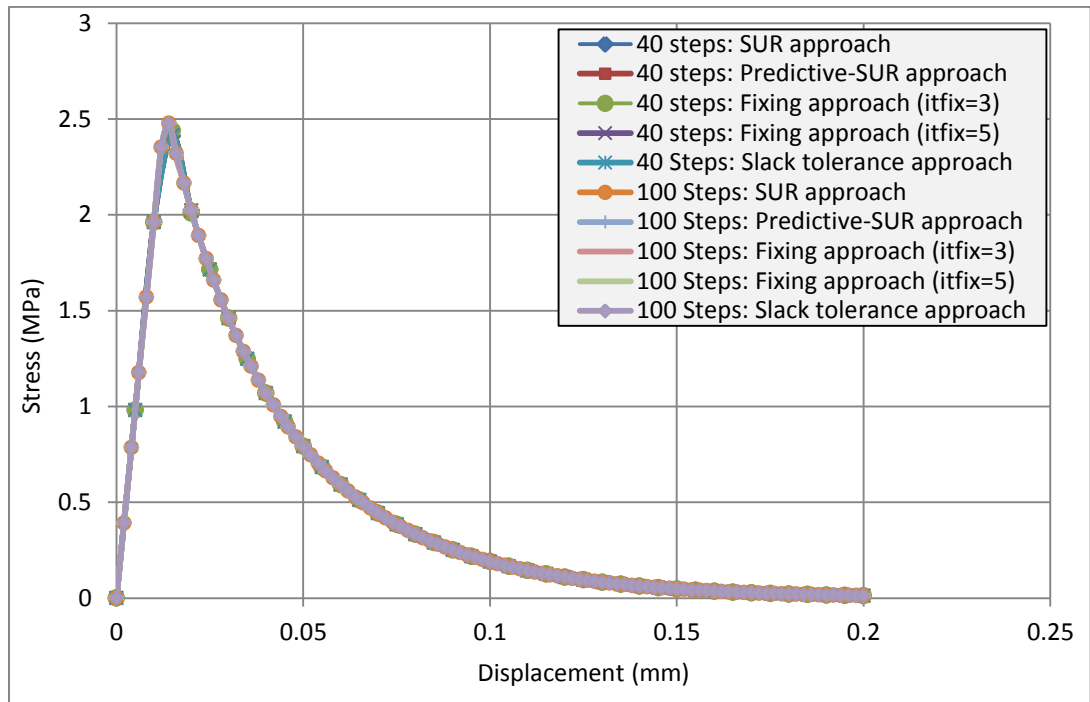


Figure 4.5: Numerical displacement-stress responses for 1D example with  $10^{-3}$  convergence tolerance.

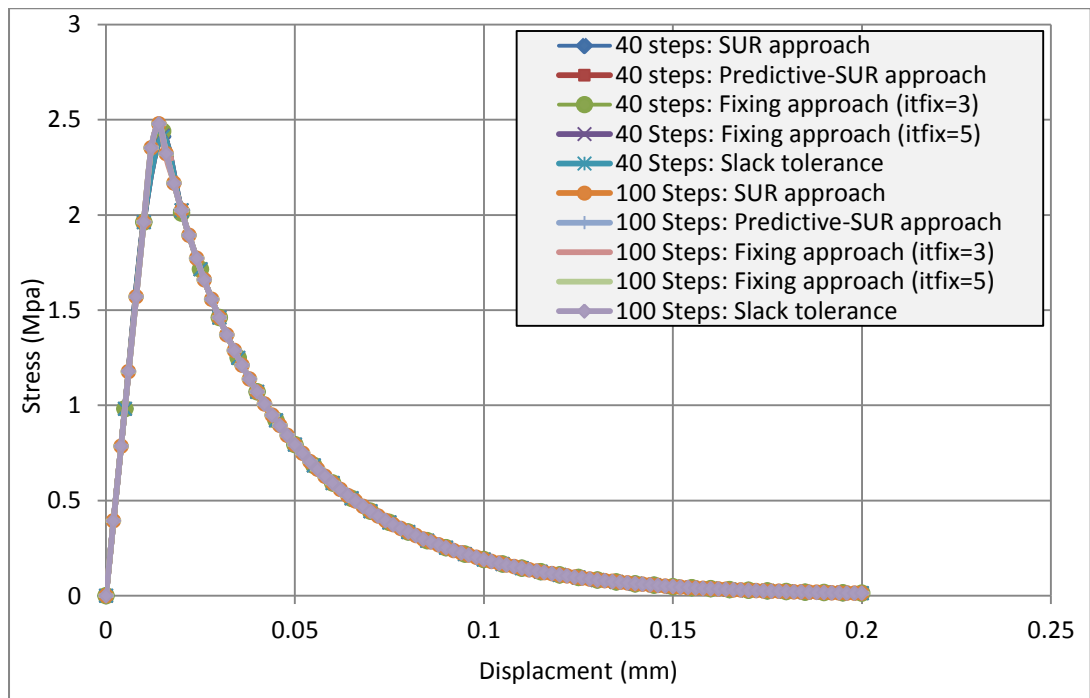


Figure 4.6: Numerical displacement-stress responses for 1D example with  $10^{-6}$  convergence tolerance.

The resulting stress-displacement responses from the various analyses are indistinguishable from each other, as can be seen in Figures 4.5 and 4.6.

In all sets of analyses, results showed that the three acceleration techniques achieved converged solutions in fewer iterations than the standard SUR solution (Figures 4.7 to 4.10). Furthermore, the ‘fixing algorithm’, with 3 iterations in Stage-1, was on average a little more efficient than the others, as can be seen in Figures 4.11 and 4.12.

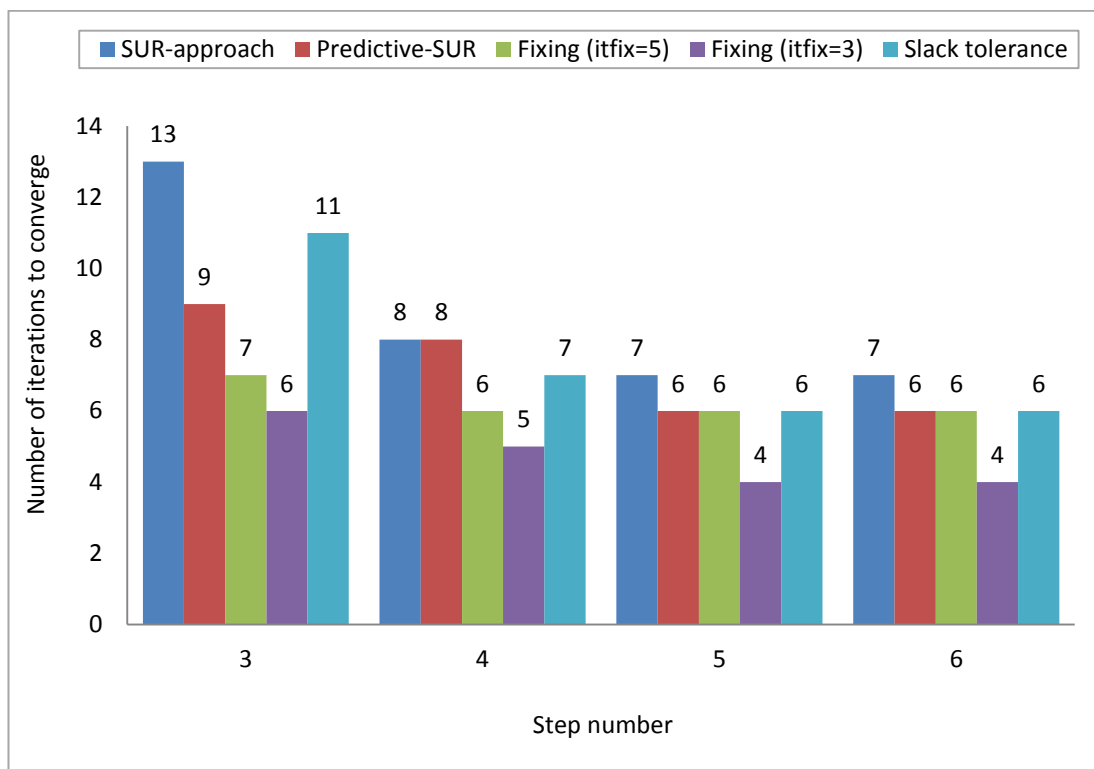


Figure 4.7: Number of iterations to achieve convergence for the most difficult increments for the analysis with 40 steps (convergence tolerance =  $10^{-3}$ ).

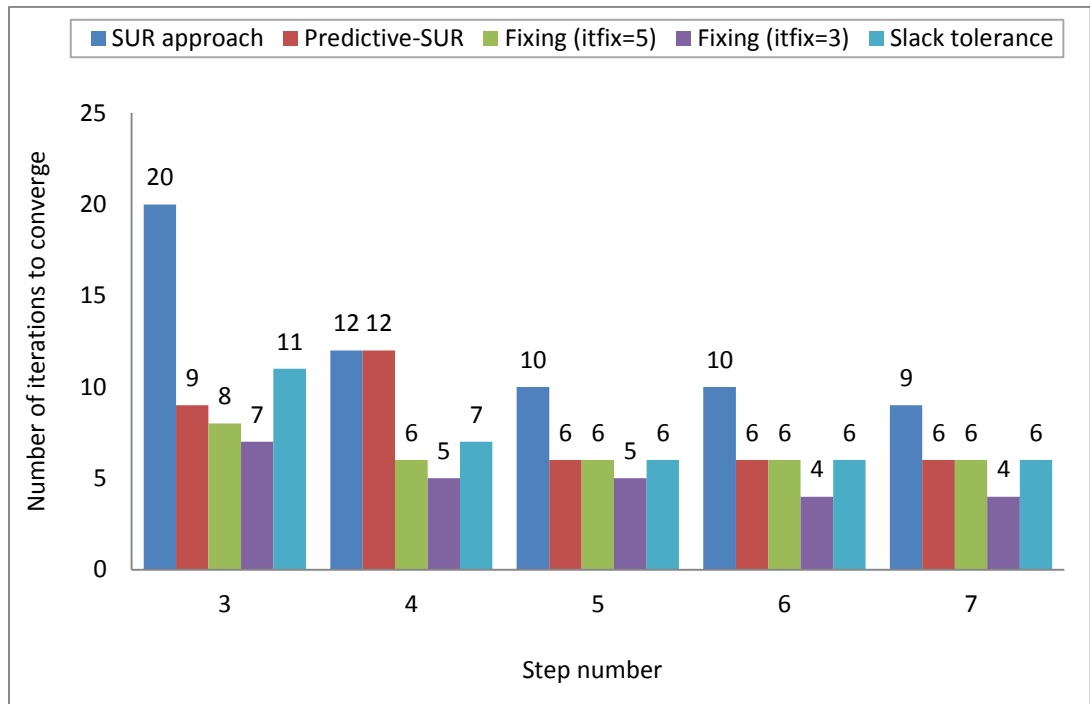


Figure 4.8: Number of iterations to achieve convergence for the most difficult increments for the analysis with 40 steps (convergence tolerance =  $10^{-6}$ ).

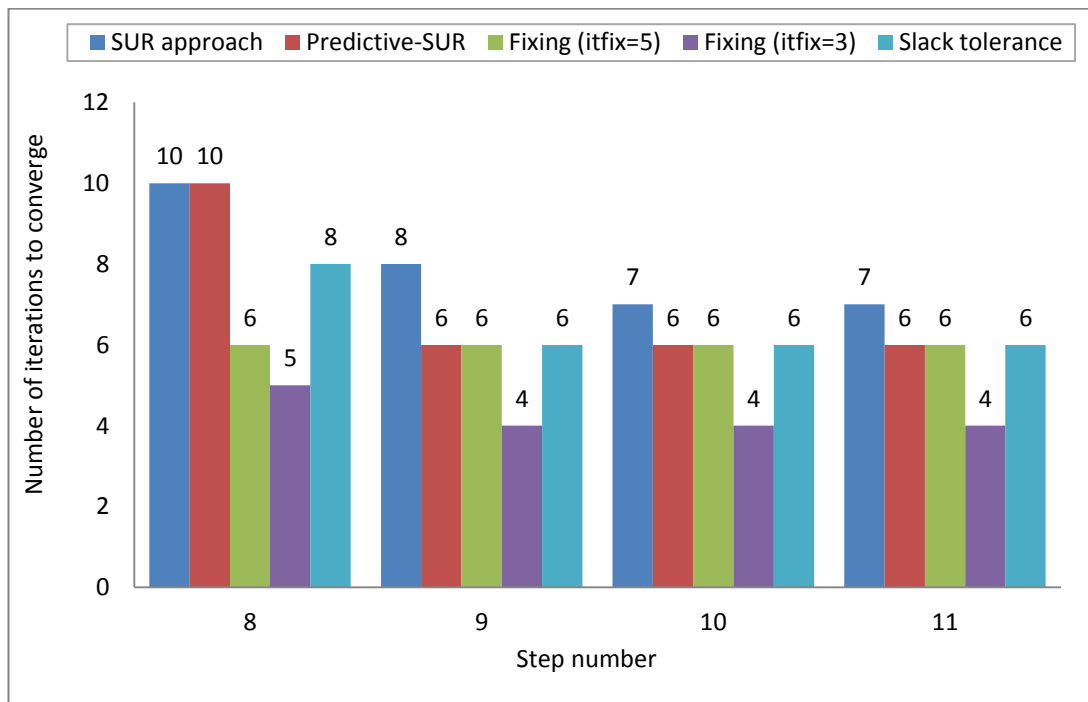


Figure 4.9: Number of iterations to achieve convergence for the most difficult increments for the analysis with 100 steps (convergence tolerance =  $10^{-3}$ ).

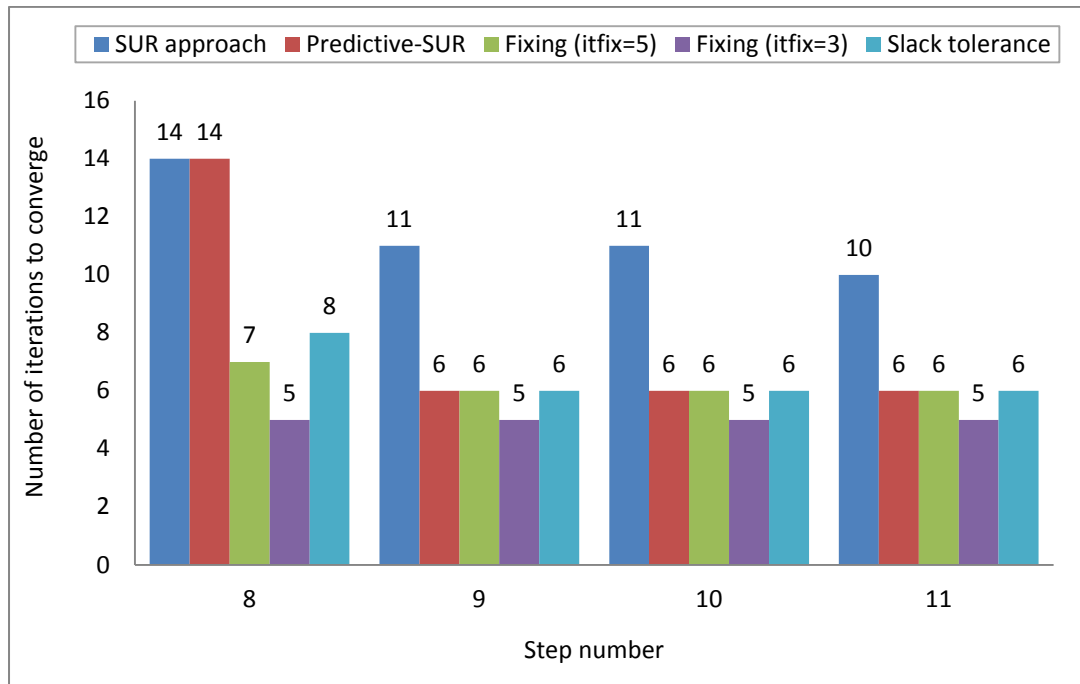


Figure 4.10: Number of iterations to achieve convergence for the most difficult increments for the analysis with 100 steps (convergence tolerance= $10^{-6}$ ).

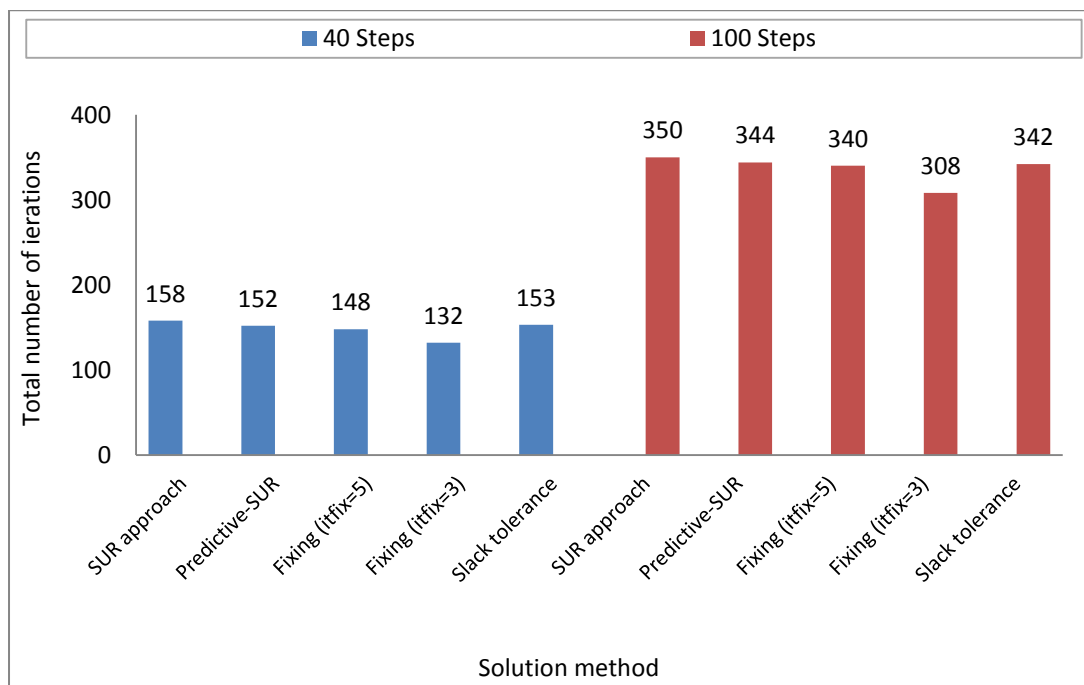


Figure 4.11: Total number of iterations that needed for each solution in the 1D example using convergence tolerance  $10^{-3}$ .

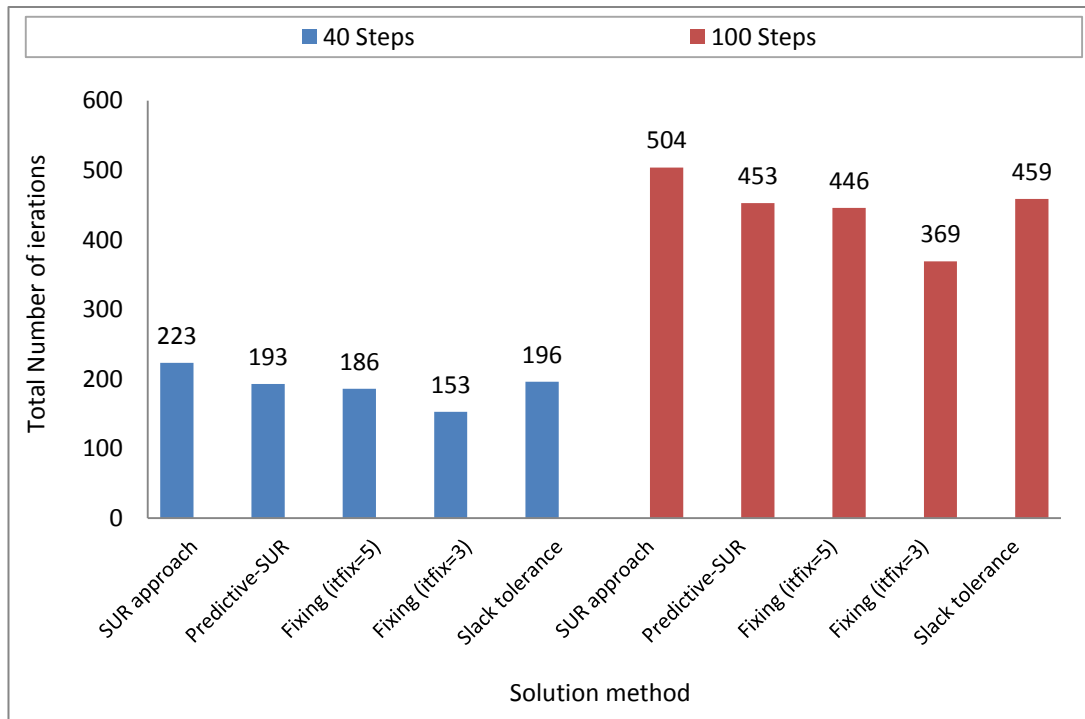


Figure 4.12: Total number of iterations that needed for each solution in the 1D example with convergence tolerance of  $10^{-6}$ .

The convergence history for the analysis with 40 and 100 steps is shown in Figures 4.13 and 4.15, respectively. Figures 4.14 and 4.16 show how the convergence progress of the SUR, predictive-SUR and fixing approaches for steps which had relatively the biggest reduction of iterations that required to achieve convergence, in which step number 3 was in the analysis with 40 steps, and step number 9 for the analysis with 100 increments

The convergence curves shown in Figures 4.14 and 4.16 indicate that the convergence rate of the standard SUR method is improved by using the accelerating algorithms.

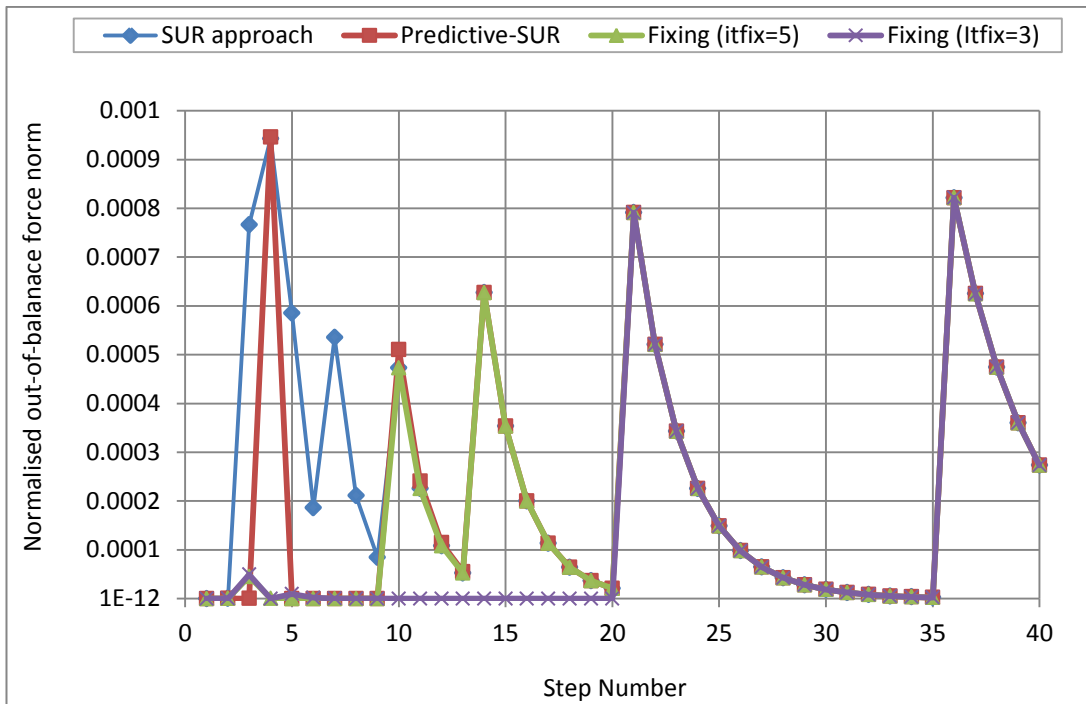


Figure 4.13: Out of balance force norm at the end of each increment for the analysis with 40 steps and convergence tolerance =  $10^{-3}$ .

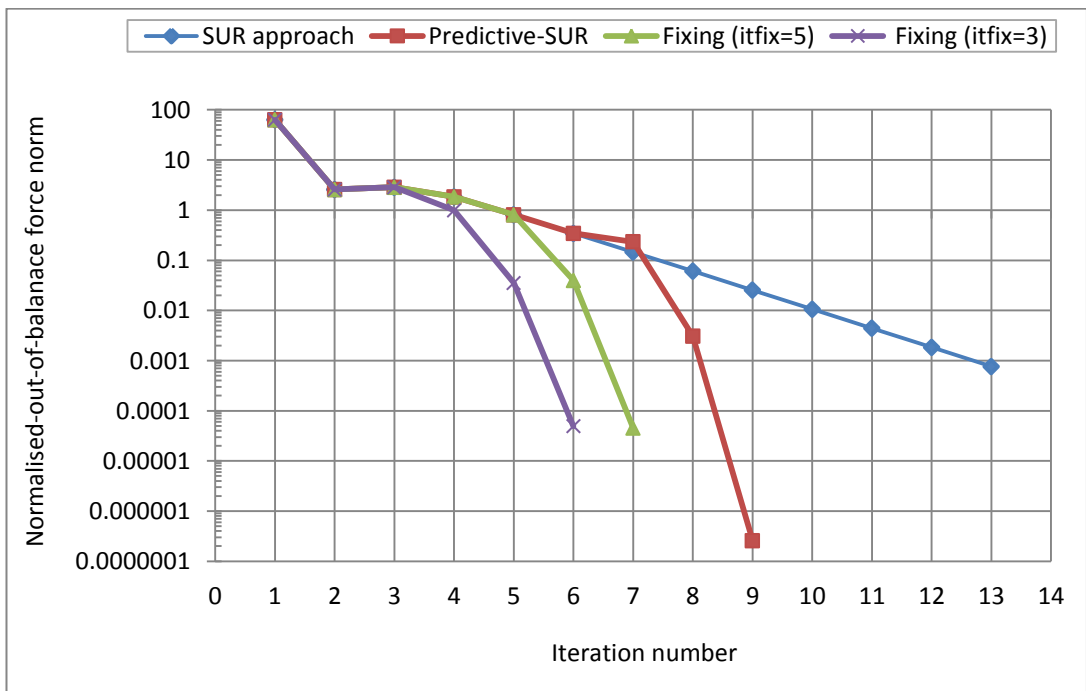


Figure 4.14: Out of balance force norm history for increment number 3 with 40 steps and convergence tolerance =  $10^{-3}$ .

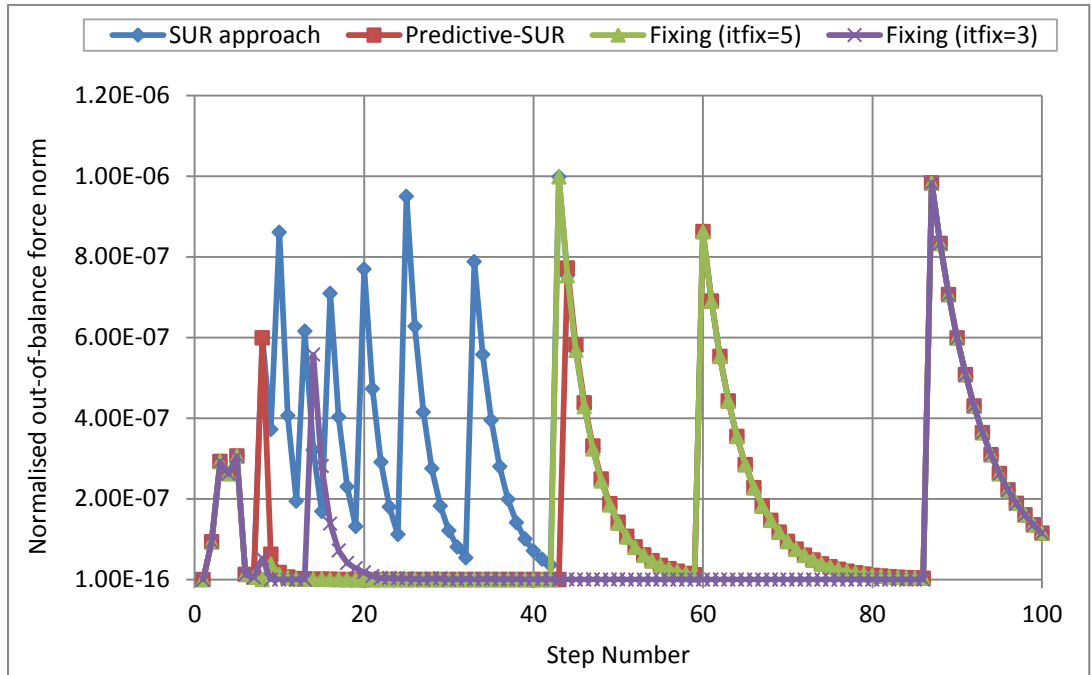


Figure 4.15: Out of balance force norm at the end of each increment for the analysis with 100 steps and convergence tolerance =  $10^{-6}$ .

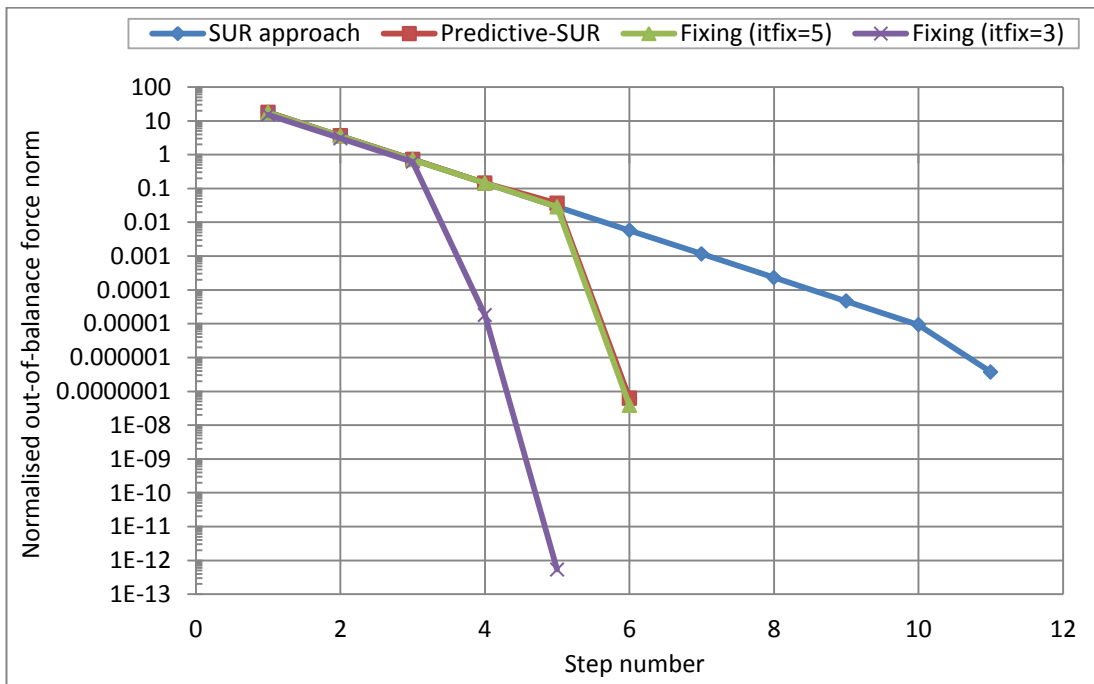


Figure 4.16: Out of balance force norm history for increment number 9 with 100 steps and convergence tolerance= $10^{-6}$ .

### Example 4.3.2: Two-dimensional plane stress specimen

An idealised 2D structure, shown in Figure 4.17a, was analysed using the damage model with various acceleration techniques. The analyses were carried out using two different prescribed displacement increments comprising 50 or 100 even steps. Also, two convergence tolerances of  $10^{-3}$  and  $10^{-6}$  were used for the analysis.

The stress-displacement responses from analyses using the standard SUR approach and acceleration techniques are shown in Figures 4.18 and 4.19. A damage contour plot at last displacement increment is given in Figure 4.20. Furthermore, the number of iterations needed to achieve convergence at the most difficult increments for all solutions are shown in Figures 4.21 to 4.24.

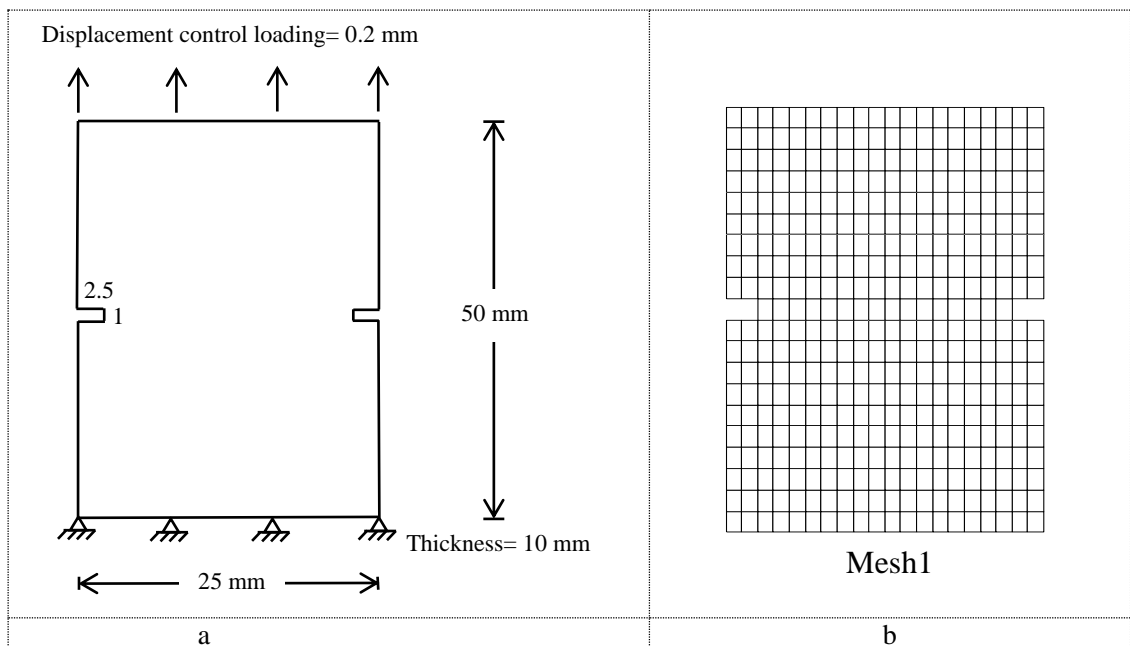


Figure 4.17: (a) 2D notched plane stress, (b) finite element Mesh1.

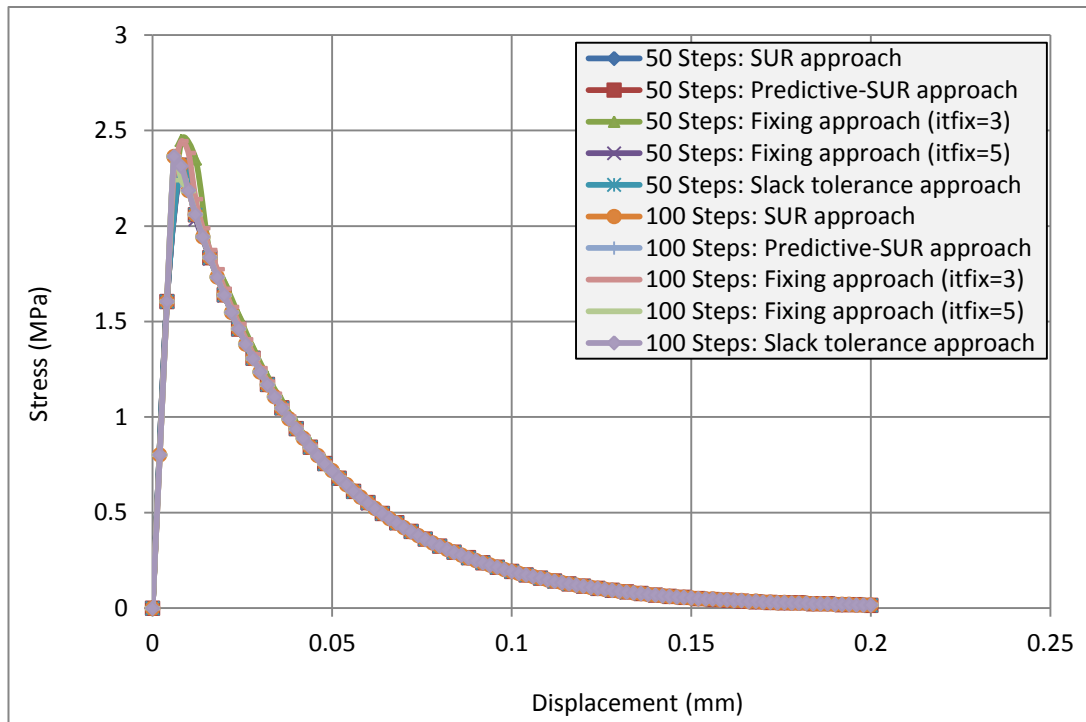


Figure 4.18: Displacement-Stress relationship for 2D plane stress specimen (convergence tolerance =  $10^{-3}$ ).

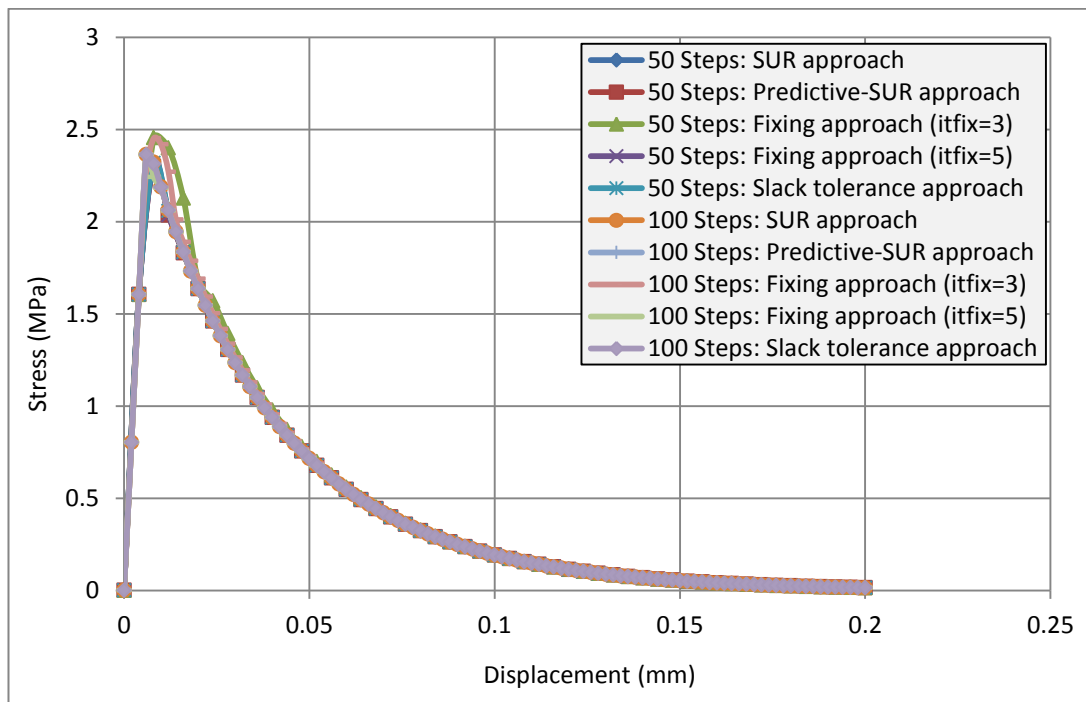


Figure 4.19: Displacement-Stress relationship for 2D plane stress specimen (convergence tolerance =  $10^{-6}$ ).

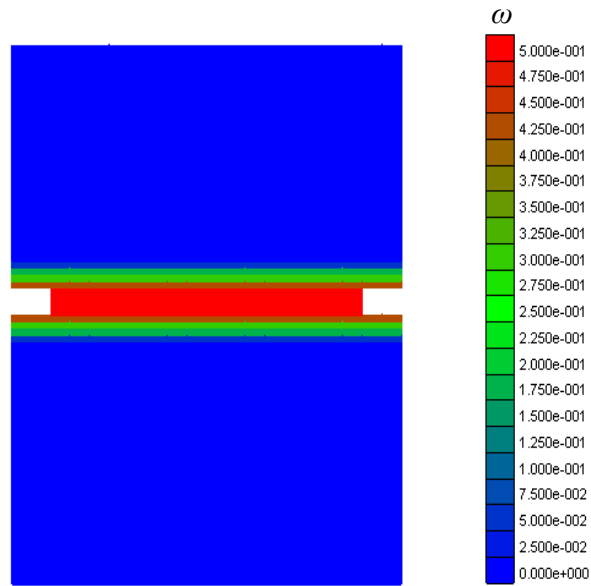


Figure 4.20: Damage contour plot at last displacement increment.

The complete stress-displacement responses obtained by predictive-SUR, fixing ( $it_{fix}=5$ ) and slack tolerance techniques are almost identical with the standard SUR response with both 50 and 100 steps, as illustrated in Figures 4.18 and 4.19. However, results obtained from the fixing approach in which  $it_{fix}=3$  show a small drift from the standard SUR response curve, but the discrepancy is relatively insignificant for both cases.

In this example, the crack was established in a single step or increment, i.e. increment 2 for the 50 step solution and increment 4 for the 100 step solution. When this occurs, overall number of iterations saved by using the acceleration approaches is insignificant when using  $\Psi_{f/d}=10^{-3}$ , but is noticeable with using  $\Psi_{f/d} = 10^{-6}$ , as can be seen in Figures 4.25 and 4.26.

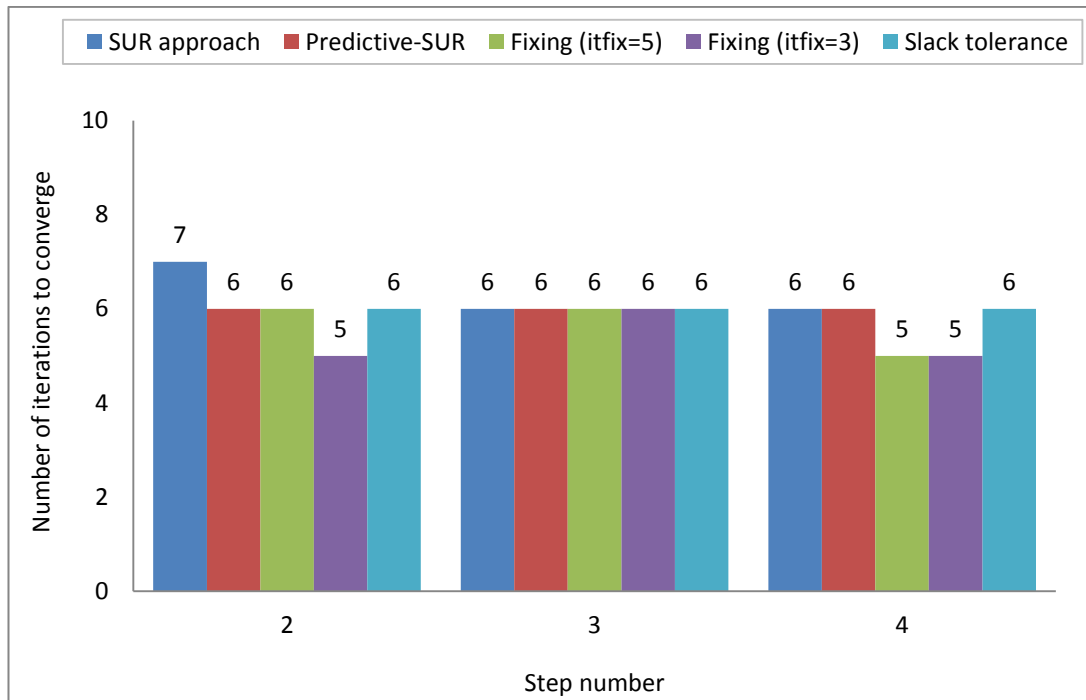


Figure 4.21: Number of iterations to achieve convergence for the most difficult increments for the analysis with 50 increments and convergence tolerance= $10^{-3}$ .

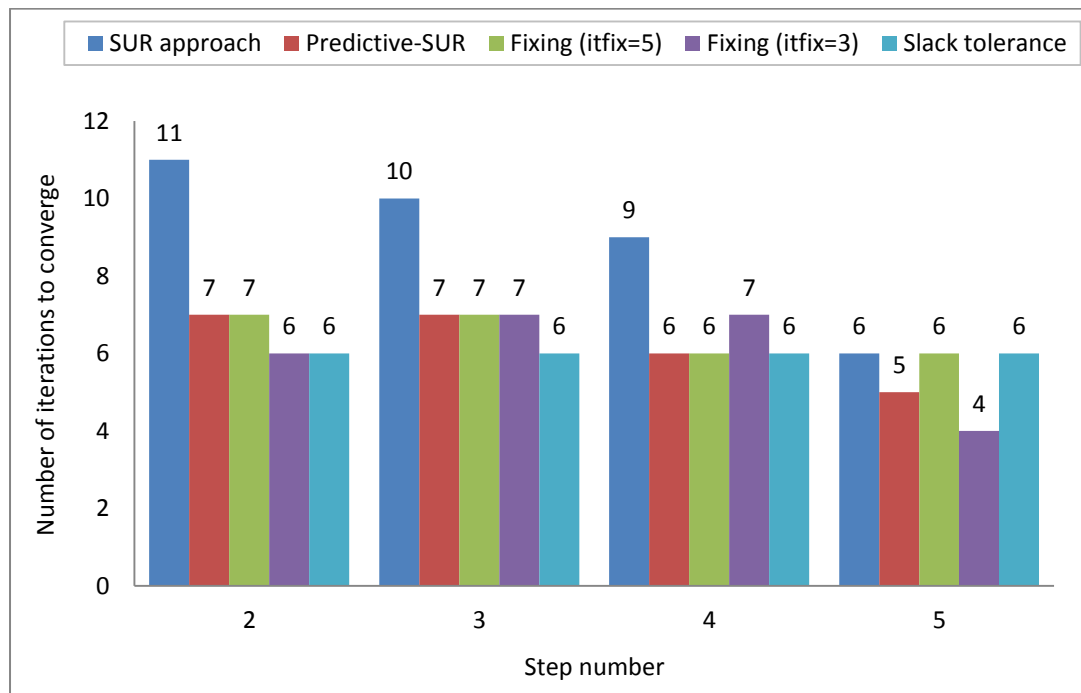


Figure 4.22: Number of iterations to achieve convergence for the most difficult increments for the analysis with 50 increments and convergence tolerance= $10^{-6}$ .

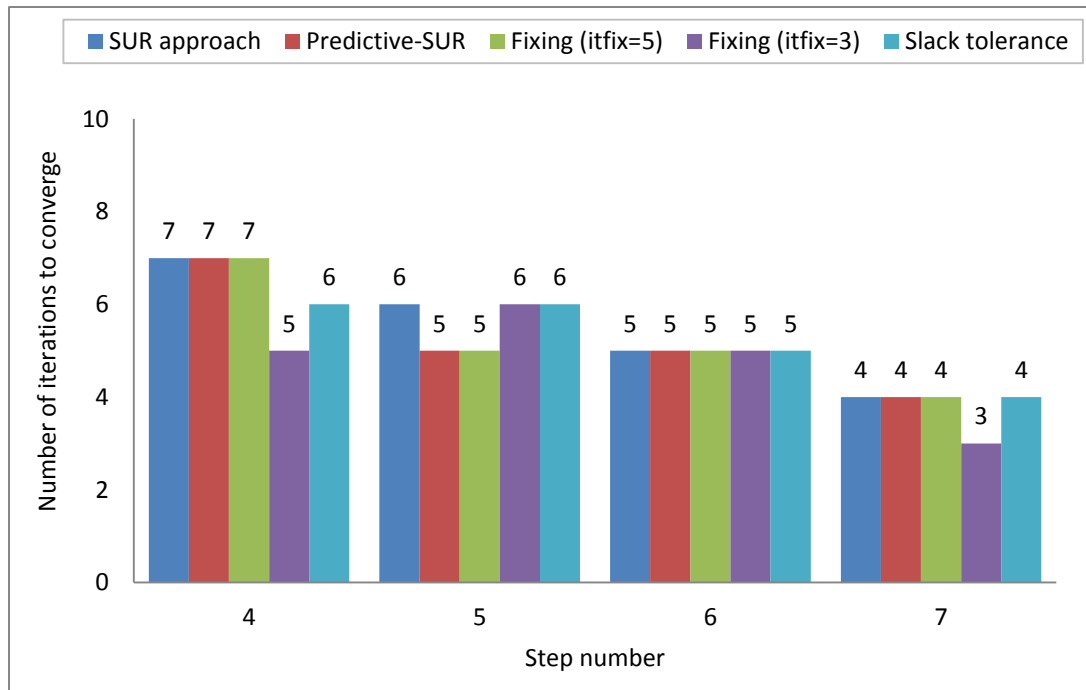


Figure 4.23: Number of iterations to achieve convergence for the most difficult increments for the analysis with 100 increments and convergence tolerance= $10^{-3}$ .

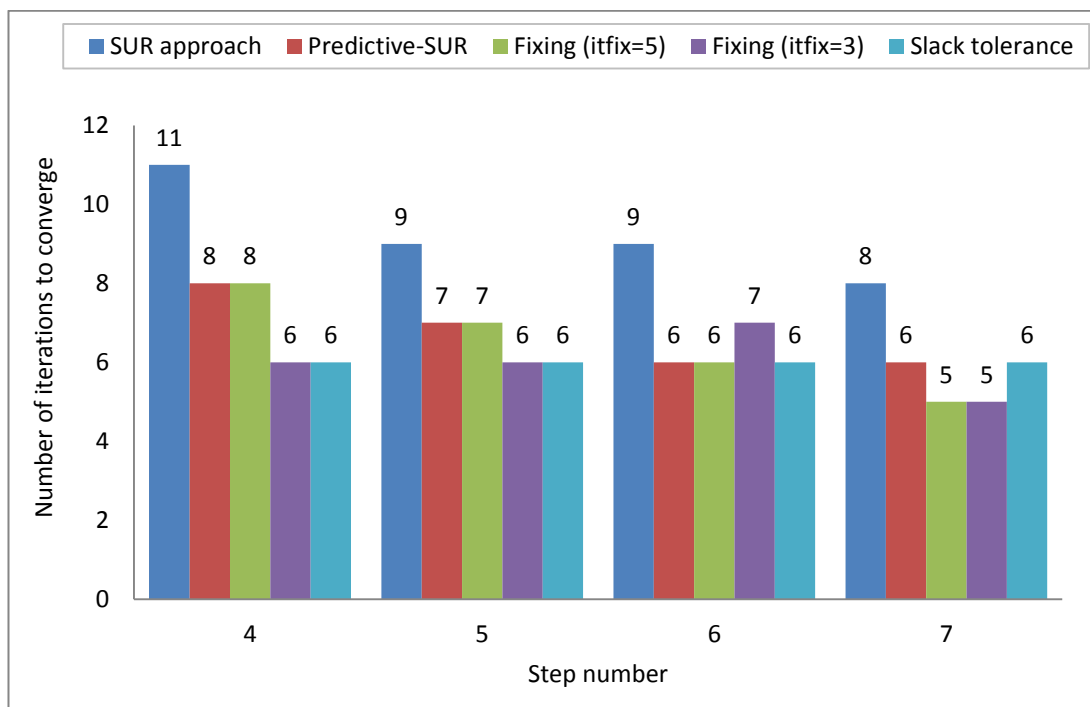


Figure 4.24: Number of iterations to achieve convergence for the most difficult increments for the analysis with 100 increments and convergence tolerance= $10^{-6}$ .

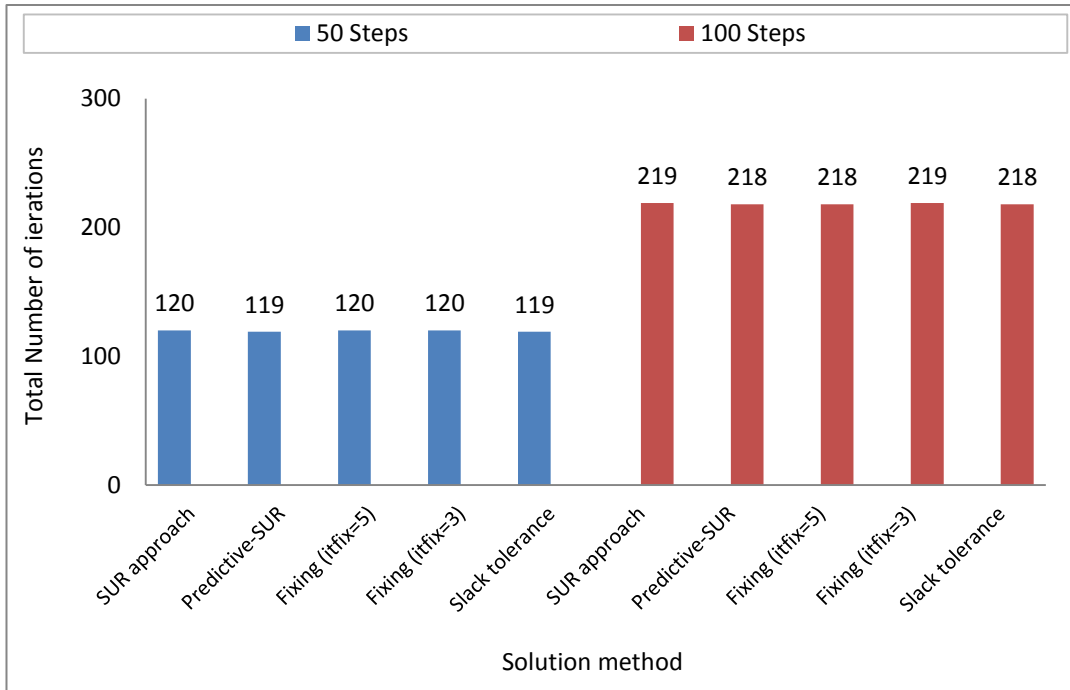


Figure 4.25: Total number of iterations that needed for each solution using convergence tolerance =  $10^{-3}$ .

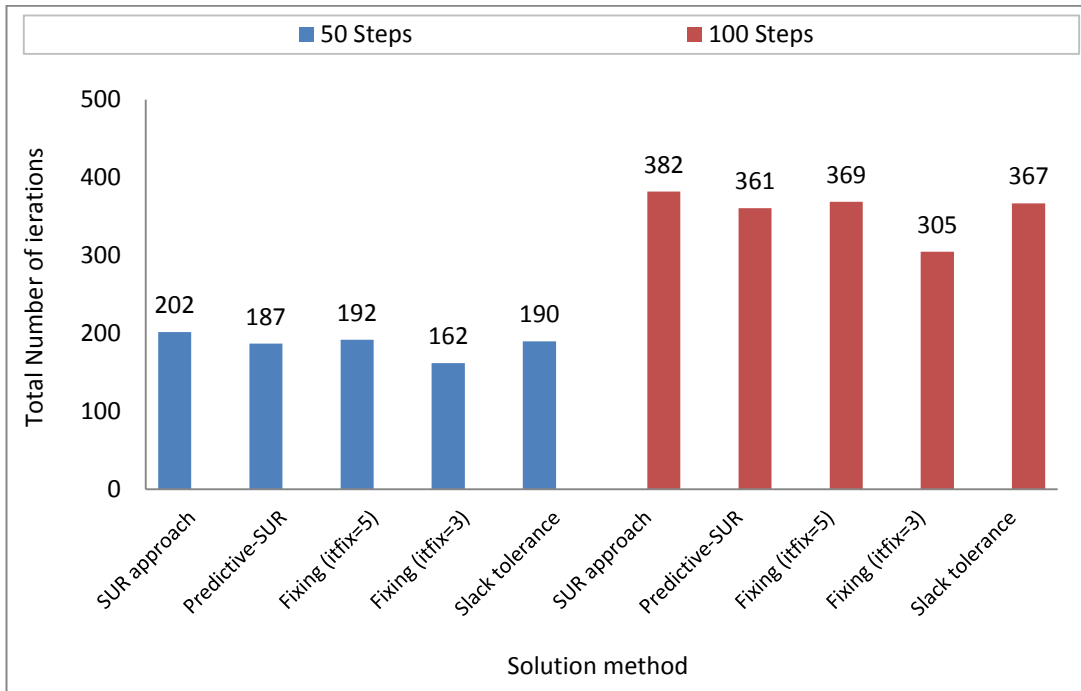


Figure 4.26: Total number of iterations that needed for each solution using convergence tolerance =  $10^{-6}$ .

**Example 4.3.3: Reinforced concrete prism**

The concrete prism shown in Figure 4.27 was reinforced with a single central reinforcement bar. The analysis was carried out with 50 and 100 steps to reach a displacement of 1mm at the load position.

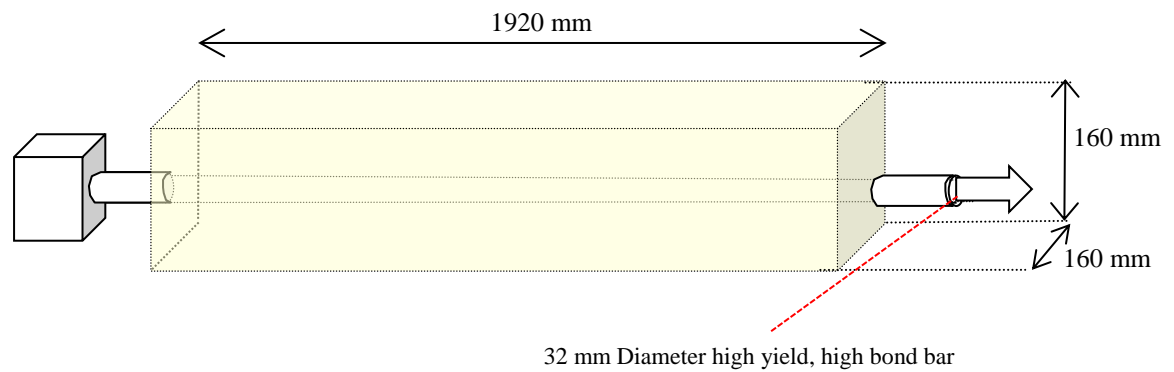


Figure 4.27: RC prism dimensions.

Figure 4.28 presents stress-displacement responses for both sets of the analyses. Again, the results of the standard SUR solution and the three acceleration techniques solutions are indistinguishable from each other.

As with other examples, it can be seen from the bar charts in Figures 4.29 and 4.30 that there was a dramatic decrease in the number of iterations required to achieve convergence for the SUR solution when any of the proposed acceleration techniques was employed. Thus, the efficiency of the proposed acceleration approaches is again evident.

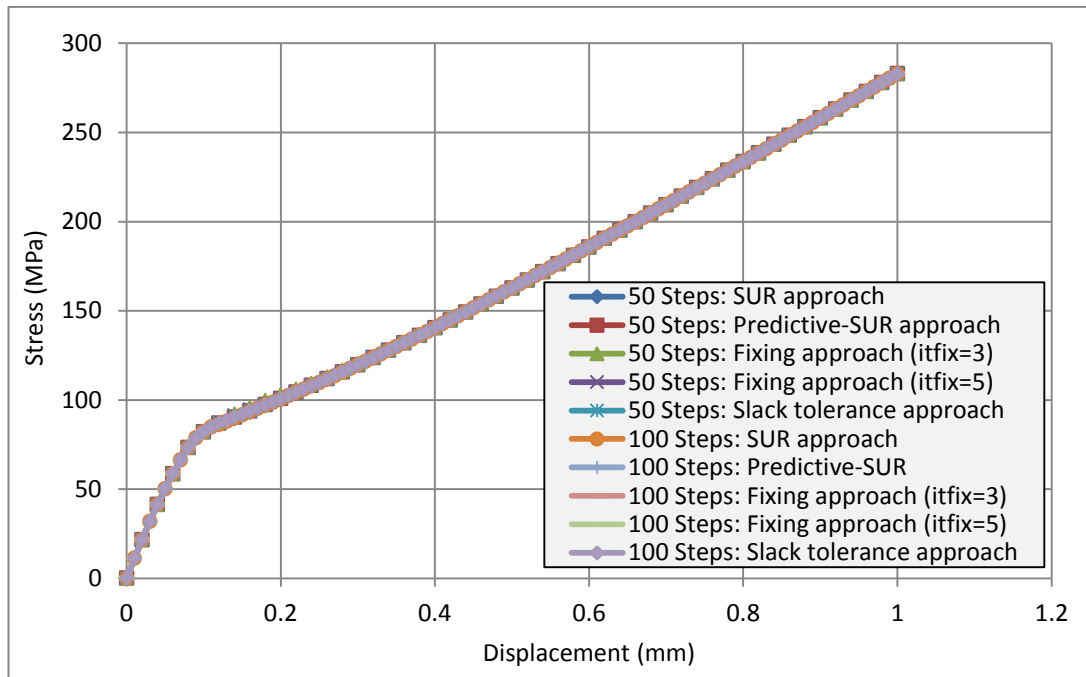


Figure 4.28: Load-displacement responses of RC prism.

The other main observation from these results is that, overall, the SUR predictive, fixing and slack tolerance solutions all require fewer iterations than the standard SUR method. However, there are single increments for which the basic SUR solution uses fewer iterations than the acceleration solutions. This is most evident in steps which follow-on from a previous step in which the predictive/fixing/slack tolerance algorithms gave a very significant reduction in iterations (e.g. see steps 6 and 7 in Figure 4.29). This occurred because the cracking was more distributed than in the plain concrete examples. It is believed that temporarily freezing  $r_p$ , whether at a predicted value in the predictive-SUR approach or at the fixed value in the fixing approach, causes the evolution of some local damage to be spread over 2 or 3 steps, rather over a single step.

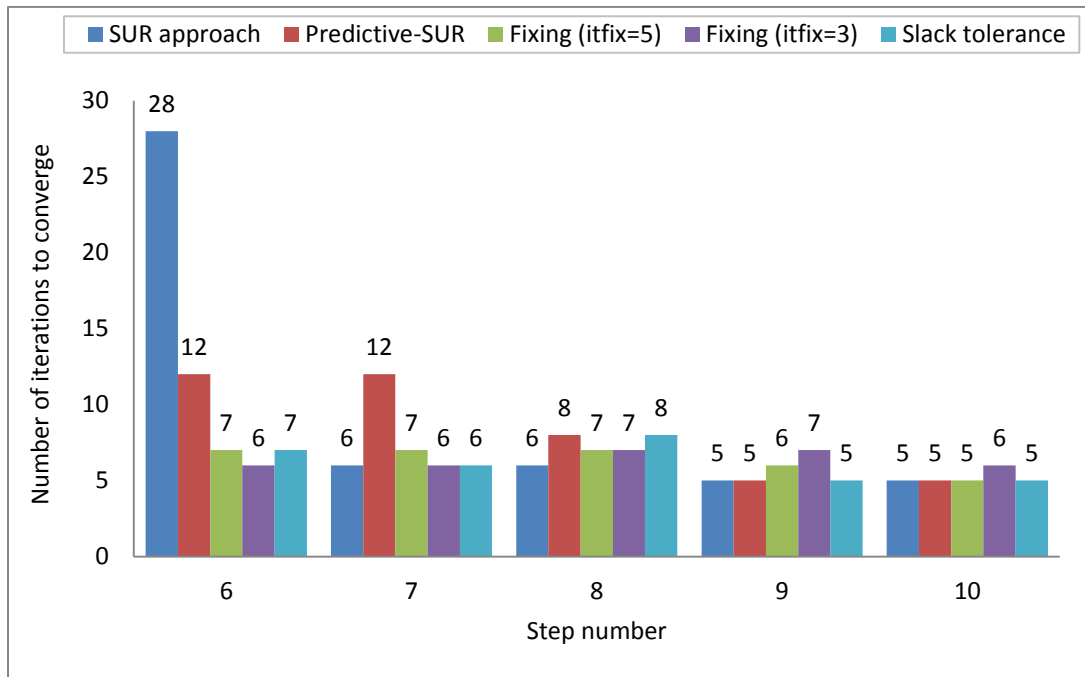


Figure 4.29: Number of iterations to achieve convergence for the most difficult increments of RC prism with 50 increments.

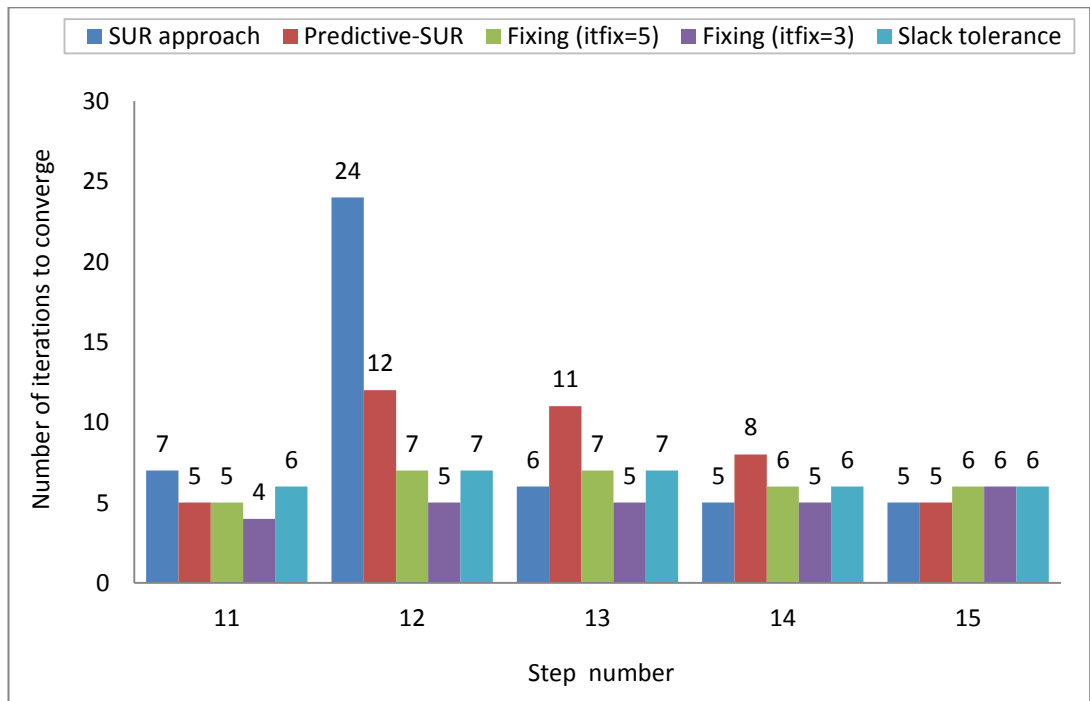


Figure 4.30: Number of iterations to achieve convergence for the most difficult increments of RC prism with 100 increments.

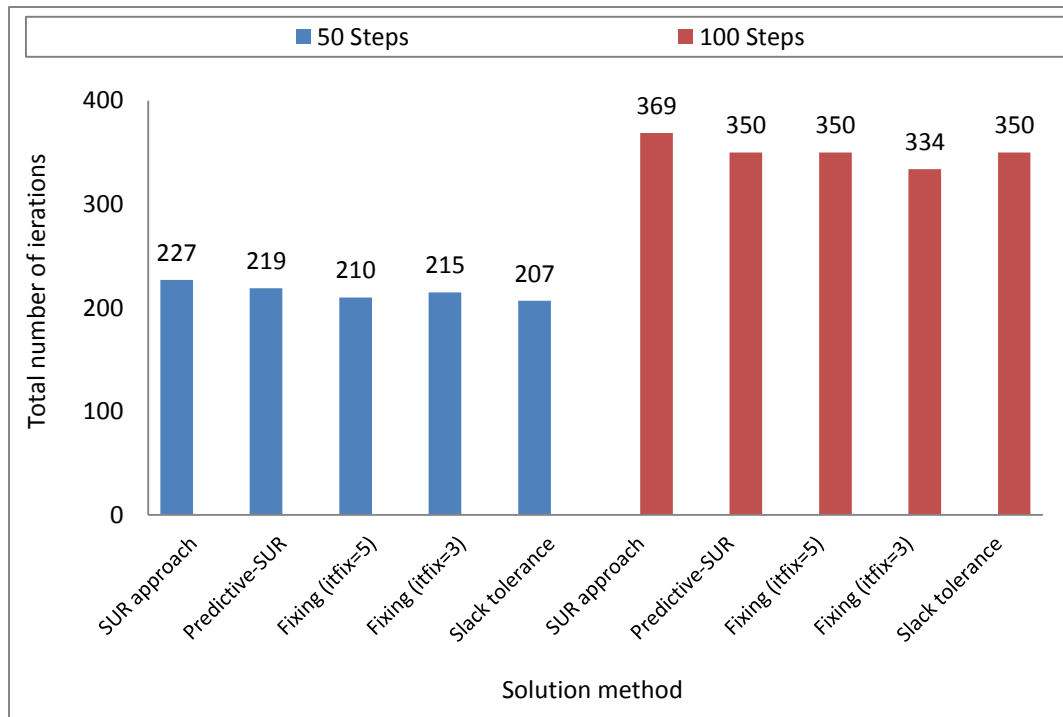


Figure 4.31: Total number of iterations that needed for each solution in the RC prism example.

#### Example 4.3.4: 2D double notched example.

The last example is a 2D double notched specimen loaded by a combination of shear and vertical tensile loads, as illustrated in Figure 4.32. The analyses were undertaken using 40 and 100 prescribed displacement increments.

The displacement versus vertical stress responses from the analyses using the standard SUR approach and the predictive-SUR, as well as the fixing and slack tolerance approaches are almost identical as shown in Figure 4.33. Moreover, the damage contour plot at the final displacement increment is depicted in Figure 4.34.

Vertical displacement control loading =0.15 mm, and 0.25 mm horizontally.

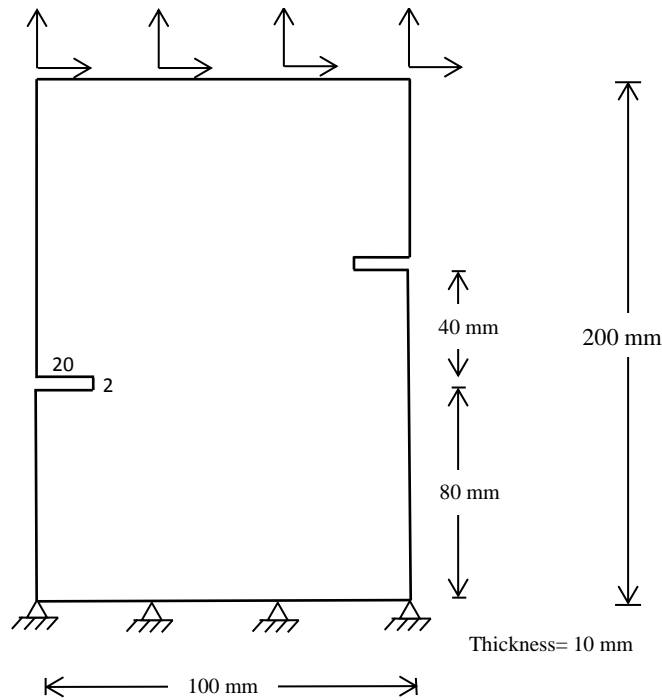


Figure 4.32: Geometry of the 2D double notched specimen.

Without doubt, using the proposed acceleration algorithms can give a noticeable reduction in the total number of iterations relative to those required by the basic SUR solution, as illustrated in Figure 4.37. Indeed, in some cases, implementing acceleration approaches can reduce the required number of iterations by more than 50 % at most difficult increments e.g. see step number 5 and 6 in Figure 4.35. As in example 1, the fixing approach with  $it_{fix}=3$  gave the greatest reduction in iterations among the other acceleration techniques.

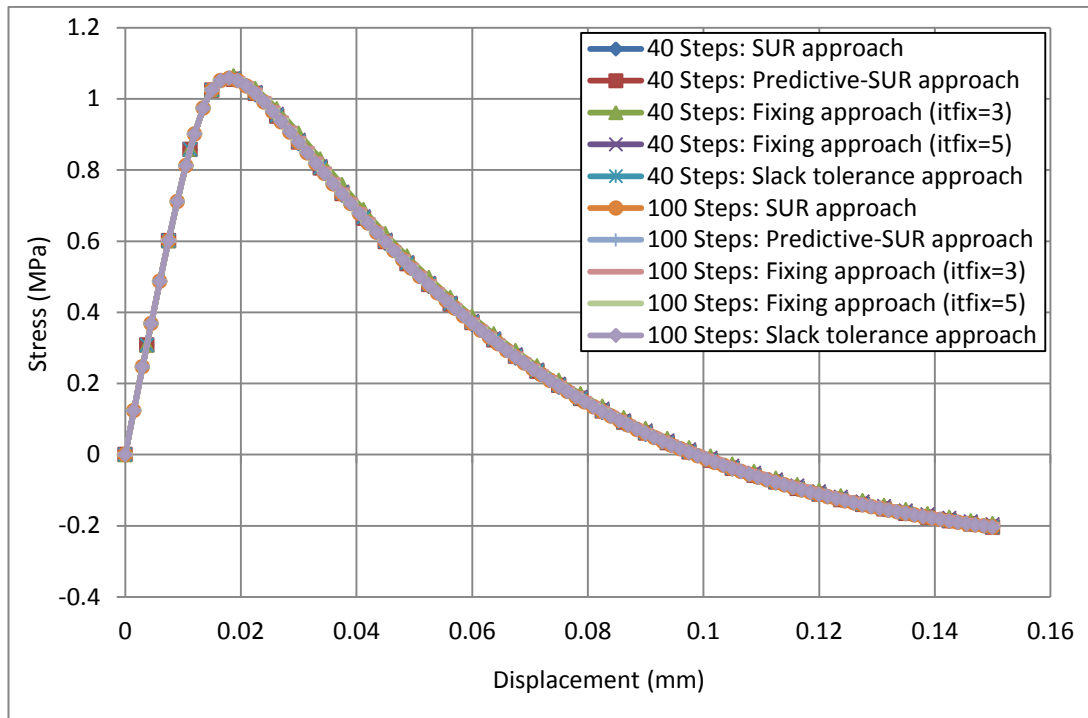


Figure 4.33: Numerical displacement and vertical stress responses 2D double notched specimen.

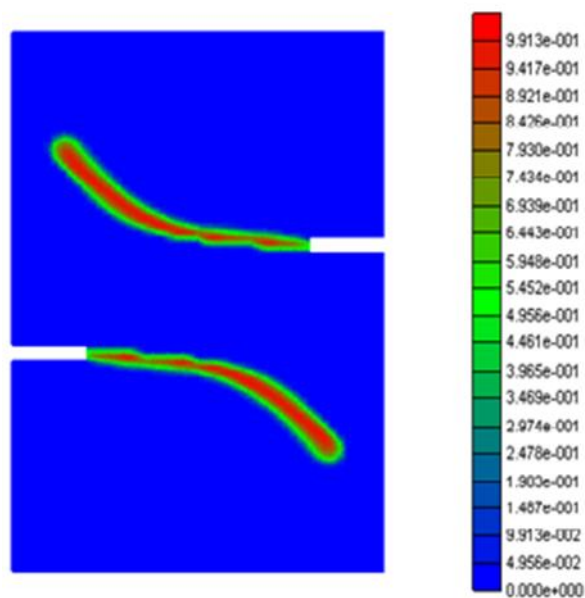


Figure 4.34: Damage indicator contour plot at last displacement increment.

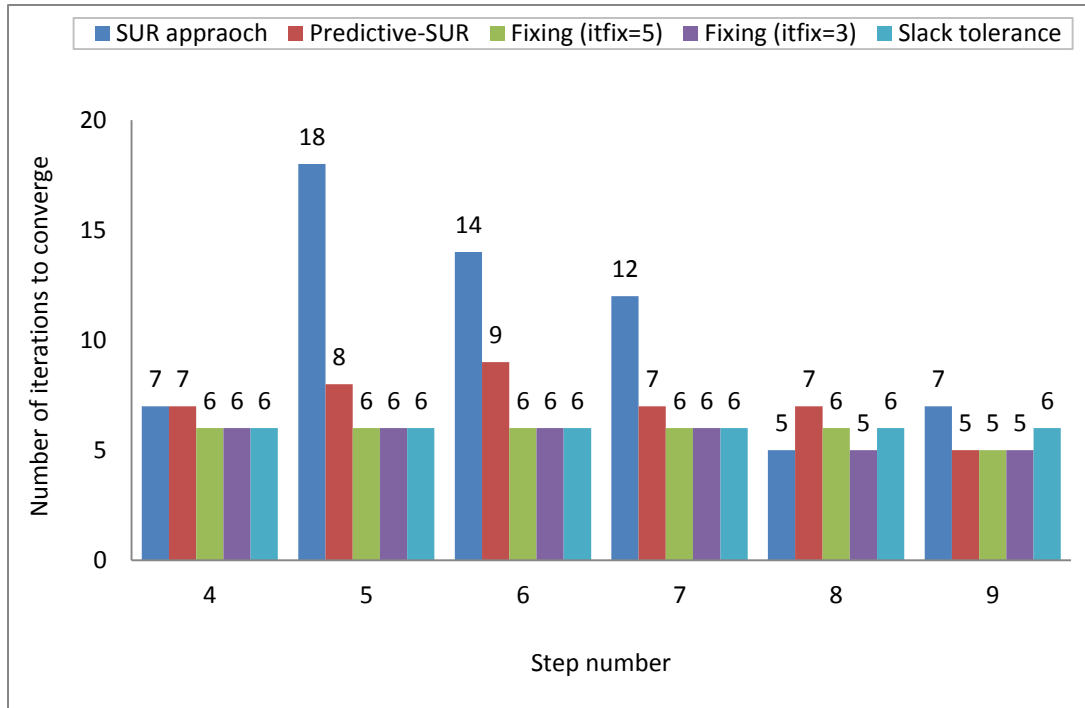


Figure 4.35: Number of iterations to achieve convergence for the most difficult increments with 40 increments.

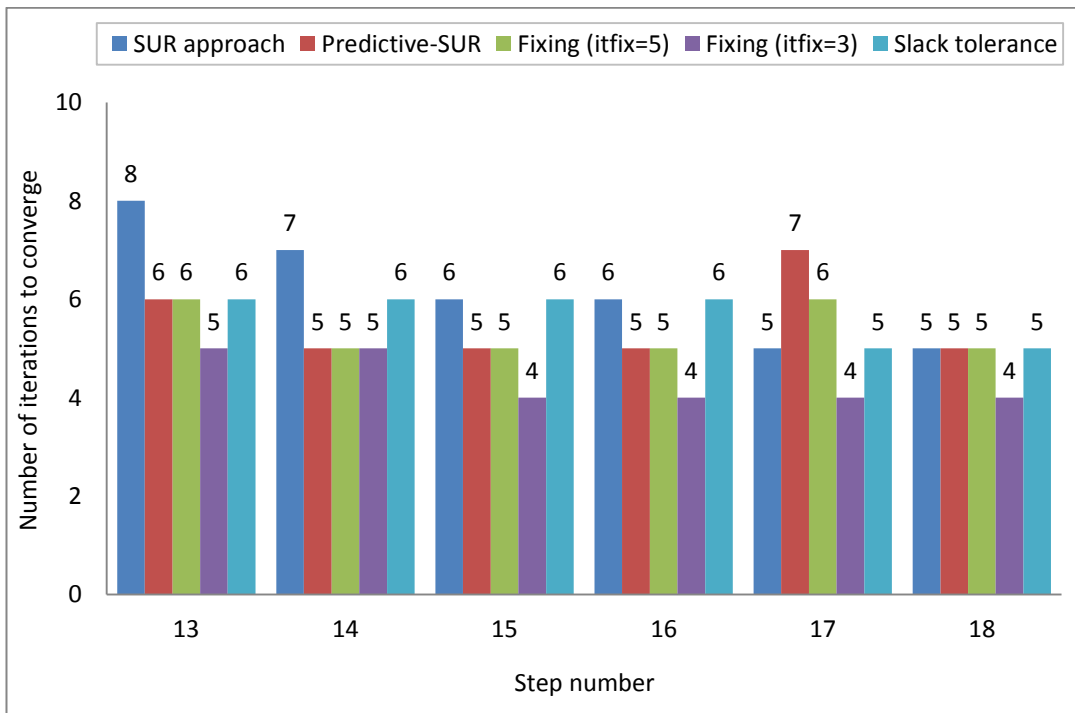


Figure 4.36: Number of iterations to achieve convergence for the most difficult increments with 100 increments.

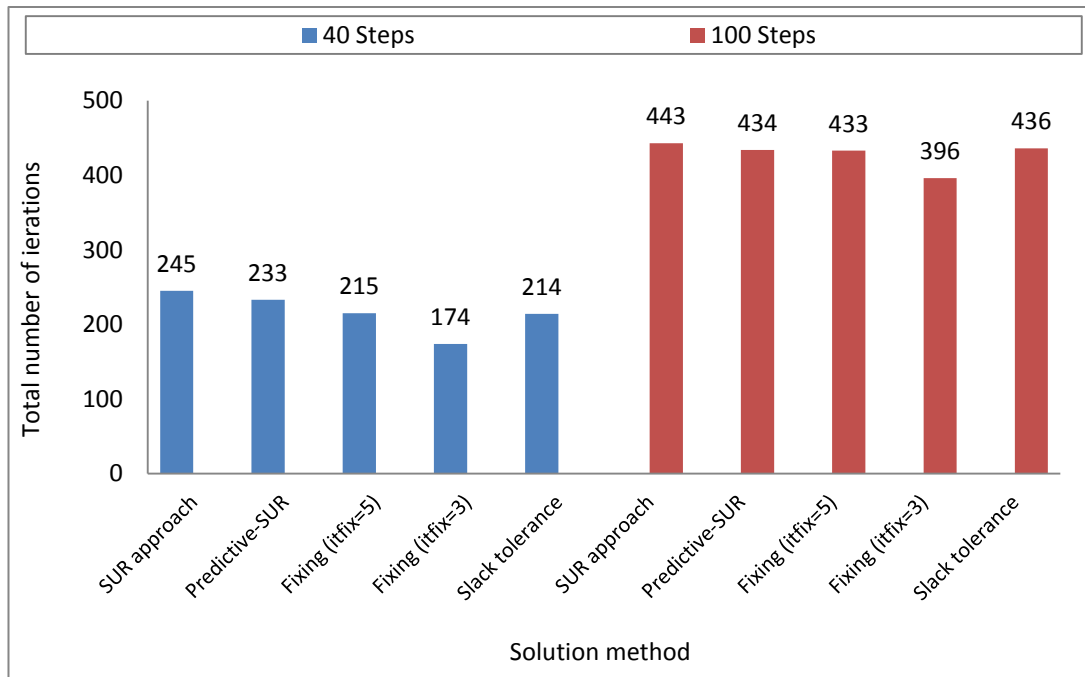


Figure 4.37: Total number of iterations that needed for each solution in the 2D double notched problem.

#### 4.4 Discussion and conclusions

In the present chapter, a number of new acceleration techniques were described to improve the convergence properties of the smooth unloading-reloading (SUR) method for the finite element simulation of quasi-brittle materials. These techniques were named; predictive-SUR approach, fixing approach and slack tolerance approach. The advantages of using these proposed acceleration algorithms with the SUR method were discussed and compared with each other.

In the predictive-SUR approach, a predictive function is developed for calculating a predictive converged value of a damage evolution parameter based on an extrapolation in semi-log space.

The second SUR technique named ‘fixing’ was based on a two stage algorithm, in which a damage evolution parameter is updated from the last converged increment in Stage-1 iterations, and then it is fixed in Stage-2 iterations within a step. In this

proposed approach two different number of iterations ( $it_{fix}=3$  and 5) in Stage-1 were investigated.

The third approach which has also been investigated is called slack tolerance technique. When the number of iterations within an increment exceeds 5 iterations in the SUR method, a switch to a slacker tolerance '1%' is employed for this specific difficult step. After that, the convergence tolerance reverts to the given specific tolerance in subsequent increments.

In all cases, the proposed acceleration algorithms resulted in fewer overall iterations than the standard SUR method. However, in the reinforced concrete example 4.3.3 there are particular increments for which acceleration algorithms used more iterations than the standard SUR algorithm. This is most evident in steps which follow-on from a previous step in which the predictive algorithm gave a very significant reduction in iterations (e.g. see steps 12 and 13 in Figure 30). This occurred mainly in the reinforced concrete example in which the cracking was more distributed than in the plain concrete examples. It is believed that temporarily freezing  $r_p$ , i.e. at a predicted/fixed value, causes the evolution of some local damage to be spread over 2 or 3 steps, rather over a single step. However, an important observation is that no appreciable difference in overall response, damage pattern, or stresses and strains was discernible between the solutions (i.e. standard SUR, predictive-SUR, fixing with  $it_{fix}=3$  or 5 and slack tolerance approaches), as judged from graphs and plots of these entities.

Overall, the three SUR acceleration algorithms described in this chapter are effective, reliable and result in substantial savings in terms of the total number iterations required for a complete solution, relative to the standard SUR approach, in some examples these savings were enormous.

The SUR 'fixing' approach, with  $it_{fix}=3$ , is the most efficient algorithm amongst those presented, but in some instances it can lead to a noticeable drift in the equilibrium path particularly when a substantial crack is established in a single solution step, as in example 4.3.2.

The 'predictive-SUR' 'fixing' -with  $it_{fix}=4$  or 5- and 'slack tolerance' approaches are all more reliable than the 'fixing with  $it_{fix}=3$  option' and always give the same responses as the standard SUR solution.

# Chapter 5

## A new formulation for elements with embedded strong discontinuities

---

### 5.1 Introduction

The numerical analysis of quasi-brittle structures requires careful consideration to obtain objective results with regard to mesh refinement due to the highly localized deformations that occur when these materials fail, i.e. the formation of cracks in concrete or shear bands in soils. Different approaches, such as the crack band model or models that employ localization limiters (e.g. nonlocal models, gradient-enhanced models and Cosserat continua) can be used to partially alleviate these problems, as mentioned in Section 2.4. However, these models require a sufficiently fine resolution of the localization zone to guarantee mesh objectivity and thus can be computationally very expensive when used to model large structures. Moreover, even with using advanced localization limiter techniques, which aim to properly simulate energy dissipation processes during softening, some undesirable side effects such as stress-locking and mesh bias problems cannot be completely overcome (Jirásek, 2000; Wells and Sluys, 2001a; Mosler, 2004; Mosler and Meschke, 2004; Foster et al., 2007; Mosler et al., 2011; Oliver et al., 2012).

In recent years, an alternative method called the Strong Discontinuity (SD) approach has been developed for the efficient modelling of strain localization in brittle and quasi-brittle materials. In this approach, cracks or fracture zones are represented as lines or surfaces of discontinuous displacements within individual finite elements. A discontinuity in the SD approach is permitted to arbitrarily propagate through the finite element mesh (Oliver et al., 2004). An important advantage of the SD approach, compared to other established techniques for the analysis of strain localization problems, is that it allows relatively large finite elements to be used.

This means that far fewer finite elements are required for the simulation of large scale structures (Oliver et al., 2003a; Mosler, 2005; Mosler, 2006; Radulovic et al., 2011; Parvaneh and Foster, 2016).

A number of EFEM formulations result in element stiffness matrices that are unsymmetric (Simo et al., 1993; Armero and Garikipati, 1996; Oliver, 1996a; Oliver, 1996b; Wells and Sluys, 2001b; Oliver et al., 2002; Alfaiate et al., 2002; Oliver et al., 2003a), which is undesirable from a computational point of view. Other formulations introduce extra degrees of freedom on element boundaries, which are either retained or eliminated using static condensation (Alfaiate et al., 2003; Linder and Armero, 2007; Dias-da-Costa et al., 2009a; Dias-da-Costa et al., 2010; Dias-da-Costa et al., 2013). The forms of the element stiffness matrices and associated strain displacement relationships in some of these formulations are somewhat cumbersome. In the proposed formulation, the only extra degrees of freedom introduced (in a 2D element) are two translations and a rotation at the midpoint of the discontinuity. These are eliminated using an equilibrium condition along the discontinuity. The resulting element has a symmetric tangent (and secant) stiffness matrix and a compact convenient form. The stiffness matrix is derived, using variational principles, from a total potential energy functional. Unlike the formulations of Linder and Armero (2007) and Dujc et al. (2013), the element does not include relative stretching along the discontinuity because the author believes this to be incompatible with the order of the element. It is noted that this type of stretching behaviour is readily modelled with multiple elements.

A new formulation for elements with embedded strong discontinuities is described in this chapter for simulating failure in 2D quasi-brittle materials. The proposed method can simulate a discontinuity and associated rigid body motions (normal and tangential separation) in a simple and effective way. A number of numerical examples are presented, which evaluate the performance of the new formulation as implemented in a 4-noded bilinear element. The results are compared with those obtained using interface elements and the smeared crack approach.

It should be also mentioned that the development of the new formulation is the primary stage of developing a strong discontinuity method that takes into account

diffuse micro-cracking which often occurs when a specimen is subject to compression, as explained in Section 6.2.

## 5.2 Kinematic of strong discontinuity

Consider a solid defined in the domain ( $\Omega$ ), as shown in Figure 5.1. The domain is divided by a discontinuity ( $\Gamma_d$ ) into two sub-regions ( $\Omega^+$ ) and ( $\Omega^-$ ), such that  $\Omega = \Omega^+ \cup \Omega^-$ .

For each material point ( $\mathbf{x}$ ) in  $\Omega$ , the total displacement field ( $\mathbf{u}$ ) is the sum of the continuous displacement field  $\bar{\mathbf{u}}$  and the enhanced displacement field  $\tilde{\mathbf{u}}$  due to the discontinuity.

$$\mathbf{u}(\mathbf{x}) = \bar{\mathbf{u}}(\mathbf{x}) + H_{\Gamma_d} \tilde{\mathbf{u}}(\mathbf{x}) \quad (5.1)$$

where  $H_{\Gamma_d}$  is the Heaviside jump function across the discontinuity. Here, the jump is considered to be fully transmitted to nodes in the positive sub-domain  $\Omega^+$  by means of the Heaviside function.

$$H_{\Gamma_d} = \begin{cases} 1 & \text{if } \mathbf{x} \in \Omega^+ \\ 0 & \text{otherwise} \end{cases} \quad (5.2)$$

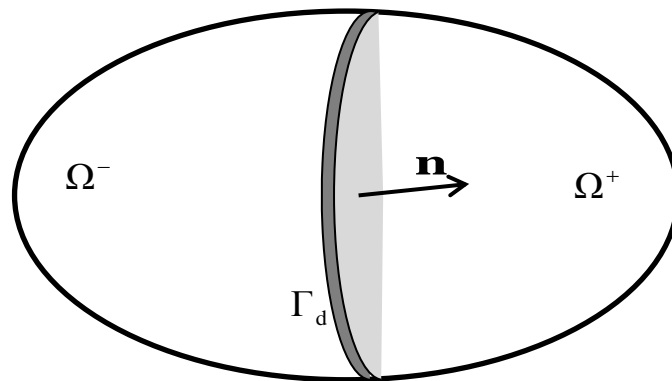


Figure 5.1: A Domain crossed by a strong discontinuity surface.

Assuming small displacements and strains, the total strain field is given by:

$$\boldsymbol{\varepsilon} = \nabla^s \mathbf{u} = \underbrace{\nabla^s \bar{\mathbf{u}} + H_{\Gamma_d} (\nabla^s \tilde{\mathbf{u}})}_{\text{bonded}} + \underbrace{\delta_{\Gamma_d} (\llbracket \mathbf{u} \rrbracket \otimes \mathbf{n})^s}_{\text{unbonded}} \quad (5.3)$$

Where  $(\bullet)^s$  refers to the symmetric part of  $(\bullet)$ ,  $\otimes$  denotes the dyadic product,  $\llbracket \mathbf{u} \rrbracket$  is the displacement jump vector and  $\mathbf{n}$  is the normal jump vector to  $\Gamma_d$ .  $\delta_{\Gamma_d}$  is the Dirac delta function along the surface of the discontinuity ( $\Gamma_d$ ) and can be written as:

$$\delta_{\Gamma_d} = \begin{cases} 0 & \text{if } \mathbf{x} \in \Omega \setminus \Gamma_d = \Omega^+ \cup \Omega^- \\ \infty & \text{if } \mathbf{x} \in \Gamma_d \end{cases} \quad (5.4)$$

Since the displacement discontinuity takes place in a very narrow bandwidth, both the displacement and the strain fields are bounded by material that remains continuous in the regions of  $\Omega^+$  and  $\Omega^-$ , thus the unbounded term in equation (5.4) vanishes in  $\Omega \setminus \Gamma_d = \Omega^+ \cup \Omega^-$ .

### 5.3 A new formulation for an element with an embedded SD

In this section, the derivation of a new finite element with an embedded strong discontinuity is presented. Let us consider a quadrilateral finite element as illustrated in Figure 5.2, in which a discontinuity of displacement field occurs along a straight line  $\Gamma_d$  crossing the element at an arbitrary direction ( $\theta$ ) and identified by unit vectors  $(\hat{\mathbf{r}}, \hat{\mathbf{s}}, \hat{\mathbf{t}})$ . The centre of the discontinuity line (within the element) is defined by the Cartesian coordinate vector  $\mathbf{x}_c$ . The relative rotation to the two crack phases ( $\alpha$ ) is assumed to be small. i.e. ( $\alpha = \sin \alpha = \tan \alpha$ ; in radians).

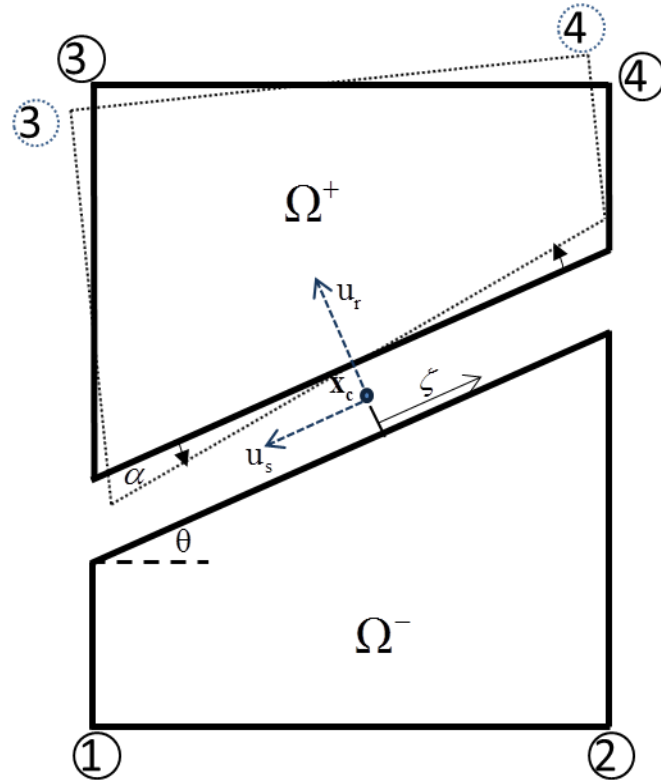


Figure 5.2: A four node element with an embedded strong discontinuity.

We assume an additional node ( $\tilde{\mathbf{W}}$ ) with three degrees of freedom (opening, sliding and rotation) located at the centre of the embedded strong discontinuity, in which  $\tilde{\mathbf{W}} = [u_r \quad u_s \quad \alpha]^T$ . Thus, the displacement of the nodes in the positive region ( $\Omega^+$ ) associated with  $\tilde{\mathbf{W}}$  can be computed.

The rotational displacement of a point i.e.  $\mathbf{x}$  in the element is given by:

$$\mathbf{R}(\mathbf{x}) = \alpha \hat{\mathbf{t}} \times (\mathbf{x} - \mathbf{x}_c) = \begin{bmatrix} R_1 \\ R_2 \end{bmatrix} \quad (5.5)$$

Where  $\mathbf{x} = (\xi, \eta)$  is the global position of any material point inside the finite element,  $\hat{\mathbf{t}}$  is out of plane unit vector  $\hat{\mathbf{t}} = [0 \quad 0 \quad 1]^T$  and  $\times$  is the cross product.

The displacement  $\mathbf{u}(\mathbf{x})$  is given by:

$$\mathbf{u}(\mathbf{x}) = \begin{bmatrix} r_1 & s_1 & R_1 \\ r_2 & s_2 & R_2 \end{bmatrix} \begin{bmatrix} u_r \\ u_s \\ \alpha \end{bmatrix} \quad (5.6)$$

Equation (5.6) is now written as:

$$\mathbf{u}(\mathbf{x}) = \mathbf{T}_w(\mathbf{x}) \tilde{\mathbf{W}} \quad (5.7)$$

where  $r_i$  and  $s_i$  are components of unit vectors  $\hat{\mathbf{r}}$  and  $\hat{\mathbf{s}}$  which are perpendicular and along the strong discontinuity respectively. For example, for the discontinuity shown in the Figure 5.2,  $r_1 = -\sin(\theta)$ ,  $r_2 = \cos(\theta)$ ,  $s_1 = -\cos(\theta)$  and  $s_2 = -\sin(\theta)$ .

The fracture strain  $\boldsymbol{\varepsilon}_{\text{fr}}(\mathbf{x})$  is the equivalent strain across the element due to the relative displacements (i.e. displacement jump) across the discontinuity.  $\boldsymbol{\varepsilon}_{\text{fr}}(\mathbf{x})$  is computed from the resulting additional displacement of the nodes in the region of  $\Omega^+$ , i.e. nodes number 3 and 4 in Figure 5.2, as follows;

$$\boldsymbol{\varepsilon}_{\text{fr}}(\mathbf{x}) = \mathbf{B} \begin{bmatrix} 0 & 0 & 0 \\ 0 & 0 & 0 \\ 0 & 0 & 0 \\ 0 & 0 & 0 \\ r_1 u_r & s_1 u_s & R_1(x_3) \alpha \\ r_2 u_r & s_2 u_s & R_2(x_3) \alpha \\ r_1 u_r & s_1 u_s & R_1(x_4) \alpha \\ r_2 u_r & s_2 u_s & R_2(x_4) \alpha \end{bmatrix} \quad (5.8)$$

Hence, the fracture strain can be re-written as:

$$\boldsymbol{\varepsilon}_{\text{fr}}(\mathbf{x}) = \mathbf{B} \begin{bmatrix} u_{x1} \\ u_{y1} \\ u_{x2} \\ u_{y2} \\ u_{x3} \\ u_{y3} \\ u_{x4} \\ u_{y4} \end{bmatrix} \quad (5.9)$$

where  $\mathbf{B}$  is the conventional strain-displacement matrix.  $\mathbf{B}$  at node i.e.  $i$  is:

$$\mathbf{B}_i = \begin{bmatrix} \partial N_i / \partial x & 0 \\ 0 & \partial N_i / \partial y \\ \partial N_i / \partial y & \partial N_i / \partial x \end{bmatrix} \quad (5.10)$$

where  $N_i$  denotes the shape function for node  $i$ .

The strain at any position in an element due to the strong discontinuity is given by:

$$\boldsymbol{\varepsilon}_{\text{fr}}(\mathbf{x}(\xi, \eta)) = \left[ \sum_{\Omega^+} \mathbf{B}_i(\xi, \eta) \mathbf{T}_{wi}(\mathbf{x}_i) \right] \tilde{\mathbf{W}} \quad (5.11)$$

Equation (5.11) can be simplified to:

$$\boldsymbol{\varepsilon}_{\text{fr}}(\mathbf{x}(\xi, \eta)) = \mathbf{M}(\xi, \eta) \tilde{\mathbf{W}} \quad (5.12)$$

in which  $\mathbf{M} = \mathbf{B} \cdot \mathbf{T}_w$

The total stiffness matrix for the embedded discontinuity is composed of the sum of regular stiffness matrix and the strong discontinuity element matrix. The stiffness matrix of the discontinuity can be computed as follows:

$$\mathbf{K}_r = \begin{bmatrix} K_r & 0 & 0 \\ 0 & K_s & 0 \\ 0 & 0 & K_\theta \end{bmatrix} \quad (5.13)$$

Where  $K_r$ ,  $K_s$  and  $K_\theta$  are the sliding, opening and rotational stiffnesses, which are defined as:

$$K_r = \frac{E_{ck} \cdot t}{(1 - \nu^2) h_{ck}} \quad (5.14)$$

$$K_s = \frac{E_{ck} \cdot t}{2(1 + \nu) h_{ck}} \quad (5.15)$$

$$K_\theta = \int_{-\frac{L_d}{2}}^{\frac{L_d}{2}} K_r \zeta d\zeta \quad (5.16)$$

The relationship between the force vector for the discontinuity and the discontinuity displacement vector is given by:

$$\mathbf{F}_r = \mathbf{K}_r \tilde{\mathbf{W}} \quad (5.17)$$

Where ( $E_{ck}$ ) is the Young's modulus of the discontinuity, ( $t$ ) is the out of plane thickness of the element, ( $L_d$ ) is the length of the discontinuity with the finite element and  $h_{ck}$  is the assumed thickness of the embedded discontinuity element. The assumption of the  $h_{ck}$  should be incredibly small, in this study  $h_{ck}$  was set to 1/100.

The total potential energy ( $\Pi$ ) for the element with embedded discontinuity is given by:

$$\Pi = \int_{\Omega} \frac{1}{2} (\boldsymbol{\varepsilon} - \boldsymbol{\varepsilon}_{\text{fr}})^T \mathbf{D} (\boldsymbol{\varepsilon} - \boldsymbol{\varepsilon}_{\text{fr}}) d\Omega + \frac{1}{2} \tilde{\mathbf{W}}^T \mathbf{K}_{\Gamma} \tilde{\mathbf{W}} \quad (5.18)$$

It should be borne in mind that the fracture strain  $\boldsymbol{\varepsilon}_{\text{fr}}$  changes only with respect of  $\tilde{\mathbf{W}}$ , if  $\boldsymbol{\varepsilon}$  is fixed. Hence, the variation of the total potential energy with respect of  $\tilde{\mathbf{W}}$  can be calculated as:

$$\begin{aligned} \delta \Pi(\tilde{\mathbf{W}}) &= \frac{1}{2} \int_{\Omega} \left( -\boldsymbol{\varepsilon}^T \mathbf{D} \delta \boldsymbol{\varepsilon}_{\text{fr}} + \boldsymbol{\varepsilon}_{\text{fr}}^T \mathbf{D} \delta \boldsymbol{\varepsilon}_{\text{fr}} - \delta \boldsymbol{\varepsilon}_{\text{fr}}^T \mathbf{D} \boldsymbol{\varepsilon} + \delta \boldsymbol{\varepsilon}_{\text{fr}}^T \mathbf{D} \boldsymbol{\varepsilon}_{\text{fr}} \right) d\Omega + \\ &\frac{1}{2} (\delta \tilde{\mathbf{W}}^T \mathbf{K}_{\Gamma} \tilde{\mathbf{W}} + \tilde{\mathbf{W}}^T \mathbf{K}_{\Gamma} \delta \tilde{\mathbf{W}}) = 0 \end{aligned} \quad (5.19)$$

Equation (5.19) can be simplified to:

$$\delta \Pi(\tilde{\mathbf{W}}) = \int_{\Omega} \left[ (-\delta \boldsymbol{\varepsilon}_{\text{fr}}^T \mathbf{D} \boldsymbol{\varepsilon}) + (\delta \boldsymbol{\varepsilon}_{\text{fr}}^T \mathbf{D} \boldsymbol{\varepsilon}_{\text{fr}}) \right] d\Omega + \delta \tilde{\mathbf{W}}^T \mathbf{K}_{\Gamma} \tilde{\mathbf{W}} = 0 \quad (5.20)$$

Using equation (5.12) and  $\boldsymbol{\varepsilon} = \mathbf{B}\mathbf{u}$ , equation (5.20) may be written as:

$$\delta \Pi(\tilde{\mathbf{W}}) = -\delta \tilde{\mathbf{W}}^T \left[ \int_{\Omega} \mathbf{M}^T \mathbf{D} \mathbf{B} d\Omega \cdot \mathbf{u} - \int_{\Omega} \mathbf{M}^T \mathbf{D} \mathbf{M} d\Omega \cdot \tilde{\mathbf{W}} - \mathbf{K}_{\Gamma} \tilde{\mathbf{W}} \right] = 0 \quad (5.21)$$

$$\mathbf{K}_{\Gamma} \tilde{\mathbf{W}} + \int_{\Omega} \mathbf{M}^T \mathbf{D} \mathbf{M} d\Omega \cdot \tilde{\mathbf{W}} = \int_{\Omega} \mathbf{M}^T \mathbf{D} \mathbf{B} d\Omega \cdot \mathbf{u} \quad (5.22)$$

then

$$\tilde{\mathbf{W}} = \left( \mathbf{K}_{\Gamma} + \int_{\Omega} \mathbf{M}^T \mathbf{D} \mathbf{M} d\Omega \right)^{-1} \int_{\Omega} \mathbf{M}^T \mathbf{D} \mathbf{B} d\Omega \cdot \mathbf{u} \quad (5.23)$$

Equations (5.12) and (5.23) can also be simplified to the following forms:

$$\tilde{\mathbf{W}} = \mathbf{B}_{\Gamma}^{-1} \mathbf{A}_{\Gamma} \mathbf{u} = \mathbf{C}_{\Gamma} \mathbf{u} \quad (5.24)$$

$$\boldsymbol{\varepsilon}_{fr} = \mathbf{M}\mathbf{C}_r \mathbf{u} \quad (5.25)$$

Now the total potential energy ( $\Pi$ ) becomes:

$$\Pi = \int_{\Omega} \frac{1}{2} \left( \mathbf{u}^T \mathbf{B}^T - \mathbf{u}^T \mathbf{C}_r^T \mathbf{M}^T \right)^T \mathbf{D} (\mathbf{B} - \mathbf{M}\mathbf{C}_r) d\Omega \mathbf{u} + \frac{1}{2} \mathbf{u}^T \mathbf{C}_r^T \mathbf{K}_r \mathbf{C}_r \mathbf{u} = \frac{1}{2} \mathbf{u}^T \mathbf{F} \quad (5.26)$$

Also equation (5.26) can be simplified further to:

$$\left( \int_{\Omega} \left( \mathbf{B}^T - \mathbf{C}_r^T \mathbf{M}^T \right)^T \mathbf{D} (\mathbf{B} - \mathbf{C}_r \mathbf{M}) d\Omega + \mathbf{C}_r^T \mathbf{K}_r \mathbf{C}_r \right) \mathbf{u} = \mathbf{F} \quad (5.27)$$

Thus, the stiffness matrix for an element with embedded strong discontinuity is given by:

$$\mathbf{K}_{\Omega} = \int_{\Omega} \left( \mathbf{B}^T - \mathbf{C}_r^T \mathbf{M}^T \right)^T \mathbf{D} (\mathbf{B} - \mathbf{C}_r \mathbf{M}) d\Omega + \mathbf{C}_r^T \mathbf{K}_r \mathbf{C}_r \quad (5.28)$$

## 5.4 Interface element formulation

Interface or contact elements are very useful for modelling material interfaces and for simulating discontinuities in bodies, such as cracks, shear bands or faults (Vignollet et al., 2015). Interface elements can be used for a wide range of applications, for instance, to model the intermediate layer between rocks and concrete, the interface between concrete and reinforcement, concrete fracture, aggregate interlock, soil-structure interactions and delamination in composite structures, etc. (Zubelewicz and Bažant, 1987; Rots, 1988; Jefferson, 1989; Rots, 1991; Schellekens and De Borst, 1993a; Schellekens and De Borst, 1993b; Alfaiate et al., 1997; Alfano and Crisfield, 2001; De Borst, 2006; Nazir and Dhanasekar, 2014; Truster, 2016).

Interface elements approach are particularly well suited to describing stationary discontinuities, or in other words, to describing situations in which the evolution of a

discontinuity is known a priori (Irzal et al., 2014; Vignollet et al., 2015). This method was used as a reference method in the first example of this chapter (see Section 5.7). In the interface element approach, a zero-thickness interface finite element is inserted along inter-element boundaries to represent the surfaces of potential discontinuities (Truster, 2016). A fundamental difference between the interface element and most other elements used in solid mechanics is that the constitutive relationship is between relative displacements and stresses as opposed to strains and stresses (Jefferson, 1989; Schellekens and De Borst, 1993b). From the numerical point of view, interface elements represent the standard method for simulating cohesive cracks in the finite element method (De Borst, 2006; Paggi and Wriggers, 2016).

This section reviews the formulation of 2D interface elements. Let us consider an interface element between two layers of a two-dimensional continuum, as shown in Figure 5.3. Assuming the thickness of the interface element is thin enough to be considered negligible with respect to the overall geometrical dimensions of the problem (Alfano and Crisfield, 2001). The interface element is also assumed to be composed by  $n$  pairs of nodes sharing the same coordinates and each node has two degrees of freedom. Indeed, nodal interface elements can be regarded as elements formed from smeared springs.

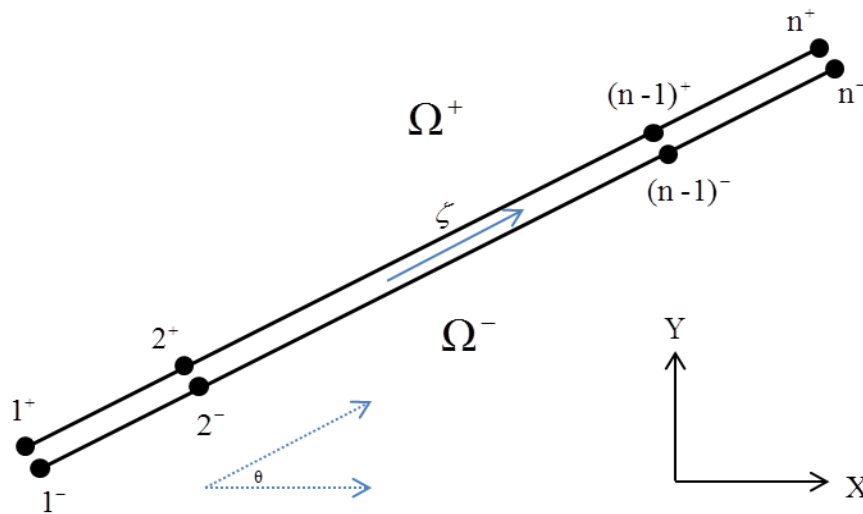


Figure 5.3: An interface element with  $n$  pairs of nodes in local coordinates.

The interface element geometry  $\mathbf{X}_\Gamma$  and the element displacement field  $\mathbf{U}_\Gamma$  are interpolated as:

$$\mathbf{X}_\Gamma = \mathbf{N}_\Gamma \mathbf{x}_i \quad (5.29)$$

$$\mathbf{U}_\Gamma = \mathbf{N}_\Gamma \mathbf{u}_i \quad (5.30)$$

where  $\mathbf{x}_i$  is the nodal geometry vector in global coordinates,  $\mathbf{u}_i$  is the nodal displacement vector in the global coordinates and  $\mathbf{N}_\Gamma$  contains the nodal interpolation functions of the interface element which are expressed in terms of the in-plane local coordinates ( $\zeta$ ) of the interface surface, see Table 5.1. The same interpolations are adopted for top and bottom sides of the interface element, which implies that nodes should be overlapped.

For the case shown in Figure 5.3,  $\mathbf{N}_\Gamma$  can be written as:

$$\mathbf{N}_\Gamma = \begin{bmatrix} -N_{1^-} & 0 & \dots & -N_{n^-} & 0 & N_{1^+} & 0 & \dots & N_{n^+} & 0 \\ 0 & -N_{1^-} & \dots & 0 & -N_{n^-} & 0 & N_{1^+} & \dots & 0 & N_{n^+} \end{bmatrix} \quad (5.31)$$

Table 5.1: Shape functions for the interface element shown in Figure 5.3.				
Node No	Shape function		Node No.	Shape function
$N_{1^-}$	$\frac{1}{2}(1-\zeta)$		$N_{1^+}$	$\frac{1}{2}(1-\zeta)$
$N_{2^-}$	$\frac{1}{2}(1-\zeta)$		$N_{2^+}$	$\frac{1}{2}(1-\zeta)$
$N_{(n-1)^-}$	$\frac{1}{2}(1+\zeta)$		$N_{(n-1)^+}$	$\frac{1}{2}(1+\zeta)$
$N_{n^-}$	$\frac{1}{2}(1+\zeta)$		$N_{n^+}$	$\frac{1}{2}(1+\zeta)$

The relative displacement  $\Delta \mathbf{U}_\Gamma$  is computed by taking the difference between the displacement at the upper ( $\Omega^+$ ) and lower ( $\Omega^-$ ) sides of the interface element. The relative displacement at any point is therefore can be given by the following relationship:

$$\Delta \mathbf{U}_\Gamma = \mathbf{N}_\Gamma \mathbf{u}^\Gamma \quad (5.32)$$

in which  $\mathbf{u}^\Gamma$  a vector that contains the interface element nodal displacements.

The stiffness matrix for the two dimensional interface element is given by (Rots, 1988; Schellekens and De Borst, 1993b; De Borst, 2006):

$$\mathbf{K}_{int} = \int_\Gamma \mathbf{N}_\Gamma^T \mathbf{T}_c \mathbf{C} \mathbf{T}_c^T \mathbf{N}_\Gamma d_\Gamma \quad (5.33)$$

in which  $\mathbf{T}_c$  is the transformation matrix,  $\mathbf{C}$  is the elastic interface stiffness matrix and the superscript  $(.)^T$  denotes the matrix transpose.  $\mathbf{T}_c$  and  $\mathbf{C}$  for the two-dimensional interface element are given by:

$$\mathbf{T}_c = \begin{bmatrix} \cos(\theta) & \sin(\theta) \\ -\sin(\theta) & \cos(\theta) \end{bmatrix} \quad (5.34)$$

$$\mathbf{C} = \begin{bmatrix} K_{ri} & 0 \\ 0 & K_{si} \end{bmatrix} \quad (5.35)$$

where  $K_{ri}$  and  $K_{si}$  are the normal and shear stiffnesses per unit area to the interface layer. These stiffnesses are defined as:

$$K_{ri} = \frac{E_{ck}}{(1-\nu^2) h_{ck}} \quad (5.36)$$

$$K_{si} = \frac{E_{ck}}{2(1+\nu)h_{ck}} \quad (5.37)$$

The undesired elastic deformation can be suppressed by using a sufficiently high values of the dummy stiffness for the interface element, in which  $E_{ck}$  is taken as  $10E$  unless noted otherwise (Schellekens and De Borst, 1993b; De Borst, 2006; Ciancio et al., 2007; Vignollet et al., 2015).

It should be mentioned here that a linear 4-noded interface element was used in this study, with two nodes in each face.

## 5.5 Damage function

In this chapter, the isotropic damage model presented in Section 3.2.1 was used. The scalar damage variable ( $\omega$ ) is governed by the effective strain damage evolution parameter ( $\zeta_{eff}$ ) and is based on the damage parameter for the SUR function given in equation (3.14), considering that ( $r_{eff} = \zeta_{eff} \cdot \sqrt{E}$ ).

The effective strain damage parameter can be computed as follows (Jefferson and Mihai, 2015):

$$\zeta_{eff} = \frac{\tilde{\epsilon}_1}{2} \left[ 1 + \left( \frac{\mu_\epsilon}{r_\zeta} \right)^2 \right] + \frac{1}{2r_\zeta^2} \sqrt{(r_\zeta^2 - \mu_\epsilon^2)^2 \tilde{\epsilon}_1^2 + 4r_\zeta^2 (\tilde{\epsilon}_2^2)} \quad (5.38)$$

The material constants  $r_\zeta$  and  $\mu_\epsilon$  are the relative shear strain intercept and the asymptotic shear friction factor, respectively, of the damage surface in strain space. These constants can be computed from the relative shear stress ( $r_\sigma$ ) and residual friction factor ( $\mu$ ), in which:  $r_\zeta = r_\sigma \cdot (E/G)$  and  $\mu_\epsilon = \mu \cdot (E/G)$ . Where  $r_\sigma$  and  $\mu$  are set to 1.25 and 0.8, respectively.  $\tilde{\epsilon}$  is crack-plane total strain vector,  $E$  is Young's modulus and  $G$  is the shear modulus. Noting that  $G = E/2(1+\nu)$ .

## 5.6 Numerical examples

In this section, the performance of the proposed interface embedded strong discontinuity approach, termed the ‘IESD approach’, is explored with several examples, which include linear and nonlinear interface behaviour. It well-known that the interface elements approach (IEA) is the most suitable approach to simulate a predefined strong discontinuity (Vignollet et al., 2015). Therefore, the IEA is used in the first example as a reference method to assess the performance of the proposed IESD method. In the other examples, results obtained from the proposed IESD method were compared with those obtained using the smeared crack approach.

In this study, a strong discontinuity is assumed to be embedded within a finite element when the maximum principal stress measured at the additional central node (see Figure 5.2) exceeds the tensile strength of the material. The crack is assumed to cross the centre of the finite element with an orientation perpendicular to the maximum principal stress direction. This orientation is updated at each iteration within the crack formation step, but is kept constant thereafter. In the examples (5.7.2 and 5.7.3) cracks were prescribed based on the nonlinear FE analysis of using smeared crack approach.

Plane-stress 4-noded bilinear isoparametric elements were used in all of the examples. Both bulk and discontinuity constitutive relationships were assumed to be linear elastic in the first example (5.7.1), whereas the damage model presented in Sections 3.2.1 and 5.6 was adopted for the other examples. Convergence tolerances for the nonlinear incremental-iterative analyses were equal to 0.001 for both incremental displacement L2 norm and incremental residual force vector L2 norm.

Linear elastic analyses on a single 2D square finite element using interface elements method and the proposed IESD approach were carried out in the first example (5.7.1). A linear interface element (4-node interface element) was used in this study. Four different loading cases were investigated and comparisons made between results obtained from both methods.

In the second numerical example (5.7.2), a series of nonlinear finite element analyses were conducted on a two-dimensional specimen with two notches in order to assess the performance of the proposed IESD method in mode-1 fracture. A coarse and a fine mesh with 100 and 2500 bilinear finite elements were studied in this example. In the third example (5.7.3), a nonlinear FE analysis was also performed under displacement control by imposing vertical and horizontal displacements on a double notched specimen in order to induce mixed mode fracture. Comparisons between results obtained from the proposed embedded strong discontinuity approach and the smeared approach were performed in these examples.

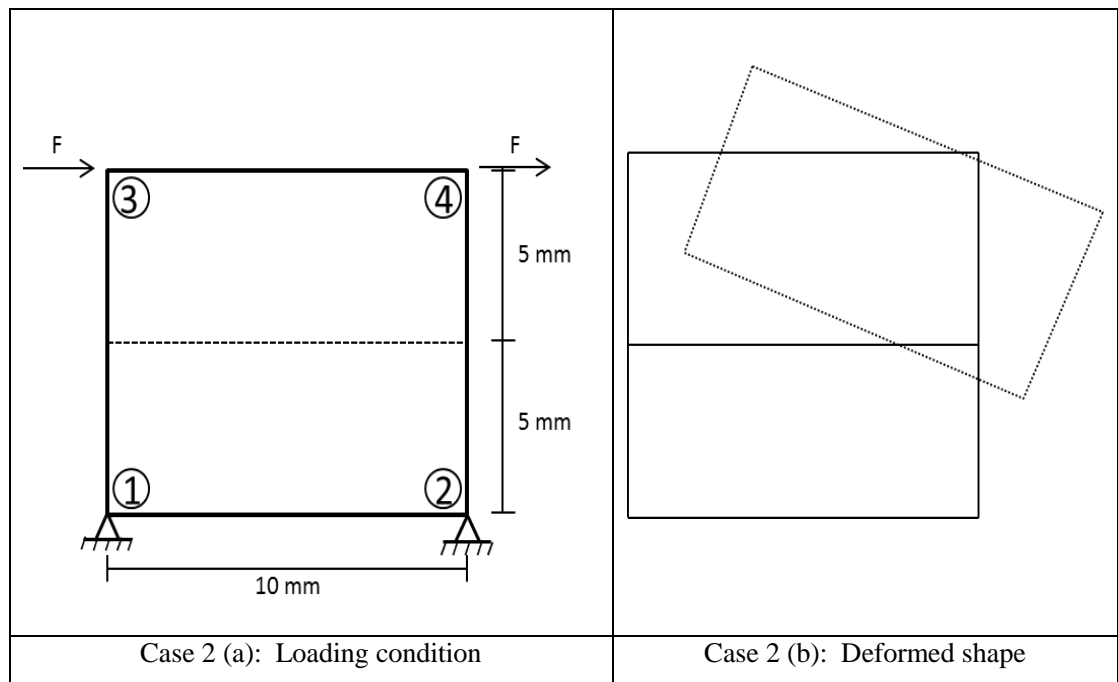
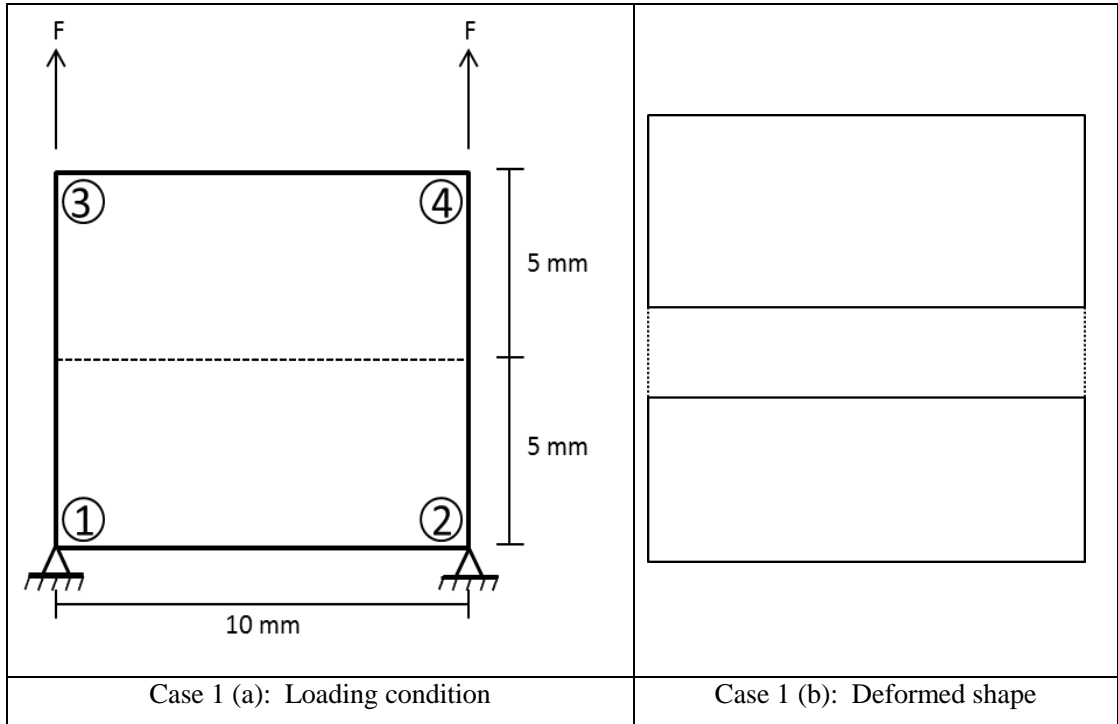
### **5.6.1 One-element examples.**

A linear elastic analysis was carried out on a quadrilateral element ( $10 \times 10 \times 1 \text{ mm}^3$ ) crossed by either a horizontal ( $\theta=0$ ) or an inclined ( $\theta \neq 0$ ) strong discontinuity for a range of loading scenarios. The geometry of the square element is given in Figure 5.4. The material properties used in this example are assumed as follows: Young's modulus ( $E=20,000 \text{ MPa}$ ), Young's modulus of the strong discontinuity ( $E_{ck}=0.0001 \text{ MPa}$ ), Poisson's ratio ( $\nu=0.20$ ).

Four different load cases were considered, which all involved combinations of unit loads ( $F=1 \text{ N}$ ) being applied to the top edge nodes, as illustrated in Figure 5.4. These cases represent mode-I, mode-II and mixed mode fracture conditions. Deformed element plots for every case are also given in Figure 5.4. The results obtained from the proposed interface element strong discontinuity IESD approach are compared with those obtained by the interface elements approach (IEA) in Table 5.2.

Table 5.2: Horizontal and vertical displacements at the top nodes for 4 studied cases.					
Case No.	Method type	Displacement at top nodes for IESD and IEA methods (mm)			
		Node number 3		Node number 4	
		$u_x$	$u_y$	$u_x$	$u_y$
Case 1	Proposed IESD approach	$1.3 \cdot 10^{-5}$	19.2	$-1.3 \cdot 10^{-5}$	19.2
	IEA	$1 \cdot 10^{-5}$	19.2	$-1 \cdot 10^{-5}$	19.2
Case 2	Proposed IESD approach	105.6	57.6	105.6	-57.6
	IEA	105.6	57.6	105.60	-57.6
Case 3	Proposed IESD approach	10.30	22.32	10.30	22.32
	IEA	10.30	22.32	10.30	22.32
Case 4	Proposed IESD approach	49.80	48.08	49.80	6.87
	IEA	49.80	48.08	49.80	6.87

From the comparison shown in Table 5.2 between nodal displacement results for the two methods, it can be concluded that there are negligible differences between the results obtained using the different idealisations.



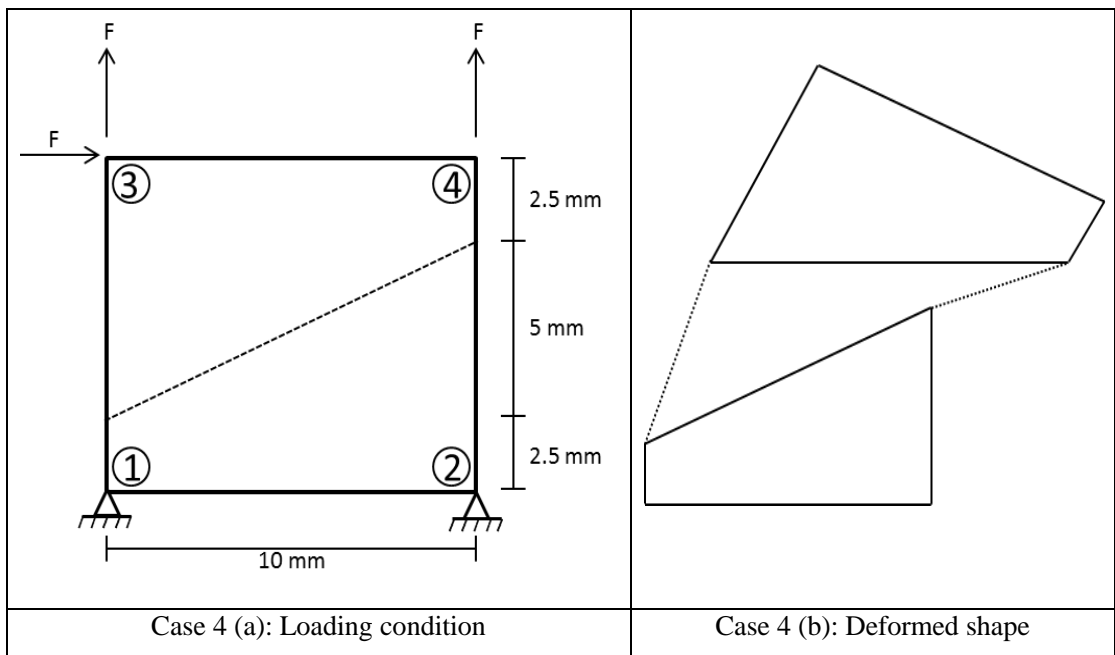
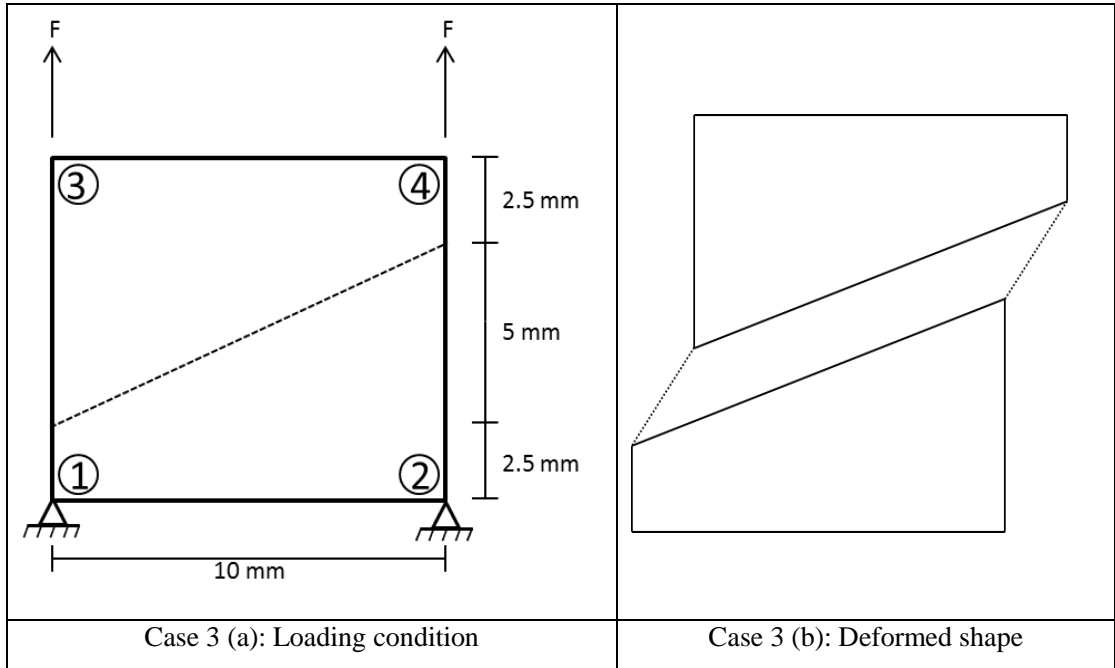


Figure 5.4: Loading conditions and deformed meshes using linear elastic analysis for the proposed IESD approach and IEA.

### 5.6.2 Two-dimensional tensile example

A non-linear analysis of a plain concrete specimen with two notches located at the centre of the specimen was undertaken using the smeared approach and the proposed IESD approach. The specimen dimensions are shown in Figure 5.5. Two meshes were studied, a coarse and a fine mesh with 100 and 2500 bilinear isoperimetric elements respectively. A 0.2 mm prescribed displacement was applied at the top nodes of the specimen to induce mode-I fracture (see Figure 5.6). It should be emphasised here again that the complete crack path was predefined in the proposed IESD approach by allowing the row of elements between the two notches to be only damaged.

The mechanical material properties of this specimen are:  $E=20,000$  MPa, the Young's modulus of the strong discontinuity is ten times stiffer than the Young's modulus ( $E_{ck}=10 * E$  MPa), Poisson's ratio ( $\nu =0.20$ ), fracture energy ( $G_f =0.10$  N/mm), tensile strength ( $f_t =2.5$  MPa),

The deformed configurations for both coarse and fine meshes are represented in Figure 5.6. Figure 5.7 shows the vertical stress vs the applied prescribed displacement curves obtained with both the proposed IESD and the smeared approach using the two meshes. Contour plot of the displacement in the specimen with a fine mesh at the last displacement increment of the analysis (step No. 40) is given in Figure 5.8.

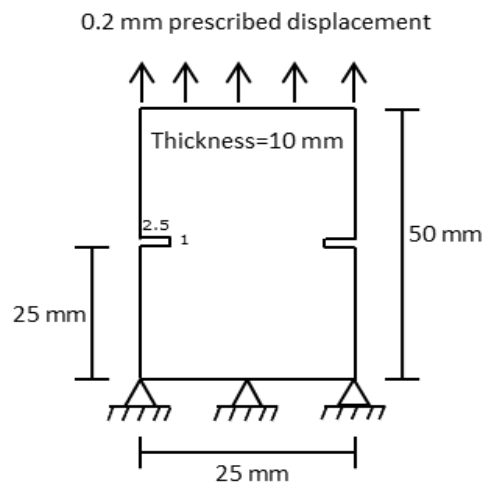


Figure 5.5: 2D plane stress specimen dimensions.

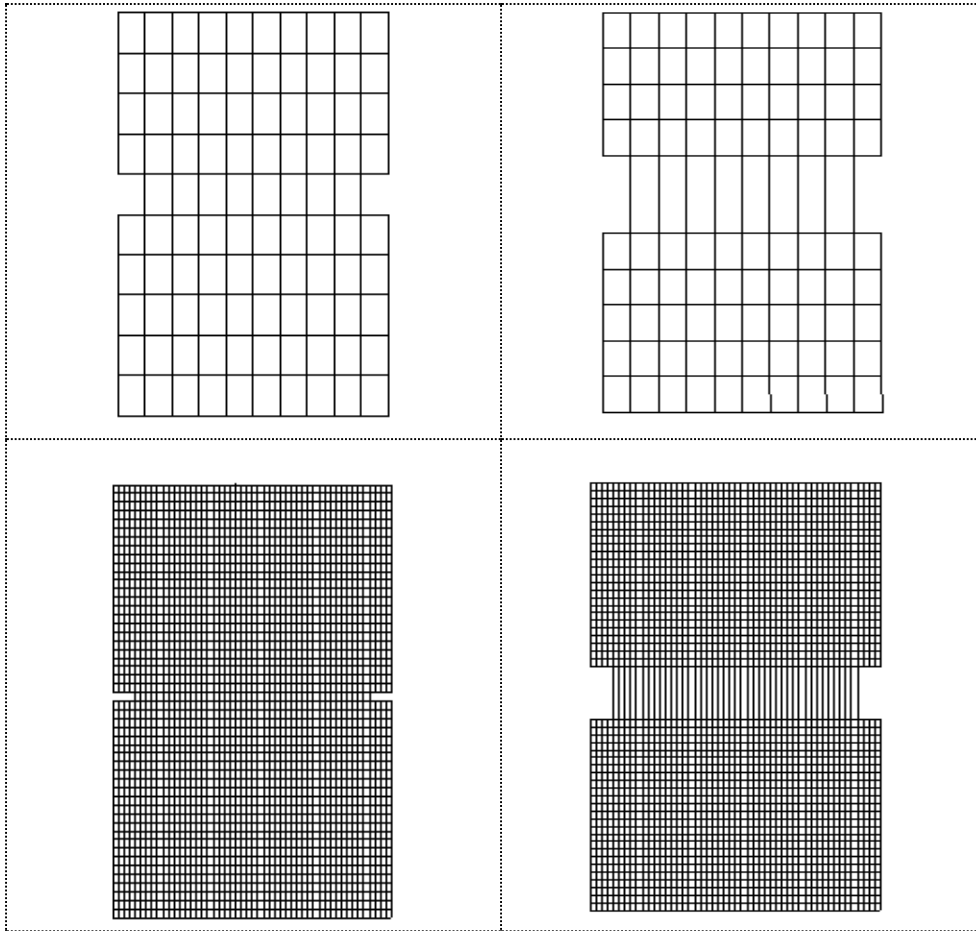


Figure 5.6: Coarse and fine meshes with their deformed shapes (magnified 30 times).

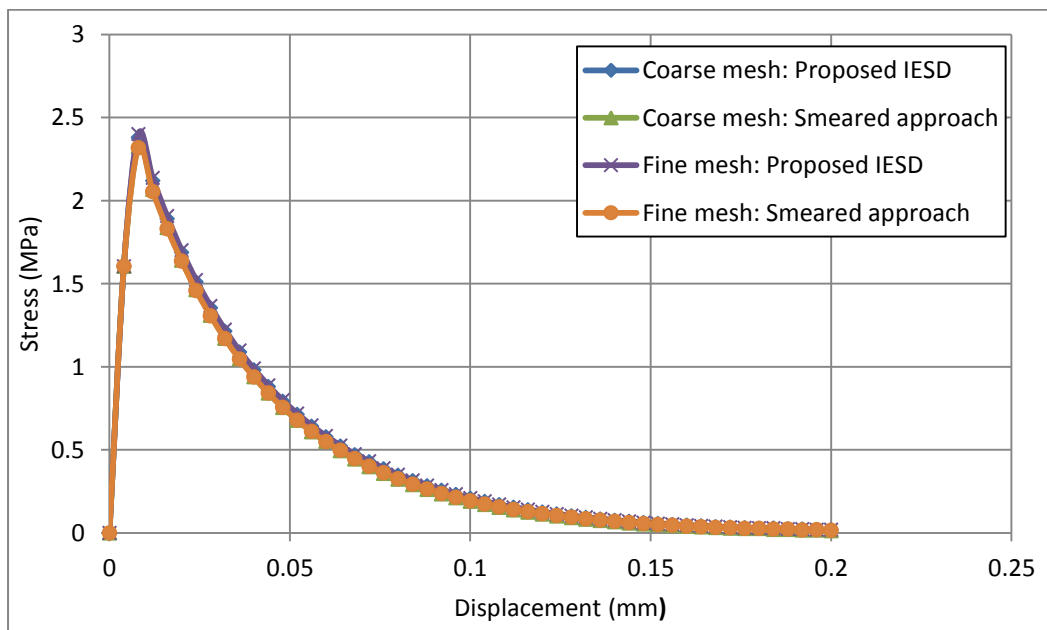


Figure 5.7: Stress-displacement responses with different methods.

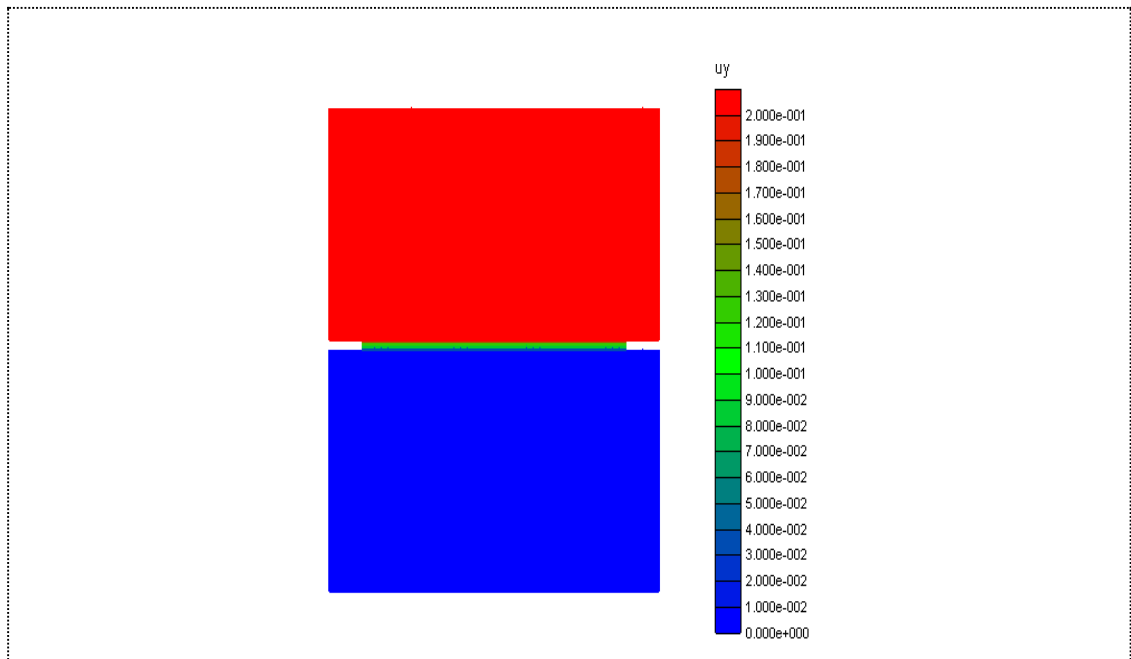


Figure 5.8: Vertical displacement contour plot for the fine mesh.

In this pure mode-I fracture example, the stress-displacement responses from the smeared approach and the proposed IESD approach are almost identical. In addition, deformed meshes as well as displacements contour plots obtained from the two methods were coincident, therefore only plots from the IESD analyses are depicted in Figures 5.6 and 5.8. It should be mentioned that there is no appreciable differences in the overall stress-displacement response or the crack pattern obtained using the coarse and fine mesh solutions; thus, in this case, accurate results can be achieved with a relatively coarse mesh.

This conclusion agrees with Mosler and Meschke (2004) who showed that in many situations, fracture energy-based smeared crack models give essentially the same response as elements with embedded strong discontinuities.

### 5.6.3 Double-notched example.

The third example simulates a two-dimensional notched plane stress specimen, loaded by prescribed displacements at the top edge nodes from two directions to induce mixed mode fracture behaviour, as shown in Figure 5.9. The analyses were carried out using 40 prescribed displacement increments and a mesh with 1250 elements.

The mechanical material properties of this example are:  $E=20,000$  MPa, the Young's modulus of the strong discontinuity is ten times stiffer than the undamaged Young's modulus (i.e.  $E_{ck}=10 * E$ ), Poisson's ratio ( $\nu =0.20$ ), fracture energy ( $G_f =0.10$  N/mm) and tensile strength ( $f_t =2.5$  MPa).

Exaggerated deformed mesh plots for both the smeared crack and IESD analyses at the final displacement increment are given in Figure 5.10.

Vertical displacement control loading =0.15 mm, and 0.25 mm horizontally.

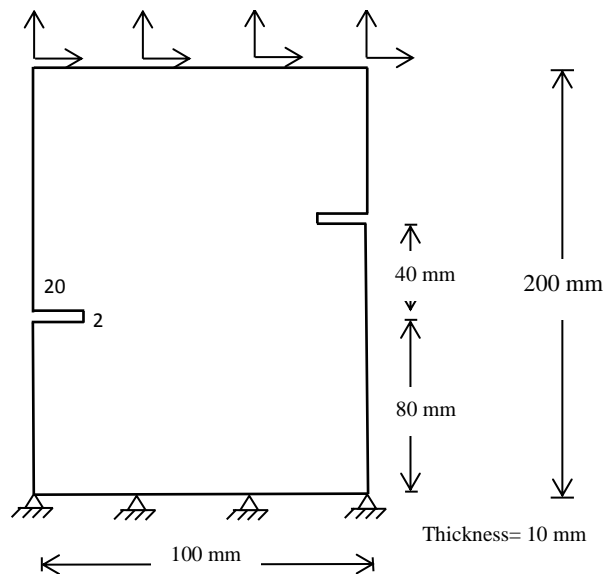


Figure 5.9: Double notched plane stress example.

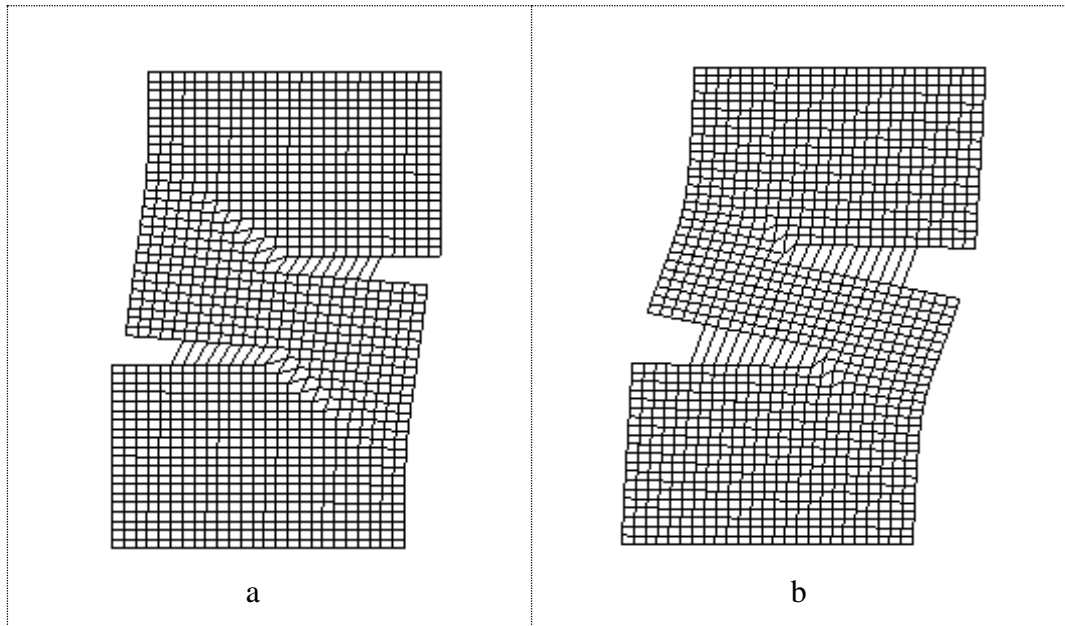


Figure 5.10: Exaggerated deformed mesh: (a) smeared approach and (b) proposed interface embedded strong discontinuity (IESD) approach.

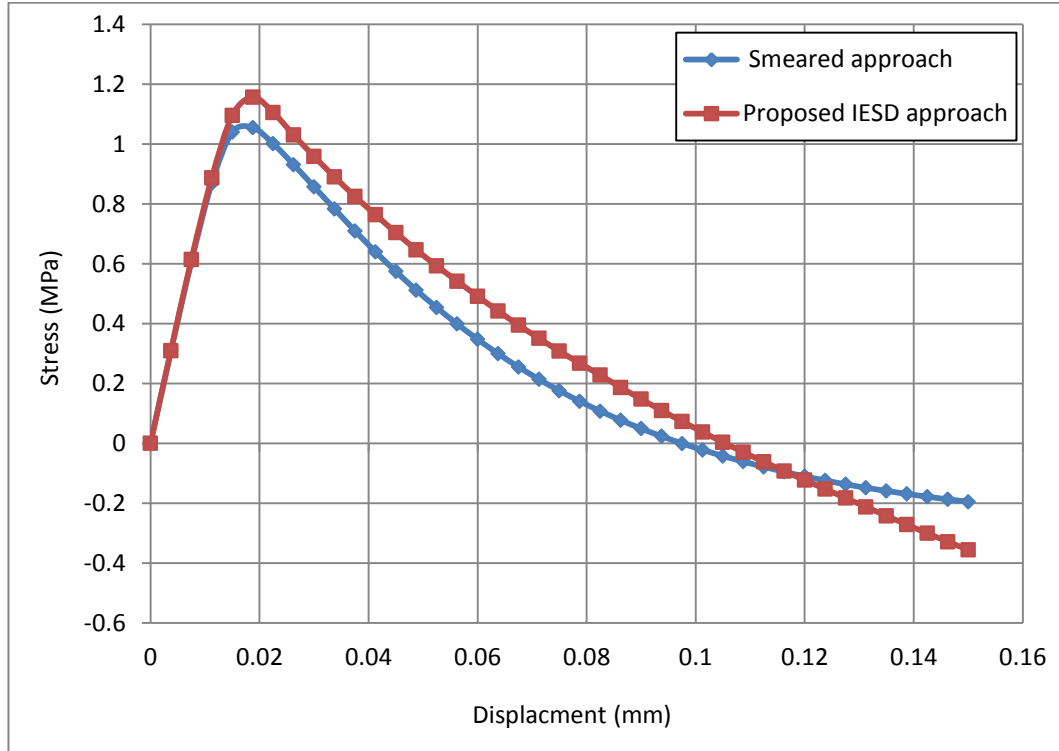


Figure 5.11: Vertical stress and displacement response.

As can be observed from Figure 5.11, there is a small difference between the peak stresses obtained with smeared approach and the IESD approach. The overall stress-displacement responses from the two approaches are similar. The differences can be attributed to the following:

- In the proposed IESD approach a discontinuity is assumed to cross the centre of a finite element, while in the smeared crack approach the strong discontinuity is modelled by reducing the stiffness and strength of the element at its Gauss points.
- The effective crack directions from the two analyses may not be the same because, in the IESD approach, a crack can change during the first step but is fixed thereafter, whereas the smeared damage model does not directly simulate directional cracks. In the latter case, the crack plane is assumed, a posteriori, to be normal to the maximum principal strain direction and this plane can change throughout the analysis.

## **5.7 Discussion and conclusions**

A new formulation for an element with an embedded strong discontinuity is presented in this chapter to model failure of quasi-brittle materials and this is named the interface embedded strong discontinuity (IESD) approach. The key feature of the proposed IESD approach is that an additional dummy node is assumed at the centre of the discontinuity to measure the opening, sliding and rotational displacements.

When an initial damage criterion is met at the SD reference node, an embedded discontinuity is added to the continuum part of the element. In the present implementation, this discontinuity is assumed to occur at the finite element centre with an orientation normal to the maximum principal stress direction. This orientation is updated in the damage initiation step, but is kept constant in the remaining steps.

It is noted that the formulation allows the reference node to be located anywhere within the continuum element even though it is placed centrally in the examples described in this chapter.

Several 2D elements examples were used to assess the performance of the proposed SD approach for modelling mode-1, mode-2 and mixed mode fracture. In all examples, 4-noded bilinear isoparametric elements were used and plane stress conditions were assumed. Moreover, in all of these examples, the complete strong discontinuity path was predefined, and interface elements and the smeared crack approach were used as reference methods for comparison purposes.

In the linear analysis of the example (5.7.1), the results showed that the proposed IESD approach gives almost identical results to those obtained using interface elements. Furthermore, the nonlinear finite element analysis of the mode-1 fracture example (5.7.2) showed that the stress-displacement responses from the smeared approach and the proposed IESD approach were almost identical for both coarse and fine meshes. In the mixed mode fracture example (5.7.3), the stress-displacement curve obtained from the IESD approach was close to the stress-displacement curve obtained using the smeared crack approach.

In summary, results obtained from all examples showed without a doubt that the proposed IESD method is able to model the failure of structural elements formed from quasi-brittle materials. Moreover, the new element formulation has certain advantages over many other SD approaches, e.g. the element shape functions do not have to be modified nor is static condensation (in the conventional form) needed. An additional positive feature of the IESD approach is that it leads to a symmetric stiffness matrix. Furthermore, the proposed approach is easy to implement in finite element codes and computationally efficient.

# Chapter 6

## Conclusions and future work

---

### 6.1 Conclusions

The main aims of the work presented in this thesis were to **(i)** to develop a robust incremental iterative numerical method for the nonlinear finite element analysis of quasi-brittle materials and, **(ii)** to develop a new formulation for elements with embedded strong discontinuities. The first aim was addressed in Chapters 3 and 4, whilst work undertaken on the second aim was presented in Chapter 5.

In Chapter 3, a new method for improving the robustness and convergence characteristics of a damage model when applied to the nonlinear finite element analysis of fracture problems in quasi-brittle materials was described. This method, named the smooth unloading-reloading (SUR) approach, employs a smooth unloading-reloading function as a basis for computing an approximate positive-definite finite element tangent matrix in an incremental iterative Newton type solution procedure. Also, in this chapter a new convenient approach for computing the characteristic length parameter for a range of 2D and 3D finite elements was presented.

The SUR was developed to work with an incremental iterative nonlinear finite element solution scheme and thus it is compatible with other FE materials models developed for this standard type of solution algorithm.

A range of idealised quasi-brittle specimens were used to assess the performance of the new SUR method. From the results of these examples, it is concluded that the SUR method is numerically robust, accurate and results in considerable savings, in terms of the number of iterations used in a complete solution, relative to a model that

uses a secant unloading-reloading function. A further conclusion is that the SUR approach rarely (if ever) results in numerical breakdown.

In order to further improve the convergence properties of the new SUR method, three accelerations techniques were proposed in Chapter 4. These acceleration techniques were introduced into the SUR solution algorithm. These techniques were designated ‘predictive-SUR’, ‘fixing’ and ‘slack tolerance’ approaches:

- I. The concept of the predictive-SUR algorithm relies on two parameters, namely the damage evolution parameter and the number of iterations. In this proposed approach, a function is employed to predict a converged value of a damage evolution parameter based on an extrapolation in semi-log space.
- II. In the ‘fixing’ technique, two stages of iteration within each load step are introduced in the SUR approach. In Stage-1 iterations, a damage evolution parameter is updated from the last converged increment, and then is fixed in the Stage-2 iterations. The effect of using three or five iterations in Stage-1 was investigated.
- III. The third proposed approach uses a slightly slacker convergence tolerance at key stages in a computation. The slacker tolerance (1% for the L2 norm of out of balance residual forces) is temporarily triggered when the number of iterations within an increment exceeds a certain limit (e.g. 5 iterations). Subsequently, the convergence tolerance reverts to the standard tighter tolerance of (0.001 or 0.000001).

The results from all of the examples presented in Chapter 4 proved that the three proposed acceleration techniques are effective, reliable and result in substantial savings in terms of the total number iterations required to achieve convergence for the SUR solution. In some examples, these savings were substantial. Thus, it is concluded that the proposed acceleration techniques achieve solutions in less computer time than the standard SUR solution, with no appreciable effect on the accuracy of simulations.

In Chapter 5, the formulation of a new element with an embedded strong discontinuity was presented. This formulation was applied to a 4-noded quadrilateral element. This method was named the interface embedded strong discontinuity (IESD) approach. The IESD approach employs a single internal node at a reference point within the element. This node has sufficient translational and rotational degrees of freedom to fully describe the kinematics of the strong discontinuity, and these degrees of freedom are eliminated at the element level.

The applicability of the proposed IESD approach for modelling mode-1, mode-2 and mixed mode fracture were investigated by a number of numerical 2D-examples using linear and nonlinear finite element analyses. In all numerical examples 4-node bilinear elements were used in the work of this thesis. Results obtained from the IESD approach were compared with those obtained from using the interface element approach and the smeared crack approach.

The conclusions from this work are that the IESD approach captures the rigid body motion in a simple and effective way, the proposed element has symmetric matrices and that it is easy to implement in finite element codes.

It is also concluded that the proposed embedded strong discontinuity approach is able to model fracture in quasi-brittle materials effectively with a good accuracy relative to the interface element method and the smeared approach.

At the end of the work of this thesis, the author would like to mention that the smooth unloading-reloading method, with one of the acceleration techniques has been implemented in the commercial finite element program LUSAS and is currently in use by a number of their clients. This software is one of the most widely used finite element packages for civil engineering applications in the UK.

## 6.2 Recommendations for future work

The following suggestions for future work are made.

- The available methods for the nonlinear finite element analysis of quasi-brittle materials that can overcome stability and convergence difficulties are the ‘*sequentially linear approach*’, the ‘*implicit-explicit approach*’ and the newly developed ‘*smooth-unloading-reloading approach*’. It would be useful, if a comparison between these three methods is made.
- The SUR method should be linked to an arc-length approach so that snap-back behaviour can be captured.
- The application of the new formulation, for an element with an embedded strong discontinuity, to three dimensional elements would be a valuable piece of further work.
- The proposed embedded strong discontinuity approach should be applied to a variety of fracture mechanics problems using different finite elements types.
- The method used for simulating the transition from diffuse damage to a strong discontinuity should be refined and extended to account for compressive micro-cracking. Currently, the method employed involves abruptly switching off damage and transferring the associated inelastic relative-displacements to the embedded strong discontinuity when the damage parameter at a particular point reaches a chosen threshold value. However, this method does not account for the type of diffuse micro-cracking that often occurs when a specimen is subject to compression. The formulation should be extended to provide a seamless transition from micro to macro cracking and to simulate the simultaneous evolution of both micro and macro cracks within a single element.

# Appendices

---

## Appendix A: Direct tensor notation

Table A.1 shows notations for the direct tensor operations that employed in this thesis, in which  $\alpha$  denotes a scalar,  $\mathbf{a}$  and  $\mathbf{b}$  represent first order tensors (i.e. vectors).  $\mathbf{A}$ ,  $\mathbf{B}$  and  $\mathbf{C}$  are second-order tensors and  $\mathbf{P}$ ,  $\mathbf{Q}$  and  $\mathbf{R}$  denote fourth-order tensors.

Table A.1: Direct tensor notation (Voyiadjis and Kattan, 2006).

Direct tensor notation	Summation convention
$\alpha = \mathbf{a} \cdot \mathbf{b}$	$\alpha = a_i b_i$
$\mathbf{A} = \mathbf{a} \otimes \mathbf{b}$	$A_{ij} = a_i b_j$
$\alpha = \mathbf{A} : \mathbf{B}$	$\alpha = A_{ij} B_{ij}$
$\mathbf{C} = \mathbf{A} \cdot \mathbf{B}$	$C_{ik} = A_{ij} B_{jk}$
$\mathbf{P} = \mathbf{A} \otimes \mathbf{B}$	$P_{ijkl} = A_{ij} B_{kl}$
$\mathbf{C} = \mathbf{P} : \mathbf{A}$	$C_{ij} = P_{ijkl} A_{kl}$
$\mathbf{B} = \mathbf{A} : \mathbf{P}$	$B_{kl} = A_{ij} P_{ijkl}$
$\mathbf{R} = \mathbf{P} \cdot \mathbf{Q}$	$R_{ijmn} = P_{ijkl} Q_{klmn}$

## Appendix B: Derivation of the constitutive tangent stiffness

Constitutive equation

$$\boldsymbol{\sigma} = (1 - \omega) \mathbf{D}_0 : \boldsymbol{\varepsilon} \quad (\text{B.1})$$

Constitutive tangent equation

$$\dot{\boldsymbol{\sigma}} = (1 - \omega) \mathbf{D}_0 \dot{\boldsymbol{\varepsilon}} - \dot{\omega} \mathbf{D}_0 \boldsymbol{\varepsilon} \quad (\text{B.2})$$

Consider damage rate

$$\dot{\omega} = \frac{d\omega}{dr} \left( \frac{dr}{d\boldsymbol{\varepsilon}} \right)^T \dot{\boldsymbol{\varepsilon}} \quad (\text{B.3})$$

$$\dot{\boldsymbol{\sigma}} = (1 - \omega) \mathbf{D}_0 \dot{\boldsymbol{\varepsilon}} - \frac{d\omega}{dr} \mathbf{D}_0 \boldsymbol{\varepsilon} \left( \frac{dr}{d\boldsymbol{\varepsilon}} \right)^T \dot{\boldsymbol{\varepsilon}} \quad (\text{B.4})$$

$$\dot{\boldsymbol{\sigma}} = (1 - \omega) \mathbf{D}_0 \dot{\boldsymbol{\varepsilon}} - \frac{d\omega}{dr} \boldsymbol{\sigma}_0 \left( \frac{dr}{d\boldsymbol{\sigma}_0} \frac{d\boldsymbol{\sigma}_0}{d\boldsymbol{\varepsilon}} \right)^T \dot{\boldsymbol{\varepsilon}} \quad (\text{B.5})$$

$$\dot{\boldsymbol{\sigma}} = (1 - \omega) \mathbf{D}_0 \dot{\boldsymbol{\varepsilon}} - \frac{d\omega}{dr} \boldsymbol{\sigma}_0 \left( \frac{dr}{d\boldsymbol{\sigma}_0} \mathbf{D}_0 \right)^T \dot{\boldsymbol{\varepsilon}} \quad (\text{B.6})$$

## References

1	ACI 1997. Finite Element Analysis of Fracture in Concrete Structures: State-of-the-Art. <i>ACI Committee 446</i> , 33.
2	Alfaiate, J., Pires, E. B. & Martins, J. A. C. 1997. A finite element analysis of non-prescribed crack propagation in concrete. <i>Computers &amp; Structures</i> , 63, 17-26.
3	Alfaiate, J., Simone, A. & Sluys, L. J. 2003. Non-homogeneous displacement jumps in strong embedded discontinuities. <i>International Journal of Solids and Structures</i> , 40, 5799-5817.
4	Alfaiate, J., Wells, G. N. & Sluys, L. J. 2002. On the use of embedded discontinuity elements with crack path continuity for mode-I and mixed-mode fracture. <i>Engineering Fracture Mechanics</i> , 69, 661-686.
5	Alfano, G. & Crisfield, M. A. 2001. Finite element interface models for the delamination analysis of laminated composites: mechanical and computational issues. <i>International Journal for Numerical Methods in Engineering</i> , 50, 1701-1736.
6	Armero, F. & Garikipati, K. 1996. An analysis of strong discontinuities in multiplicative finite strain plasticity and their relation with the numerical simulation of strain localization in solids. <i>International Journal of Solids and Structures</i> , 33, 2863-2885.
7	Armero, F. & Linder, C. 2008. New finite elements with embedded strong discontinuities in the finite deformation range. <i>Computer Methods in Applied Mechanics and Engineering</i> , 197, 3138-3170.
8	Armero, F. & Linder, C. 2009. Numerical simulation of dynamic fracture using finite elements with embedded discontinuities. <i>International Journal of Fracture</i> , 160, 119-141.
9	Bathe, K. J. 2006. <i>Finite Element Procedures</i> , Prentice Hall.
10	Bathe, K. J. & Cimento, A. P. 1980. Some practical procedures for the solution of nonlinear finite element equations. <i>Computer Methods in Applied Mechanics and Engineering</i> , 22, 59-85.
11	Bažant, Z. & Jirásek, M. 2002. Nonlocal Integral Formulations of Plasticity and Damage: Survey of Progress. <i>Journal of Engineering Mechanics</i> , 128, 1119-1149.
12	Bažant, Z. P. 1976. Instability, Ductility, and Size Effect in Strain-Softening Concrete. <i>Journal of the Engineering Mechanics Division</i> , 102, 331-344.

13	Bažant, Z. P. 1992. Fracture Mechanics of Concrete Structures: <i>Proceedings of the First International Conference on Fracture Mechanics of Concrete Structures (FraMCoS1), held at Beaver Run Resort, Breckenridge, Colorado, USA, 1-5 June 1992</i> , Taylor & Francis.
14	Bažant, Z. P. 2002. Concrete fracture models: testing and practice. <i>Engineering Fracture Mechanics</i> , 69, 165-205.
15	Bažant, Z. P. & Cedolin, L. 2010. <i>Stability of Structures: Elastic, Inelastic, Fracture and Damage Theories</i> , World Scientific.
16	Bažant, Z. P. & Oh, B. H. 1983. Crack band theory for fracture of concrete. <i>Material and Construction</i> , 16, 155-177.
17	Bažant, Z. P. & Pijaudier-Cabot, G. 1988. Nonlocal continuum damage, localization instability and convergence. <i>Journal of applied mechanics</i> , 55, 287-293.
18	Bažant, Z. P. & Planas, J. 1997. <i>Fracture and Size Effect in Concrete and Other Quasibrittle Materials</i> , Taylor & Francis.
19	Becker, A. 2004. <i>An introduction Guide to Finite Element Analysis</i> , London, Uk, Professional Engineering Publishing.
20	Belytschko, T. & Black, T. 1999. Elastic crack growth in finite elements with minimal remeshing. <i>International Journal for Numerical Methods in Engineering</i> , 45, 601-620.
21	Belytschko, T., Fish, J. & Engelmann, B. E. 1988. A finite element with embedded localization zones. <i>Computer Methods in Applied Mechanics and Engineering</i> , 70, 59-89.
22	Belytschko, T., Gracie, R. & Ventura, G. 2009. A review of extended/generalized finite element methods for material modeling. <i>Modelling and Simulation in Materials Science and Engineering</i> , 17, 043001.
23	Belytschko, T., Liu, W. K., Moran, B. & Elkhodary, K. 2013. <i>Nonlinear finite elements for continua and structures</i> , John Wiley & Sons.
24	Belytschko, T., Moës, N., Usui, S. & Parimi, C. 2001. Arbitrary discontinuities in finite elements. <i>International Journal for Numerical Methods in Engineering</i> , 50, 993-1013.
25	Borja, R. I. 2000. A finite element model for strain localization analysis of strongly discontinuous fields based on standard Galerkin approximation. <i>Computer Methods in Applied Mechanics and Engineering</i> , 190, 1529-1549.
26	Borja, R. I. 2008. Assumed enhanced strain and the extended finite element methods: A unification of concepts. <i>Computer Methods in Applied Mechanics and Engineering</i> , 197, 2789-2803.

27	Carol, I., Rizzi, E. & Willam, K. 2001. On the formulation of anisotropic elastic degradation. I. Theory based on a pseudo-logarithmic damage tensor rate. <i>International Journal of Solids and Structures</i> , 38, 491-518.
28	Červenka, J., Bažant, Z. P. & Wierer, M. 2005. Equivalent localization element for crack band approach to mesh-sensitivity in microplane model. <i>International Journal for Numerical Methods in Engineering</i> , 62, 700-726.
29	Cervera, M. 2008. A smeared-embedded mesh-corrected damage model for tensile cracking. <i>International Journal for Numerical Methods in Engineering</i> , 76, 1930-1954.
30	Cervera, M. & Chiumenti, M. 2006a. Mesh objective tensile cracking via a local continuum damage model and a crack tracking technique. <i>Computer Methods in Applied Mechanics and Engineering</i> , 196, 304-320.
31	Cervera, M. & Chiumenti, M. 2006b. Smeared crack approach: back to the original track. <i>International Journal for Numerical and Analytical Methods in Geomechanics</i> , 30, 1173-1199.
32	Cervera, M., Chiumenti, M. & Codina, R. 2010. Mixed stabilized finite element methods in nonlinear solid mechanics: Part II: Strain localization. <i>Computer Methods in Applied Mechanics and Engineering</i> , 199, 2571-2589.
33	Cervera, M., Chiumenti, M. & Codina, R. 2011. Mesh objective modeling of cracks using continuous linear strain and displacement interpolations. <i>International Journal for Numerical Methods in Engineering</i> , 87, 962-987.
34	Chaboche, J.-L. 1981. Continuous damage mechanics — A tool to describe phenomena before crack initiation. <i>Nuclear Engineering and Design</i> , 64, 233-247.
35	Chen, W. F. 2007. <i>Plasticity in Reinforced Concrete</i> , J. Ross Pub.
36	Chen, W. F. & Han, D. J. 2012. <i>Plasticity for Structural Engineers</i> , Springer New York.
37	Ciancio, D., Carol, I. & Cuomo, M. 2007. Crack opening conditions at ‘corner nodes’ in FE analysis with cracking along mesh lines. <i>Engineering Fracture Mechanics</i> , 74, 1963-1982.
38	Comi, C. & Perego, U. 2001. Fracture energy based bi-dissipative damage model for concrete. <i>International Journal of Solids and Structures</i> , 38, 6427-6454.
39	Crisfield, M. 1982a. Local instabilities in the nonlinear analysis of reinforced concrete beams and slabs. <i>Proceedings of the Institution of Civil Engineers</i> , 73, 135-145.

40	Crisfield, M. A. 1981. A fast incremental/iterative solution procedure that handles “snap-through”. <i>Computers &amp; Structures</i> , 13, 55-62.
41	Crisfield, M. A. 1982b. Accelerated solution techniques and concrete cracking. <i>Computer Methods in Applied Mechanics and Engineering</i> , 33, 585-607.
42	Crisfield, M. A. 1983. An arc-length method including line searches and accelerations. <i>International Journal for Numerical Methods in Engineering</i> , 19, 1269-1289.
43	Crisfield, M. A. 1984. Difficulties with current numerical models for reinforced concrete and some tentative solutions. <i>International Conference on Computer-aided Analysis and Design of Concrete Structures</i> , Damjanic F, Hinton E, Owen DRJ, Bicanic N, Simovic V (eds). Pineridge Press: Swansea, Pineridge Press, 331–358.
44	Crisfield, M. A. 1991. <i>Non-linear Finite Element Analysis of Solids and Structures</i> , Chichester, UK., John Wiley & Sons.
45	Crisfield, M. A. 1997. <i>Non-linear Finite Element Analysis of Solids and Structures</i> , Chichester, UK., John Wiley & Sons.
46	Crisfield, M. A. & Wills, J. 1988. Solution strategies and softening materials. <i>Computer Methods in Applied Mechanics and Engineering</i> , 66, 267-289.
47	Daichao, S., Scott, S. & Abbo., A. 2002. An Automatic Newton-Raphson Scheme. <i>International Journal of Geomechanics</i> , 2, 471-502.
48	De Borst, R. 1987. Computation of post-bifurcation and post-failure behavior of strain-softening solids. <i>Computers &amp; Structures</i> , 25, 211-224.
49	De Borst, R. 1997. Some recent developments in computational modelling of concrete fracture. <i>International Journal of Fracture</i> , 86, 5-36.
50	De Borst, R. 2001. Some recent issues in computational failure mechanics. <i>International Journal for Numerical Methods in Engineering</i> , 52, 63-95.
51	De Borst, R. 2006. Modern domain-based discretization methods for damage and fracture. <i>Advances in Fracture Research</i> . Springer.
52	De Borst, R., Crisfield, M. A., Remmers, J. J. C. & Verhoosel, C. V. 2012. <i>Nonlinear Finite Element Analysis of Solids and Structures</i> , Wiley.
53	De Borst, R., Pamin, J. & Geers, M. G. D. 1999. On coupled gradient-dependent plasticity and damage theories with a view to localization analysis. <i>European Journal of Mechanics - A/Solids</i> , 18, 939-962.
54	De Borst, R., Remmers, J. J. C., Needleman, A. & Abellan, M. A. 2004. Discrete vs smeared crack models for concrete fracture: bridging the gap. <i>International Journal for Numerical and Analytical Methods in Geomechanics</i> , 28, 583-607.

55	DeJong, M. J., Hendriks, M. A. N. & Rots, J. G. 2008. Sequentially linear analysis of fracture under non-proportional loading. <i>Engineering Fracture Mechanics</i> , 75, 5042-5056.
56	Dennis, J., J. & Moré, J. 1977. Quasi-Newton Methods, Motivation and Theory. <i>SIAM Review</i> , 19, 46-89.
57	Dias-da-Costa, D., Alfaiate, J., Sluys, L. J., Areias, P. & Júlio, E. 2013. An embedded formulation with conforming finite elements to capture strong discontinuities. <i>International Journal for Numerical Methods in Engineering</i> , 93, 224-244.
58	Dias-da-Costa, D., Alfaiate, J., Sluys, L. J. & Júlio, E. 2009a. A discrete strong discontinuity approach. <i>Engineering Fracture Mechanics</i> , 76, 1176-1201.
59	Dias-da-Costa, D., Alfaiate, J., Sluys, L. J. & Júlio, E. 2009b. Towards a generalization of a discrete strong discontinuity approach. <i>Computer Methods in Applied Mechanics and Engineering</i> , 198, 3670-3681.
60	Dias-da-Costa, D., Alfaiate, J., Sluys, L. J. & Júlio, E. 2010. A comparative study on the modelling of discontinuous fracture by means of enriched nodal and element techniques and interface elements. <i>International Journal of Fracture</i> , 161, 97-119.
61	Dujc, J., Brank, B. & Ibrahimbegovic, A. 2013. Stress-hybrid quadrilateral finite element with embedded strong discontinuity for failure analysis of plane stress solids. <i>International Journal for Numerical Methods in Engineering</i> , 94, 1075-1098.
62	Dujc, J., Brank, B. & Ibrahimbegović, A. 2010. Quadrilateral finite element with embedded strong discontinuity for failure analysis of solids. <i>Computer Modeling in Engineering and Sciences</i> , 69, 223-260.
63	Dureisseix, D., Ladevèze, P. & Schrefler, B. A. 2003. A LATIN computational strategy for multiphysics problems: application to poroelasticity. <i>International Journal for Numerical Methods in Engineering</i> , 56, 1489-1510.
64	Elfgren, L. & Noghabai, K. 2001. Tension of reinforced concrete prisms. Round robin analysis and tests on bond: . <i>A report from an investigation arranged by RILEM Technical Committee 147-FMB Fracture Mechanics to Anchorage and Bond Research Report</i> . Luleå University of Technology, Division of Structural Engineering.
65	Eliáš, J. 2015. Generalization of load–unload and force-release sequentially linear methods. <i>International Journal of Damage Mechanics</i> , 24, 279-293.
66	Eliáš, J., Frantík, P. & Vořechovský, M. 2010. Improved sequentially linear solution procedure. <i>Engineering Fracture Mechanics</i> , 77, 2263-2276.

67	Etse, G. & Willam, K. 1994. Fracture energy formulation for inelastic behavior of plain concrete. <i>Journal of engineering mechanics</i> , 120, 1983-2011.
68	Faria, R., Oliver, J. & Cervera, M. 1998. A strain-based plastic viscous-damage model for massive concrete structures. <i>International Journal of Solids and Structures</i> , 35, 1533-1558.
69	Feenstra, P. H. & De Borst, R. 1995. A plasticity model and algorithm for mode-I cracking in concrete. <i>International Journal for Numerical Methods in Engineering</i> , 38, 2509-2529.
70	Foster, C. D., Borja, R. I. & Regueiro, R. A. 2007. Embedded strong discontinuity finite elements for fractured geomaterials with variable friction. <i>International Journal for Numerical Methods in Engineering</i> , 72, 549-581.
71	Fries, T.-P. & Belytschko, T. 2010. The extended/generalized finite element method: an overview of the method and its applications. <i>International Journal for Numerical Methods in Engineering</i> , 84, 253-304.
72	Gálvez, J. C., Planas, J., Sancho, J. M., Reyes, E., Cendón, D. A. & Casati, M. J. 2013. An embedded cohesive crack model for finite element analysis of quasi-brittle materials. <i>Engineering Fracture Mechanics</i> , 109, 369-386.
73	Gernay, T., Millard, A. & Franssen, J.-M. 2013. A multiaxial constitutive model for concrete in the fire situation: Theoretical formulation. <i>International Journal of Solids and Structures</i> , 50, 3659-3673.
74	Graça-e-Costa, R., Alfaiate, J., Dias-da-Costa, D., Neto, P. & Sluys, L. J. 2013. Generalisation of non-iterative methods for the modelling of structures under non-proportional loading. <i>International Journal of Fracture</i> , 182, 21-38.
75	Graça-e-Costa, R., Alfaiate, J., Dias-da-Costa, D. & Sluys, L. J. 2012. A non-iterative approach for the modelling of quasi-brittle materials. <i>International Journal of Fracture</i> , 178, 281-298.
76	Grassl, P. & Jirásek, M. 2006. Damage-plastic model for concrete failure. <i>International Journal of Solids and Structures</i> , 43, 7166-7196.
77	Grassl, P., Lundgren, K. & Gylltoft, K. 2002. Concrete in compression: a plasticity theory with a novel hardening law. <i>International Journal of Solids and Structures</i> , 39, 5205-5223.
78	Grassl, P., Xenos, D., Nyström, U., Rempling, R. & Gylltoft, K. 2013. CDPM2: A damage-plasticity approach to modelling the failure of concrete. <i>International Journal of Solids and Structures</i> , 50, 3805-3816.
79	Han, D. & Chen, W.-F. 1987. Constitutive modeling in analysis of concrete structures. <i>Journal of engineering mechanics</i> , 113, 577-593.

80	Hayhurst, D. R. 1972. Creep rupture under multi-axial states of stress. <i>Journal of the Mechanics and Physics of Solids</i> , 20, 381-382.
81	He, W., Wu, Y.-F., Xu, Y. & Fu, T.-T. 2015. A thermodynamically consistent nonlocal damage model for concrete materials with unilateral effects. <i>Computer Methods in Applied Mechanics and Engineering</i> , 297, 371-391.
82	Hellweg, H. B. & Crisfield, M. A. 1998. A new arc-length method for handling sharp snap-backs. <i>Computers &amp; Structures</i> , 66, 704-709.
83	Hendriks, M. A. N. & Rots, J. G. 2013. Sequentially linear versus nonlinear analysis of RC structures. <i>Engineering Computations</i> , 30, 792-801.
84	Hillerborg, A., Modéer, M. & Petersson, P.-E. 1976. Analysis of crack formation and crack growth in concrete by means of fracture mechanics and finite elements. <i>Cement and concrete research</i> , 6, 773-781.
85	Hu, X. Z. & Wittmann, F. H. 1992. Fracture energy and fracture process zone. <i>Materials and Structures</i> , 25, 319-326.
86	Ibrahimbegovic, A. 2009. <i>Nonlinear Solid Mechanics: Theoretical Formulations and Finite Element Solution Methods</i> , Springer Netherlands.
87	Ingraffea, A. R. & Manu, C. 1980. Stress-intensity factor computation in three dimensions with quarter-point elements. <i>International Journal for Numerical Methods in Engineering</i> , 15, 1427-1445.
88	Ingraffea, A. R. & Saouma, V. 1985. Numerical modeling of discrete crack propagation in reinforced and plain concrete. In: SIH, G. & DITOMMASO, A. (eds.) <i>Fracture mechanics of concrete: Structural application and numerical calculation</i> . Springer Netherlands.
89	Invernizzi, S., Trovato, D., Hendriks, M. A. N. & van de Graaf, A. V. 2011. Sequentially linear modelling of local snap-back in extremely brittle structures. <i>Engineering Structures</i> , 33, 1617-1625.
90	Irzal, F., Remmers, J. J. C., Verhoosel, C. V. & de Borst, R. 2014. An isogeometric analysis Bézier interface element for mechanical and poromechanical fracture problems. <i>International Journal for Numerical Methods in Engineering</i> , 97, 608-628.
90	Jefferson, A. D. 1989. <i>Finite element analysis of composite structures</i> . PhD, University of Wales (Cardiff).
91	Jefferson, A. D. 2003. Craft—a plastic-damage-contact model for concrete. I. Model theory and thermodynamic considerations. <i>International Journal of Solids and Structures</i> , 40, 5973-5999.
92	Jefferson, A. D. & Mihai, I. C. 2015. The simulation of crack opening–closing and aggregate interlock behaviour in finite element concrete models. <i>International Journal for Numerical Methods in Engineering</i> , 104, 48-78.

93	Jefferson, A. D., Mihai, I. C., Tenchev, R., Alnaas, W. F., Cole, G. & Lyons, P. 2016. A plastic-damage-contact constitutive model for concrete with smoothed evolution functions. <i>Computers &amp; Structures</i> , 169, 40-56.
94	Jirásek, M. 2000. Comparative study on finite elements with embedded discontinuities. <i>Computer Methods in Applied Mechanics and Engineering</i> , 188, 307-330.
95	Jirásek, M. 2007. Mathematical analysis of strain localization. <i>Revue Européenne de Génie Civil</i> , 11, 977-991.
96	Jirásek, M. 2011. Damage and Smeared Crack Models. In: HOFSTETTER, G. & MESCHKE, G. (eds.) <i>Numerical Modeling of Concrete Cracking</i> . Springer Vienna.
97	Jirásek, M. & Bauer, M. 2012. Numerical aspects of the crack band approach. <i>Computers &amp; Structures</i> , 110–111, 60-78.
98	Jirásek, M. & Belytschko, T. Computational resolution of strong discontinuities. Proceedings of Fifth World Congress on Computational Mechanics, WCCM V, Vienna University of Technology, Austria, 2002.
99	Jirásek, M. & Bazant, Z. P. 2002. <i>Inelastic analysis of structures</i> , John Wiley & Sons.
100	Jirásek, M. & Grassl, P. 2008. Evaluation of directional mesh bias in concrete fracture simulations using continuum damage models. <i>Engineering Fracture Mechanics</i> , 75, 1921-1943.
101	Jirásek, M. & Marfia, S. 2005. Non-local damage model based on displacement averaging. <i>International Journal for Numerical Methods in Engineering</i> , 63, 77-102.
102	Jirásek, M. & Patzák, B. 2002. Consistent tangent stiffness for nonlocal damage models. <i>Computers &amp; Structures</i> , 80, 1279-1293.
103	Jirásek, M., Rolshoven, S. & Grassl, P. 2004. Size effect on fracture energy induced by non-locality. <i>International Journal for Numerical and Analytical Methods in Geomechanics</i> , 28, 653-670.
104	Jirásek, M. & Zimmermann, T. 1998. Rotating crack model with transition to scalar damage. <i>Journal of engineering mechanics</i> , 124, 277-284.
105	Kachanov, L. M. 1958. Rupture time under creep conditions. <i>Izvestia Akademii Nauk</i> , 8, 26-31.
106	Karihaloo, B. L. 1995. <i>Fracture Mechanics and Structural Concrete</i> , Longman Scientific & Technical.

107	Karihaloo, B. L., Abdalla, H. M. & Imjai, T. 2003. A simple method for determining the true specific fracture energy of concrete. <i>Magazine of Concrete Research</i> , 55, 471-481.
108	Kattan, P. I. & Voyiadjis, G. Z. 2001. <i>Damage Mechanics with Finite Elements: Practical Applications with Computer Tools</i> , Springer Berlin Heidelberg.
109	Kerfriden, P., Allix, O. & Gosselet, P. 2009. A three-scale domain decomposition method for the 3D analysis of debonding in laminates. <i>Computational Mechanics</i> , 44, 343-362.
110	Kim, J. 2013. <i>New finite elements with embedded strong discontinuities to model failure of three-dimensional continua</i> . PhD., University of California, Berkeley.
111	Krajcinovic, D. & Fonseka, G. 1981. The continuous damage theory of brittle materials, part 1: general theory. <i>Journal of applied Mechanics</i> , 48, 809-815.
112	La Borderie, C., Mazars, J. & Pijaudier-Cabot, G. 1992. Response of plain and reinforced concrete structures under cyclic loadings. <i>American Concrete Institute</i> , 134, 147-172.
113	Ladeveze, P. 1999. <i>Nonlinear Computational Structural Mechanics: New Approaches and Non-Incremental Methods of Calculation</i> , Springer New York.
114	Lemaitre, J. & Chaboche, J. L. 1990. <i>Mechanics of Solid Materials</i> , Cambridge University Press.
115	Lin, F. & Whu, A. 1992. Nonlocal smeared cracking model: characteristic length and energy dissipation. <i>Fract. Mech. Concr. Struct., Elsevier</i> , 313-318.
116	Linder, C. 2007. <i>New finite elements with embedded strong discontinuities to model failure of three-dimensional continua</i> . PhD., University of California, Berkeley.
117	Linder, C. & Armero, F. 2007. Finite elements with embedded strong discontinuities for the modeling of failure in solids. <i>International Journal for Numerical Methods in Engineering</i> , 72, 1391-1433.
118	Linder, C. & Armero, F. 2009. Finite elements with embedded branching. <i>Finite Elements in Analysis and Design</i> , 45, 280-293.
119	Litewka, A. & Debinski, J. 2003. Load-induced oriented damage and anisotropy of rock-like materials. <i>International Journal of Plasticity</i> , 19, 2171-2191.
120	Lotfi, H. R. & Shing, P. B. 1995. Embedded representation of fracture in concrete with mixed finite elements. <i>International Journal for Numerical Methods in Engineering</i> , 38, 1307-1325.

121	Ma, S. Y. A. & May, I. M. 1986. The Newton-Raphson method used in the non-linear analysis of concrete structures. <i>Computers &amp; Structures</i> , 24, 177-185.
122	Manzoli, O., Oliver, J., Diaz, G. & Huespe, A. 2008. Three-dimensional analysis of reinforced concrete members via embedded discontinuity finite elements. <i>Revista IBRACON de Estruturas e Materiais</i> , 58-83.
123	Matthies, H. & Strang, G. 1979. The solution of nonlinear finite element equations. <i>International Journal for Numerical Methods in Engineering</i> , 14, 1613-1626.
124	May, I. M. & Duan, Y. 1997. A local arc-length procedure for strain softening. <i>Computers &amp; Structures</i> , 64, 297-303.
125	May, S., Vignollet, J. & De Borst, R. 2015. A numerical assessment of phase-field models for brittle and cohesive fracture: $\Gamma$ -Convergence and stress oscillations. <i>European Journal of Mechanics-A/Solids</i> , 52, 72-84.
126	Mazars, J. 1986. A description of micro- and macroscale damage of concrete structures. <i>Engineering Fracture Mechanics</i> , 25, 729-737.
127	Mazars, J. & Lemaitre, J. 1985. Application of Continuous Damage Mechanics to Strain and Fracture Behavior of Concrete. In: SHAH, S. P. (ed.) <i>Application of Fracture Mechanics to Cementitious Composites</i> . Springer Netherlands.
128	Mazars, J. & Pijaudier-Cabot, G. 1989. Continuum damage theory-application to concrete. <i>Journal of Engineering Mechanics</i> , 115, 345-365.
129	Melenk, J. M. & Babuška, I. 1996. The partition of unity finite element method: Basic theory and applications. <i>Computer Methods in Applied Mechanics and Engineering</i> , 139, 289-314.
130	Meschke, G., Lackner, R. & Mang, H. A. 1998. An anisotropic elastoplastic-damage model for plain concrete. <i>International Journal for Numerical Methods in Engineering</i> , 42, 703-727.
131	Moës, N., Dolbow, J. & Belytschko, T. 1999. A finite element method for crack growth without remeshing. <i>International Journal for Numerical Methods in Engineering</i> , 46, 131-150.
132	Mosalam, K. M. & Paulino, G. H. 1997. Evolutionary characteristic length method for smeared cracking finite element models. <i>Finite Elements in Analysis and Design</i> , 27, 99-108.
133	Mosler, J. 2004. On the modeling of highly localized deformations induced by material failure: The strong discontinuity approach. <i>Archives of Computational Methods in Engineering</i> , 11, 389-446.

134	Mosler, J. 2005. A novel algorithmic framework for the numerical implementation of locally embedded strong discontinuities. <i>Computer Methods in Applied Mechanics and Engineering</i> , 194, 4731-4757.
135	Mosler, J. 2006. Modeling strong discontinuities at finite strains—A novel numerical implementation. <i>Computer Methods in Applied Mechanics and Engineering</i> , 195, 4396-4419.
136	Mosler, J. & Meschke, G. 2003. 3D modelling of strong discontinuities in elastoplastic solids: fixed and rotating localization formulations. <i>International Journal for Numerical Methods in Engineering</i> , 57, 1553-1576.
137	Mosler, J. & Meschke, G. 2004. Embedded crack vs. smeared crack models: a comparison of elementwise discontinuous crack path approaches with emphasis on mesh bias. <i>Computer Methods in Applied Mechanics and Engineering</i> , 193, 3351-3375.
138	Mosler, J., Stanković, L. & Radulović, R. 2011. Efficient modeling of localized material failure by means of a variationally consistent embedded strong discontinuity approach. <i>International Journal for Numerical Methods in Engineering</i> , 88, 1008-1041.
139	Murakami, S. 2012. <i>Continuum Damage Mechanics: A Continuum Mechanics Approach to the Analysis of Damage and Fracture</i> , Springer.
140	Murakami, S. & Ohno, N. 1981. A Continuum Theory of Creep and Creep Damage. In: PONTER, A. R. S. & HAYHURST, D. R. (eds.) <i>Creep in Structures</i> . Springer Berlin Heidelberg.
141	Nazir, S. & Dhanasekar, M. 2014. A non-linear interface element model for thin layer high adhesive mortared masonry. <i>Computers &amp; Structures</i> , 144, 23-39.
142	Needleman, A. 1988. Material rate dependence and mesh sensitivity in localization problems. <i>Computer Methods in Applied Mechanics and Engineering</i> , 67, 69-85.
143	Ngo, D. & Scordelis, A. C. 1967. Finite Element Analysis of Reinforced Concrete Beams. <i>Journal Proceedings</i> , 64.
144	Nguyen, G. D. 2005. <i>A thermodynamic approach to constitutive modelling of concrete using damage mechanics and plasticity theory</i> . PhD, Oxford University.
145	Nguyen, G. D. & Houlsby, G. T. 2008. A coupled damage–plasticity model for concrete based on thermodynamic principles: Part I: model formulation and parameter identification. <i>International Journal for Numerical and Analytical Methods in Geomechanics</i> , 32, 353-389.

146	Nguyen, V. P., Rabczuk, T., Bordas, S. & Duflot, M. 2008. Meshless methods: A review and computer implementation aspects. <i>Mathematics and Computers in Simulation</i> , 79, 763-813.
147	Oliver, J. 1989. A consistent characteristic length for smeared cracking models. <i>International Journal for Numerical Methods in Engineering</i> , 28, 461-474.
148	Oliver, J. 1996a. Modelling strong discontinuities in solid mechanics via strain softening constitutive equations. Part1: Numerical Simulation. <i>International Journal for Numerical Methods in Engineering</i> , 39, 3575-3600.
149	Oliver, J. 1996b. Modelling strong discontinuities in solid mechanics via strain softening constitutive equations. Part2: Numerical Simulation. <i>International Journal for Numerical Methods in Engineering</i> , 39, 3601-3623.
150	Oliver, J. 2000. On the discrete constitutive models induced by strong discontinuity kinematics and continuum constitutive equations. <i>International Journal of Solids and Structures</i> , 37, 7207-7229.
151	Oliver, J., Cervera, M. & Manzoli, O. 1999. Strong discontinuities and continuum plasticity models: the strong discontinuity approach. <i>International Journal of Plasticity</i> , 15, 319-351.
152	Oliver, J., Cervera, M., Oller, S. & Lubliner, J. 1990. Isotropic Damage Models and Smeared Crack Analysis of Concrete. <i>Computer Aided Analysis and design of Concrete Structures, Proceedings of SCI-C 1990, II. International Conference, Austria</i> , 945-957.
153	Oliver, J., Huespe, A., Pulido, M. & Samaniego, E. 2003a. On the strong discontinuity approach in finite deformation settings. <i>International Journal for Numerical Methods in Engineering</i> , 56, 1051-1082.
154	Oliver, J. & Huespe, A. E. 2004. Continuum approach to material failure in strong discontinuity settings. <i>Computer Methods in Applied Mechanics and Engineering</i> , 193, 3195-3220.
155	Oliver, J., Huespe, A. E., Blanco, S. & Linero, D. L. 2006a. Stability and robustness issues in numerical modeling of material failure with the strong discontinuity approach. <i>Computer Methods in Applied Mechanics and Engineering</i> , 195, 7093-7114.
156	Oliver, J., Huespe, A. E. & Cante, J. C. 2008a. An implicit/explicit integration scheme to increase computability of non-linear material and contact/friction problems. <i>Computer Methods in Applied Mechanics and Engineering</i> , 197, 1865-1889.
157	Oliver, J., Huespe, A. E. & Dias, I. F. 2012. Strain localization, strong discontinuities and material fracture: Matches and mismatches. <i>Computer Methods in Applied Mechanics and Engineering</i> , 241–244, 323-336.

158	Oliver, J., Huespe, A. E., Pulido, M. D. G. & Chaves, E. 2002. From continuum mechanics to fracture mechanics: the strong discontinuity approach. <i>Engineering Fracture Mechanics</i> , 69, 113-136.
159	Oliver, J., Huespe, A. E. & Samaniego, E. 2003b. A study on finite elements for capturing strong discontinuities. <i>International Journal for Numerical Methods in Engineering</i> , 56, 2135-2161.
160	Oliver, J., Huespe, A. E., Samaniego, E. & Chaves, E. W. V. 2004. Continuum approach to the numerical simulation of material failure in concrete. <i>International Journal for Numerical and Analytical Methods in Geomechanics</i> , 28, 609-632.
161	Oliver, J., Huespe, A. E. & Sánchez, P. J. 2006b. A comparative study on finite elements for capturing strong discontinuities: E-FEM vs X-FEM. <i>Computer Methods in Applied Mechanics and Engineering</i> , 195, 4732-4752.
162	Oliver, J., Linero, D. L., Huespe, A. E. & Manzoli, O. L. 2008b. Two-dimensional modeling of material failure in reinforced concrete by means of a continuum strong discontinuity approach. <i>Computer Methods in Applied Mechanics and Engineering</i> , 197, 332-348.
163	Omidi, O. & Lotfi, V. 2013. Continuum large cracking in a rate-dependent plastic–damage model for cyclic-loaded concrete structures. <i>International Journal for Numerical and Analytical Methods in Geomechanics</i> , 37, 1363-1390.
164	Ortiz, M. 1985. A constitutive theory for the inelastic behavior of concrete. <i>Mechanics of materials</i> , 4, 67-93.
165	Ortiz, M., Leroy, Y. & Needleman, A. 1987. A finite element method for localized failure analysis. <i>Computer Methods in Applied Mechanics and Engineering</i> , 61, 189-214.
166	Paggi, M. & Wriggers, P. 2016. Node-to-segment and node-to-surface interface finite elements for fracture mechanics. <i>Computer Methods in Applied Mechanics and Engineering</i> , 300, 540-560.
167	Parvaneh, S. M. & Foster, C. D. 2016. On numerical aspects of different updating schedules for tracking fracture path in strain localization modeling. <i>Engineering Fracture Mechanics</i> , 152, 26-57.
168	Peerlings, R., Brekelmans, W., De Borst, R. & Geers, M. Enhanced damage modelling of quasi-brittle and fatigue fracture : computational aspects. European congress on computational methods in applied sciences and engineering, 11-14 September 2000 Barcelona. 1-20.
169	Peerlings, R. H. J., deBorst, R., Brekelmans, W. A. M. & deVree, J. H. P. 1996. Gradient enhanced damage for quasi-brittle materials. <i>International Journal for Numerical Methods in Engineering</i> , 39, 3391-3403.

170	Peerlings, R. H. J., Geers, M. G. D., de Borst, R. & Brekelmans, W. A. M. 2001. A critical comparison of nonlocal and gradient-enhanced softening continua. <i>International Journal of Solids and Structures</i> , 38, 7723-7746.
171	Pijaudier-Cabot, G. & Bažant, Z. 1987. Nonlocal Damage Theory. <i>Journal of Engineering Mechanics</i> , 113, 1512-1533.
172	Pohl, T., Ramm, E. & Bischoff, M. 2014. Adaptive path following schemes for problems with softening. <i>Finite Elements in Analysis and Design</i> , 86, 12-22.
173	Prazeres, P. C., Bitencourt, L. G., Jr., Bittencourt, T. & Manzoli, O. 2015. A modified implicit–explicit integration scheme: an application to elastoplasticity problems. <i>Journal of the Brazilian Society of Mechanical Sciences and Engineering</i> , 1-11.
174	Radulovic, R., Bruhns, O. T. & Mosler, J. 2011. Effective 3D failure simulations by combining the advantages of embedded Strong Discontinuity Approaches and classical interface elements. <i>Engineering Fracture Mechanics</i> , 78, 2470-2485.
175	Rashid, Y. R. 1968. Ultimate strength analysis of prestressed concrete pressure vessels. <i>Nuclear Engineering and Design</i> , 7, 334-344.
176	Regueiro, R. A. & Borja, R. I. 1999. A finite element model of localized deformation in frictional materials taking a strong discontinuity approach. <i>Finite Elements in Analysis and Design</i> , 33, 283-315.
177	Reinhardt, H. W. 1984. <i>Fracture mechanics of an elastic softening material like concrete</i> , Delft, Netherlands, Stevin-Laboratory of the Dept. of Civil Engineering, Delft University of Technology.
178	Richard, B., Ragueneau, F., Cremona, C. & Adelaide, L. 2010. Isotropic continuum damage mechanics for concrete under cyclic loading: Stiffness recovery, inelastic strains and frictional sliding. <i>Engineering Fracture Mechanics</i> , 77, 1203-1223.
179	Riks, E. 1979. An incremental approach to the solution of snapping and buckling problems. <i>International Journal of Solids and Structures</i> , 15, 529-551.
180	Ritto-Corrêa, M. & Camotim, D. 2008. On the arc-length and other quadratic control methods: Established, less known and new implementation procedures. <i>Computers &amp; Structures</i> , 86, 1353-1368.
181	Rodríguez-Ferran, A., Bennett, T., Askes, H. & Tamayo-Mas, E. 2011. A general framework for softening regularisation based on gradient elasticity. <i>International Journal of Solids and Structures</i> , 48, 1382-1394.
182	Rots, J. 1991. Smearred and discrete representations of localized fracture. <i>International Journal of Fracture</i> , 51, 45-59.

183	Rots, J. 2001. Sequentially linear continuum model for concrete fracture. <i>In: Fracture mechanics of concrete structures, De Borst R, Mazars J, Pijaudier-Cabot G, van Mier JGM, Balkema AA, editors.</i> , The Netherlands: Liss, 831–839.
184	Rots, J. G. 1988. <i>Computational modeling of concrete fracture</i> . PhD, Delft University.
185	Rots, J. G., Belletti, B. & Invernizzi, S. 2008. Robust modeling of RC structures with an “event-by-event” strategy. <i>Engineering Fracture Mechanics</i> , 75, 590-614.
186	Rots, J. G. & Blaauwendraad, J. 1989. Crack models for concrete, discrete or smeared? Fixed, multi-directional or rotating?. <i>HERON</i> , 34 (1).
187	Rots, J. G. & Invernizzi, S. 2004. Regularized sequentially linear saw-tooth softening model. <i>International Journal for Numerical and Analytical Methods in Geomechanics</i> , 28, 821-856.
188	Ru, C. Q. & Aifantis, E. C. 1993. A simple approach to solve boundary-value problems in gradient elasticity. <i>Acta Mechanica</i> , 101, 59-68.
189	Sankar, B. V., Waas, A. M. & Hyer, M. W. 2013. <i>Damage in Composites</i> , Destech Publications Incorporated.
190	Schellekens, J. C. J. & De Borst, R. 1993a. A non-linear finite element approach for the analysis of mode-I free edge delamination in composites. <i>International Journal of Solids and Structures</i> , 30, 1239-1253.
191	Schellekens, J. C. J. & De Borst, R. 1993b. On the numerical integration of interface elements. <i>International Journal for Numerical Methods in Engineering</i> , 36, 43-66.
192	Shah, S. P., Swartz, S. E. & Ouyang, C. 1995. <i>Fracture Mechanics of Concrete: Applications of Fracture Mechanics to Concrete, Rock and Other Quasi-Brittle Materials</i> , Wiley.
193	Simo, J. & Oliver, J. 1994. A new approach to the analysis and simulation of strain softening in solids. <i>Fracture and damage in quasibrittle structures</i> , 25-39.
194	Simo, J. C. & Armero, F. 1992. Geometrically non-linear enhanced strain mixed methods and the method of incompatible modes. <i>International Journal for Numerical Methods in Engineering</i> , 33, 1413-1449.
195	Simo, J. C., Oliver, J. & Armero, F. 1993. An analysis of strong discontinuities induced by strain-softening in rate-independent inelastic solids. <i>Computational Mechanics</i> , 12, 277-296.

196	Simo, J. C. & Rifai, M. S. 1990. A class of mixed assumed strain methods and the method of incompatible modes. <i>International Journal for Numerical Methods in Engineering</i> , 29, 1595-1638.
197	Slobbe, A. T. 2015. <i>Propagation and band width of smeared cracks</i> . PhD, Delft University of Technology.
198	Slobbe, A. T., Hendriks, M. A. N. & Rots, J. G. 2012. Sequentially linear analysis of shear critical reinforced concrete beams without shear reinforcement. <i>Finite Elements in Analysis and Design</i> , 50, 108-124.
199	Slobbe, A. T., Hendriks, M. A. N. & Rots, J. G. 2013. Systematic assessment of directional mesh bias with periodic boundary conditions: Applied to the crack band model. <i>Engineering Fracture Mechanics</i> , 109, 186-208.
200	Slobbe, A. T., Hendriks, M. A. N. & Rots, J. G. 2014. Smoothing the propagation of smeared cracks. <i>Engineering Fracture Mechanics</i> , 132, 147-168.
201	Sukumar, N., Moës, N., Moran, B. & Belytschko, T. 2000. Extended finite element method for three-dimensional crack modelling. <i>International Journal for Numerical Methods in Engineering</i> , 48, 1549-1570.
202	Swenson, D. V. & Ingraffea, A. R. 1988. Modeling mixed-mode dynamic crack propagation using finite elements: Theory and applications. <i>Computational Mechanics</i> , 3, 381-397.
203	Tao, X. & Phillips, D. V. 2005. A simplified isotropic damage model for concrete under bi-axial stress states. <i>Cement and Concrete Composites</i> , 27, 716-726.
204	Torrenti, J. M., Pijaudier-Cabot, G. & Reynouard, J. M. 2013. <i>Mechanical Behavior of Concrete</i> , Wiley.
205	Truster, T. J. 2016. On interface element insertion into three-dimensional meshes. <i>Engineering Fracture Mechanics</i> , 153, 171-174.
206	van Mier, J. G. M. 1996. <i>Fracture Processes of Concrete</i> , Taylor & Francis.
207	van Mier, J. G. M. 2012. <i>Concrete Fracture: A Multiscale Approach</i> , Taylor & Francis.
208	Vandoren, B., De Proft, K., Simone, A. & Sluys, L. J. 2013. A novel constrained LARge Time INcrement method for modelling quasi-brittle failure. <i>Computer Methods in Applied Mechanics and Engineering</i> , 265, 148-162.
209	Verhoosel, C. V., Remmers, J. J. C. & Gutiérrez, M. A. 2009. A dissipation-based arc-length method for robust simulation of brittle and ductile failure. <i>International Journal for Numerical Methods in Engineering</i> , 77, 1290-1321.

210	Vignollet, J., May, S. & de Borst, R. 2015. On the numerical integration of isogeometric interface elements. <i>International Journal for Numerical Methods in Engineering</i> , 102, 1733-1749.
211	Volokh, K. Y. 2013. Characteristic length of damage localization in concrete. <i>Mechanics Research Communications</i> , 51, 29-31.
212	Vorel, J. & Boshoff, W. P. 2015. Computational modelling of real structures made of Strain-hardening Cement-based Composites. <i>Applied Mathematics and Computation</i> , 267, 562-570.
213	Voyiadjis, G. Z. & Kattan, P. I. 2006. <i>Advances in Damage Mechanics</i> , Elsevier Science.
214	Voyiadjis, G. Z., Taqieddin, Z. N. & Kattan, P. I. 2008. Anisotropic damage–plasticity model for concrete. <i>International Journal of Plasticity</i> , 24, 1946-1965.
215	Wawrzynek, P. A. & Ingraffea, A. R. 1987. Interactive finite element analysis of fracture processes: An integrated approach. <i>Theoretical and Applied Fracture Mechanics</i> , 8, 137-150.
216	Wells, G. N. & Sluys, L. J. 2001a. A new method for modelling cohesive cracks using finite elements. <i>International Journal for Numerical Methods in Engineering</i> , 50, 2667-2682.
217	Wells, G. N. & Sluys, L. J. 2001b. Three-dimensional embedded discontinuity model for brittle fracture. <i>International Journal of Solids and Structures</i> , 38, 897-913.
218	Wells, G. N., Sluys, L. J. & de Borst, R. 2002. Simulating the propagation of displacement discontinuities in a regularized strain-softening medium. <i>International Journal for Numerical Methods in Engineering</i> , 53, 1235-1256.
219	Wempner, G. A. 1971. Discrete approximations related to nonlinear theories of solids. <i>International Journal of Solids and Structures</i> , 7, 1581-1599.
220	Willam, K. J. & Warnke, E. P. 1975. <i>Constitutive models for triaxial behavior of concrete</i> , Proc. Int. Assoc. Bridge Struct. Engrg, Report 19, Zurich,Switzerland, pp:1-30.
221	Wriggers, P. 2008. <i>Nonlinear finite element methods</i> , Springer Science & Business Media.
222	Xu, W. & Waas, A. M. 2015. Modeling damage growth using the crack band model; effect of different strain measures. <i>Engineering Fracture Mechanics</i> .
223	Zienkiewicz, O. C. & Taylor, R. L. 2000. <i>The Finite Element Method: Solid mechanics</i> , Butterworth-Heinemann.

224	Zubelewicz, A. & Bažant, Z. 1987. Interface Element Modeling of Fracture in Aggregate Composites. <i>Journal of Engineering Mechanics</i> , 113, 1619-1630.
-----	---